Title
Towards Absolutely Quantitative Phase Contrast Magnetic Resonance Imaging

Author
Middione, Matthew J.

Publication Date
2013

UNIVERSITY OF CALIFORNIA

Los Angeles

Towards Absolutely Quantitative Phase Contrast Magnetic Resonance Imaging

A dissertation submitted in partial satisfaction of the
requirements for the degree Doctor of Philosophy
in Biomedical Physics

by

Matthew Joseph Middione

2013

ABSTRACT OF THE DISSERTATION

Towards Absolutely Quantitative Phase Contrast
Magnetic Resonance Imaging

by

Matthew Joseph Middione

Doctor of Philosophy in Biomedical Physics

University of California, Los Angeles, 2013

Professor Daniel B. Ennis, Chair

Phase Contrast Magnetic Resonance Imaging (PC-MRI) is a non-invasive clinical imaging technique used primarily for measuring blood velocity and flow throughout the major blood vessels of the cardiovascular system. PC-MRI uses magnetic field gradients to impart zero phase to stationary spins and a non-zero phase to moving spins. The phase measurements provide quantitative information that is useful during the diagnosis and treatment of many cardiovascular diseases. Blood flow measurements obtained using PC-MRI hold an advantage over other techniques, namely echocardiography and catheterization, due to its ability to reduce lifetime radiation exposure, provide accurate and direct quantification of flow, and it’s non-invasiveness. Despite decades of research, our ability to measure blood flow with PC-MRI is still hampered by quantitative inaccuracies leading to clinically significant errors, which dampens clinical enthusiasm for the technique. Nevertheless PC-MRI continues to be a compelling clinical technique

because of the need to non-invasively measure flow in a wide range of clinical contexts. Frequently inconsistent PC-MRI measurements, however, continue to be a source of clinical frustration and in order for PC-MRI to become an absolutely quantitative measure of flow, both the accuracy and precision of these measurements must be improved. Herein an analysis of the effects of chemically shifted perivascular fat; time efficient velocity encoding; region-of-interest contouring; and the use of convex gradient optimization is conducted in an effort towards developing absolutely quantitative PC-MRI.

In Chapter 4 we explore the phase errors associated with chemically shifted perivascular fat. Stationary perivascular fat, which surrounds most vessels throughout the cardiovascular system, can impart a significant chemical shift-induced phase error in PC-MRI. This chemical shift error does not subtract in phase difference processing, unlike other off-resonance phase errors, but can be minimized significantly with proper parameter selection. The chemical shift induced phase errors largely depend on both the receiver bandwidth and the echo time (TE). The amount of chemically shifted fat pixels that shift into the vessel can be reduced by increasing the receiver bandwidth while the use of an in-phase TE (TE_{IN}) will ensure that fat and water resonances are in-phase with slow flowing blood near the vessel wall, which minimizes the resulting errors in the calculated velocity. Computational simulations and both in vitro and in vivo experiments are used to show that the use of a high bandwidth and TE_{IN} significantly improves intra-subject flow agreement compared to a more clinically standard low receiver bandwidth and the minimum available TE (TE_{MIN}).

In Chapter 5 we explore a time efficient chemical shift reduction strategy. The minimum available TE_{IN} at 3T field strength ($TE_{IN,MIN}$ = 2.46 ms), however, may not be routinely achievable with standard flow-encoding methods. Hence, we developed a novel method for flow encoding in PC-MRI, which uses the slice select gradient and a time-shifted refocusing gradient lobe for velocity encoding. Velocity encoding with the slice select refocusing gradient (SSRG) enables the use of $TE_{IN,MIN}$ at 3T for time-efficient reduction of chemical shift-induced phase errors in PC-MRI, whereas this can't be achieved with bi-polar or flow compensated/flow encoded PC-MRI. In vivo measurements were acquired to show that PC-MRI measurements obtained using SSRG with a high receiver bandwidth and $TE_{IN,MIN}$ significantly improves intra-subject flow agreement compared to a conventional clinical sequence, which uses a low receiver bandwidth and TE_{MIN}. This approach also increases temporal resolution and signal-to-noise ratio by 35% and 33%, respectively.

In Chapter 6 we explore time efficient velocity encoding and the capabilities of convex gradient optimization in PC-MRI in chapter 7. Conventional PC-MRI pulse sequences use time inefficient velocity encoding methods along with trapezoidal and triangular gradient lobes, which do not make optimal use of the available gradient hardware. Convex gradient optimization (CVX) can be used to minimize PC-MRI gradient waveform durations subject to both gradient hardware and pulse sequence constraints. CVX PC-MRI with $TE_{IN,MIN}$ provides more accurate measurements of blood flow and velocity through the reduction of chemical shift-induced phase errors and increased sequence efficiency, which can provide either higher spatial or higher temporal resolution.

Another potential source of error in PC-MRI flow quantification occurs during image analysis. In Chapter 8 we analyze the errors associated with ROI contouring in PC-MRI. PC-MRI blood flow measurements require a region-of-interest (ROI) to be manually contoured to encompass the vessel lumen, but this process is subjective and prone to error. A systematic analysis of ROI contouring was used to evaluate the impact of overestimating and underestimating the ROI size on PC-MRI flow measurements. ROIs that overestimate the vessel lumen/wall boundary contribute a lower magnitude total flow error compared to ROIs that underestimate the same boundary.

Reducing errors arising from chemically shifted perivascular fat, implementing time efficient velocity encoding, increasing spatiotemporal resolution through the use of convex gradient optimization, and careful analysis of ROI contours all help move us towards absolutely quantitative PC-MRI.

The dissertation of Matthew Joseph Middione is approved.

Debiao Li

Holden H. Wu

Noriko Salamon

Peng Hu

J. Paul Finn

Daniel B. Ennis, Committee Chair

University of California, Los Angeles

2013

DEDICATION

This dissertation is dedicated to my loving and supportive wife, Kristin, as well as my spirited and encouraging family, Joseph, Kim, Marissa, and Michelle.

TABLE OF CONTENTS

Abstract ii

Acknowledgements x

Biographical Sketch xi

Publications and Accepted Conference Abstracts xi

Dissertation Motivation 1

Chapter 1: Magnetic Resonance Imaging 6

- Introduction 6
- Nuclear Magnetic Resonance 7
- Radio Frequency Excitation 11
- Magnetic Field Gradients 16
- Spatial Encoding 18
- Image Reconstruction 24
- Gradient Recalled Echo Imaging 25

Chapter 2: Cardiovascular Magnetic Resonance Imaging 30

- Cardiac Triggering and Segmentation 30

Chapter 3: Phase Contrast Magnetic Resonance Imaging 35

- Velocity Encoding 35
- Gradient Moments 38
- Velocity Encoding Strategies 41
- Cardiac Image Localization and Acquisition 43
- Quantitative Measures of Blood Velocity and Flow 46
- Background Phase Errors 46

Clinical Significance of Phase Contrast Measurements....48

Chapter 4: Chemical Shift-Induced Phase Errors....52

Chapter 5: Velocity Encoding with the Slice Select Refocusing Gradient....82

Chapter 6: Asymmetric Velocity Encoding....117

Chapter 7: Convex Gradient Design....123

Chapter 8: Region-of-Interest Contouring Errors....156

Chapter 9: Conclusions....170

Appendix A....173

Appendix B....175

References....180

ACKNOWLEDGEMENTS

I wish to thank my committee members who were more than generous with their donation of expertise, time, and constructive criticism. A special thanks to Dr. Daniel B. Ennis, my committee chair and thesis advisor, for his countless hours of guidance, reading, encouragement, and friendship.

To my fellow graduate students in the Department of Biomedical Physics, thank you for the hours spent studying, playing racquetball and poker, and for your friendship. A special thanks for all the advisement and support from the administrative members of the department, including Terry Moore, Reth Thatch Im, and program director Dr. Michael McNitt-Gray.

I am thankful to my fellow students in Dr. Daniel B. Ennis' lab and also the members of Dr. Peng Hu's lab for volunteering as healthy subjects for my studies; providing feedback on conference abstracts, submitted journal articles, and presentations; and their friendship.

Lastly, I would like to thank the members of the UCLA Department of Radiology and Siemens Medical Solutions for their support and scientific collaboration.

BIOGRAPHICAL SKETCH

2008 BS Biomedical Physics, California State University, Fresno, CA

2010 MS Biomedical Physics, University of California, Los Angeles, CA

PUBLICATIONS

1. Zou Y, **Middione MJ***, Srinivasan S, Ennis DB. *Analysis of Gradient Spoiling in Phase Contrast MRI*. Magn Reson Med 2013 {In Preparation}.
2. **Middione MJ**, Wu HH, Ennis DB. *Convex Gradient Optimization for Increased Spatiotemporal Resolution and Improved Accuracy in Phase Contrast MRI*. Magn Reson Med 2013{Submitted}.
3. **Middione MJ**, Thompson RB, Ennis DB. *Velocity Encoding with the Slice Select Refocusing Gradient for Faster Imaging and Reduced Chemical Shift-Induced Phase Errors*. Magn Reson Med 2013. doi: 10.1002/mrm.24861.
4. **Middione MJ**, Ennis DB. *The Effects of Chemically Shifted Perivascular Fat in Quantitative Phase Contrast MRI*. Magn Reson Med 2013; 69:391-401.

ACCEPTED CONFERENCE ABSTRACTS

1. Zou Y, **Middione MJ***, Srinivasan S, Ennis DB. *Analysis of Gradient Spoiling in Phase Contrast MRI*. ISMRM Flow and Motion Study Group Salt Lake City, Utah, 2013.
2. **Middione MJ**, Ennis DB. *Reduced Chemical Shift-Induced Phase Errors at 3T Using Novel PC-MRI Encoding Gradients*. SCMR/ISMRM Joint Scientific Sessions San Francisco, California, 2013.

3. **Middione MJ**, Ennis DB. *Chemical Shift-Induced Phase Errors in Phase Contrast MRI*. ISMRM Conf Proc Melbourne, Australia 2012 {Young Investigator Award Winner, Magna Cum Laude Award Winner}.
4. **Middione MJ**, Ennis DB. *Reduction of Eddy Current-Induced Velocity Offsets in Phase Contrast MRI*. ISMRM Conf Proc, Melbourne, Australia 2012.
5. **Middione MJ**, Ennis DB. *Flip Angle Optimization for Quantitative Phase Contrast MR Imaging*. SCMR Conf. Proc. Nice, France. 2011.
6. **Middione MJ**, Moghadam AN, Natsuaki Y, Ennis DB. *The Effects of Chemically Shifted Perivascular Fat in Quantitative Phase Contrast MRI*. ISMRM Conf Proc Montreal, Quebec, Canada 2011.

* Co-first author

DISSERTATION MOTIVATION

Congenital heart disease (CHD) affects 9.6 per 1000 live births (1) and an increasing population of adolescents and adults are living with CHD (35-year survival is approximately 85% (2)). Patients with CHD often require a lifetime of clinical evaluation, multiple surgeries, numerous interventional procedures, and dozens of imaging exams – all of which contribute to the high costs associated with managing the disease ($1.4 billion in annual hospital costs) (3).

For pediatric and adult patients with CHD, diagnosis and treatment of the disease is aided by the ability to measure cardiovascular hemodynamics. Magnetic resonance imaging (MRI) exams play a central role in the management of patients with CHD and are routinely ordered for these patients for pre-surgical or pre-interventional evaluation because of the exceptional ability to visualize complex vascular anatomy and accurately measure ventricular volumes and masses. Furthermore, phase contrast MRI (PC-MRI) is a powerful non-invasive imaging technique used in patients with CHD to measure blood velocity and flow with flexible spatial and temporal resolution (4,5) and image orientation. PC-MRI is used clinically for evaluating cardiovascular flow regurgitant volume/fraction, right-left lung flow, Q_p/Q_s, stenotic pressure gradient, and more. However, poor intra-subject agreement and low confidence in PC-MRI can lead to: 1) follow-up exams, which incur greater downstream costs; or 2) a team of physicians left to make a “judgment call.”

Cardiac catheterization is the ‘gold standard’ for evaluating cardiovascular hemodynamics, but ionizing radiation, invasiveness, and expense mean that “it is not a practical method for longitudinal follow-ups,” (6) which are needed, for example, to identify the optimal timing for an intervention. Ionizing radiation concerns also limit the repeated use of computed tomography (CT) and nuclear scintigraphy.

Body habitus combined with vessel angulation and the interposition of surgical scarring and the lungs sometimes limits the effectiveness of echocardiography (7-9). This is especially true for the evaluation of the right heart, where echocardiography is challenged to measure branch pulmonary artery flow, pulmonary regurgitant fraction/volume, and/or flow in the main pulmonary artery.

Despite clinical preference and guidelines (2,7,10-13) suggesting the use of PC-MRI for blood velocity and flow measurements in CHD, its accuracy and reliability are frequently questioned due to poor internal consistency or inconsistent results compared to other clinical findings. As a consequence, many CHD patients undergo a diagnostic catheterization procedure or a follow-up echocardiographic exam to bolster clinical confidence prior to making treatment decisions. The ***principal objective*** of this dissertation is to improve the diagnostic accuracy of PC-MRI by pushing technical developments towards absolutely quantitative measurements in order to better guide treatment decisions. The ***overall objectives*** of this dissertation are to: 1) Minimize chemical shift-induced PC-MRI errors arising from chemically shifted perivascular fat (Chapter 4); 2) Develop a novel velocity encoding method for time efficient chemical shift reduction (Chapter 5); 3) Develop time efficient velocity encoding (Chapter 6); 4) Implement convex gradient optimization in PC-MRI (Chapter 7); and 5) Analyze the errors associated with contouring regions-of-interest in PC-MRI measurements (Chapter 8).

The objectives are more cogently described by the following ***Specific Aims***:

SPECIFIC AIM #1 – *Reduce chemical shift effects in PC-MRI.* Perivascular fat that surrounds most vessels can chemically shift across the vessel wall into the lumen. The complex fat signal then adds to the complex water signal and leads to a clinically significant measurement error that does not subtract in phase difference imaging. In Chapter 4 we define the effects of chemically shifted perivascular fat in PC-MRI and develop a coherent error reduction strategy. We ***hypothesize*** that chemical shift-induced phase errors can be effectively eliminated by careful selection of the receiver bandwidth and echo time (TE), leading to more accurate PC-MRI measures of blood flow.

SPECIFIC AIM #2 – *Time efficient reduction of chemical shift effects in PC-MRI.* The chemical shift reduction strategy described in Specific Aim #1 necessitates the use of a prohibitively long TE. In Chapter 5 we describe and evaluate a method for flow encoding in PC-MRI that uses the slice select gradient and a time-shifted refocusing gradient lobe for velocity encoding. We ***hypothesize*** that chemical shift-induced phase errors can be efficiently eliminated using slice select refocused gradient encoding, which shortens the TE and the repetition time (TR) and can be used to improve spatiotemporal resolution or decrease breath hold time.

SPECIFIC AIM #3 – *Time efficient velocity encoding.* Traditional PC-MRI methods employ either a pair of equal-and-opposite velocity encoding gradients (Bipolar) (14,15) or a flow compensated and flow encoded gradient pair (FCFE) (16,17). In Chapter 6 we describe that each strategy has its benefits and drawbacks; but neither sequence is the most time efficiency over a wide range of clinically useful velocity encoding strengths. We ***hypothesize*** that reductions in TE/TR can be achieved by designing the fastest triangular and trapezoidal shaped velocity encoding gradient waveforms, providing significant increases in spatiotemporal resolution over conventional PC-MRI methods and more accurate measures of blood velocity and flow.

SPECIFIC AIM #4 – *Convex gradient optimization.* Conventional gradient waveform design in PC-MRI involves the use of triangular or trapezoidal waveforms, which do not optimally use the available gradient hardware. Instead, these waveforms typically limit the sequence design to $G_{Max}/\sqrt{3}$ and $SR_{Max}/\sqrt{3}$ (where G_{Max} is the maximum gradient amplitude and SR_{Max} is the maximum gradient slew rate) to ensure the sequence performs within the hardware limitations for any given double oblique slice orientation. Furthermore, these limits are only approached during a few instances throughout the sequence, which limits sequence efficiency. In Chapter 7, we ***hypothesize*** that the use of convex gradient optimization for all gradients within the PC-MRI pulse sequence will lead to more accurate measurements of blood flow and velocity through the reduction of chemical shift-induced phase errors and increased sequence efficiency, which can provide either higher spatial or higher temporal resolution.

SPECIFIC AIM #5 – *Regions-of-interest error analysis.* PC-MRI measurements require a region-of-interest (ROI) to be manually contoured to encompass the vessel lumen, but this process is subjective and prone to error. In Chapter 8, the objective of this Specific Aim is to systematically evaluate the impact of overestimating and underestimating the ROI size on PC-MRI flow measurements. We ***hypothesize*** that overestimating the ROI size will lead to higher accuracy compared to underestimating the ROI size and that these findings can be used to provide evidence based suggestions for ROI contouring to increase measurement accuracy in PC-MRI.

Overall, the work outlined in these Specific Aims will provide more accurate and precise PC-MRI measurements of blood velocity and flow compared to conventional PC-MRI methods. Additionally, these methods will have better diagnostic accuracy than conventional PC-MRI leading to increased clinical confidence in the reported measures. The overall impact of this work will be to improve the diagnostic accuracy of PC-MRI. Faster, more accurate, and more precise PC-MRI measurements with increased clinical confidence will provide more reliable flow measures for clinical management of patients with CHD. These methods will help streamline clinical care and decrease over-diagnosis, over-treatment, and overutilization of follow-up clinical exams for pediatric and adult patients with CHD.

CHAPTER 1

INTRODUCTION TO MAGNETIC RESONANCE IMAGING

In order to appreciate and understand the problems that currently limit phase contrast magnetic resonance imaging (PC-MRI) from being an absolutely quantitative measurement technique, an overall understanding of basic magnetic resonance imaging (MRI) principles is first needed. This chapter gives a brief introduction to the principles of MRI from spinning atomic protons to signal generation, signal detection, and image formation.

INTRODUCTION

MRI can be described as a medical imaging technique that produces detailed images of internal structures of the body. More specifically, MRI uses a strong magnetic field and the properties of nuclear magnetic resonance to produce images of molecules, namely hydrogen protons. MRI possesses several unique advantages over other medical imaging modalities. Unlike X-ray, Computed Tomography (CT), Single Photon Emission Computed Tomography (SPECT), and Positron Emission Tomography (PET), MRI operates in the radio-frequency energy range and thus uses no ionizing radiation. MRI has the ability to generate three-dimensional (3D) volumetric images at any oblique orientation. MRI also provides excellent soft tissue contrast, which makes it especially useful in imaging the brain, muscles, the heart, and cancerous tumors compared with other medical imaging techniques.

The process of generating an MR image can be divided into three steps: signal generation, detection, and reconstruction. At the nuclear level, the magnetic moment of hydrogen protons serve as the source of the MR signal. These magnetic moments are manipulated in the presence of a magnetic field and their collective behavior forms the basis of the measured signal. This signal is then recorded and later reconstructed to form an image. The remainder of this chapter describes the mechanics of how magnetic moments are manipulated to produce a signal, which is then reconstructed to form an MR image.

NUCLEAR MAGNETIC RESONANCE

Hydrogen atoms contain a single electron (negatively charged particle), which orbits a rotating nuclei containing a single proton (positively charged particle), which has non-negligible mass. Atomic nuclei have an intrinsic quantum property known as spin, which is classically associated with how atoms rotate about their axis. This spin combined with the proton's mass produces angular momentum, which can be expressed as a vector quantity having both magnitude and direction. The spin and charge of hydrogen nuclei, combined with its intrinsic angular momentum, produces a precessing magnetic field. This magnetic field is represented by a nuclear magnetic dipole moment, $\boldsymbol{\mu}$ (in units of kg×m^2×s^{-2}×T^{-1}, where T is Tesla), which is also a vector quantity having both magnitude and direction that is related to the angular momentum, $\boldsymbol{L}$ (in units of kg×m^2×Hz), by the following equation (Figure 1):

$$\boldsymbol{\mu} = \gamma \boldsymbol{L}, \tag{1}$$

where γ is the gyromagnetic ratio (in units of MHz/T, where MHz is Megahertz). For hydrogen the measured value is:

$$\gamma = 42.576 \ \frac{MHz}{T}. \tag{2}$$

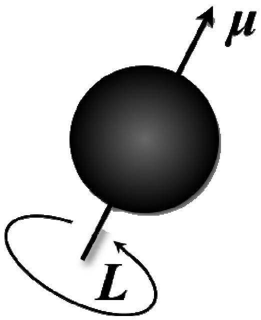

Figure 1. A hydrogen proton, which carries a mass, positive charge, and intrinsic nuclear spin with angular momentum, ***L***, produces a magnetic dipole moment, ***μ***.

The MRI signal generated by hydrogen nuclei, which are naturally abundant within the human body, is comprised of a collection of hydrogen protons, or spins. The sum of all the magnetic moments produced by each spin is called the net magnetization, ***M***. Normally, the direction of these spins are randomly distributed. Thus, the sum of all the spins yields a null net magnetization (***M*** = 0, Figure 2A). In the presence of a large external magnetic field, B_0, nuclear spins align along the axis of the main magnetic field (defined as the z-axis). Some of the spins align with the field (parallel) and some align against the field (anti-parallel) as seen in Figure 2B.

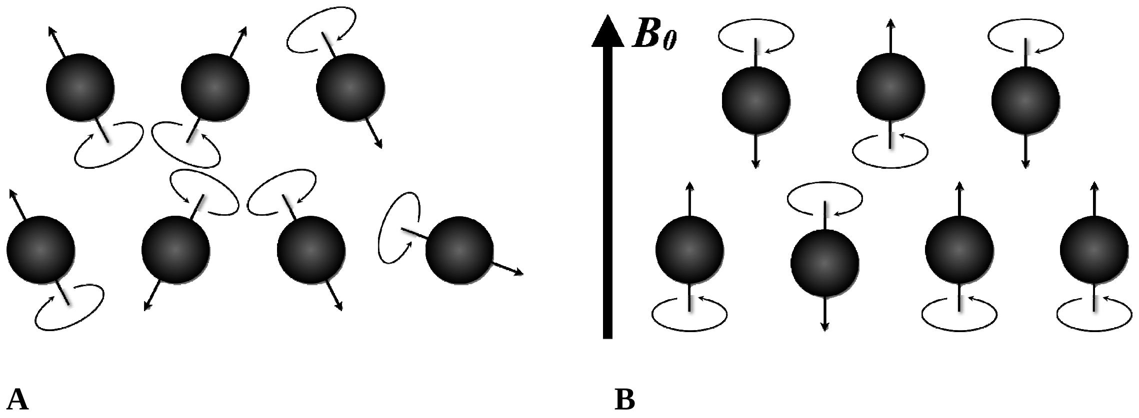

Figure 2. Randomly distributed spins produce no net magnetization (A) while in the presence of an applied field, B_0, spins align either parallel or anti-parallel producing a net magnetization (B).

Parallel spins are said to be in a low energy state, while anti-parallel spins are said to be in a high-energy state. The number of spins in the low energy state exceeds the number in the high-energy state. This leads to a net magnetization ($\boldsymbol{M} \neq 0$). This magnetization is a vector quantity that can be represented by a "longitudinal" component along the z-axis ($\boldsymbol{M_z}$ in Figure 3) and by a second component perpendicular to the first called the "transverse magnetization" along the xy-plane ($\boldsymbol{M_{xy}}$ in Figure 3).

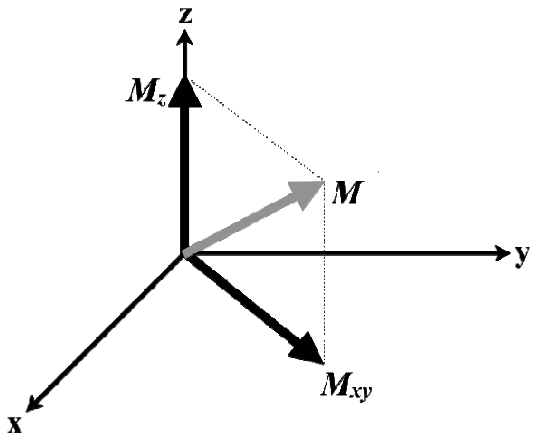

Figure 3. In the presence of an applied field, B_0, the magnetization, $\boldsymbol{M}$, has two components: longitudinal magnetization, M_z, which lies along the z-axis and transverse magnetization, $\boldsymbol{M}_{xy}$, which lies within the xy-plane. $\boldsymbol{M}_{xy}$ is a complex value possessing both a magnitude and a phase component.

In addition to the development of different energy states and the resulting net magnetization, the presence of an external magnetic field induces a torque on each spin as a consequence of the balance of forces described by the equation of motion for a spin ensemble, which illustrates how each spin precesses about the z-axis. This precession is analogous to a spinning top. The angular frequency of the precession, known as the Larmor frequency, ω_0, is proportional to the strength of the main magnetic field (Figure 4).

$$\boldsymbol{\omega}_0 = \gamma \boldsymbol{B}_0. \qquad [3]$$

These precessing spins form the net magnetization and serve as the basis of MR signal.

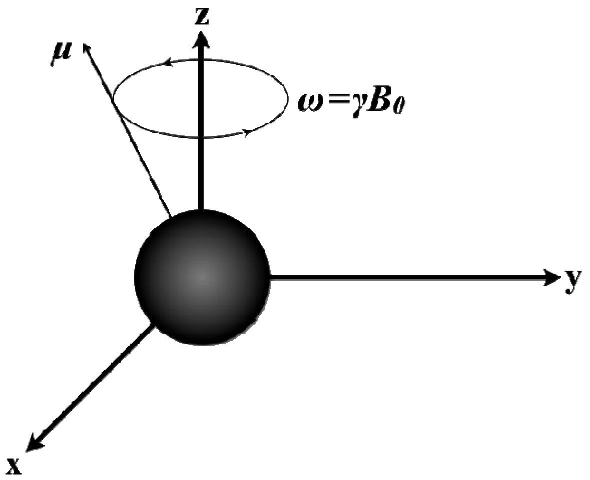

Figure 4. Pictorial description of a spin precessing at the Larmor frequency (ω) about the axis of an external magnetic field (B_0).

RADIO FREQUENCY EXCITATION

Although each spin precesses at the same frequency, they do not necessarily precess in-phase. As a result, the sum of the microscopic transverse magnetizations of each spin yields a no net transverse macroscopic magnetization (Figure 5). By design of the detector, only transverse magnetization produces a detectable signal in MRI. Thus, in order for the spins to produce a transverse signal, they must reach phase coherence, requiring the application of an external force. For a magnetized spin system, this external force comes from an oscillating magnetic field denoted as $B_1(t)$, which is distinctly different from the static main magnetic field, B_0. Clinical scanners use B_0 ranging from 1.5-3T while typical values for B_1 are about 5×10^{-6} T. For reference, the strength of the Earth's magnetic field is about 5×10^{-5} T. Classical physics mandates that $B_1(t)$ rotates in the same manner as the precessing spins it acts upon. This requirement, known as the resonance condition, dictates that the rotation of the applied B_1(t) field must match the Larmor frequency of the precessing spins.

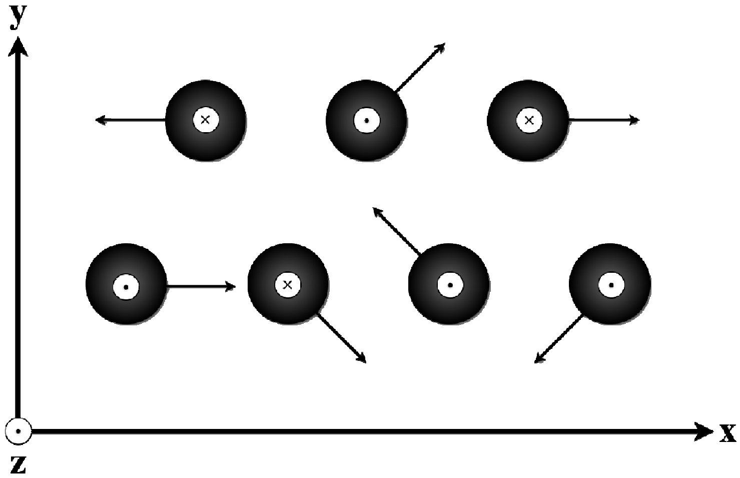

Figure 5. Although the spins have a net longitudinal magnetization component (M_z; into the page) phase incoherence results in a net zero transverse magnetization component, $\boldsymbol{M_{xy}}$, which leads to no measurable signal.

The required oscillating B_1(t) field is achieved through the application of a radio frequency (RF) pulse. RF pulses act to force the net magnetization of the precessing spins away from the direction of the static main magnetic field (z-axis) and towards the transverse xy-plane. This results in a measureable transverse signal component, $\boldsymbol{M_{xy}}$. The time-dependent behavior of the magnetization, $\boldsymbol{M}$, in the presence of the B_0 and B_1 magnetic fields is described quantitatively by the Bloch equation, which takes the form:

$$\frac{d\boldsymbol{M}}{dt} = \gamma \boldsymbol{M} \times \boldsymbol{B} - \frac{M_x \boldsymbol{i} + M_y \boldsymbol{j}}{T_2} - \frac{\left(M_z - M_z^0\right)\boldsymbol{k}}{T_1}, \qquad [4]$$

where M_z^0 is the equilibrium value of $\boldsymbol{M}$ in the presence of B_0 only, and T_1 and T_2 are time constants, which characterize the relaxation process of the bulk magnetization after it has been rotated away from its equilibrium state, which are not described in this dissertation. For the purposes of characterizing the time-dependent behavior of $\boldsymbol{M}$ during the application of the RF excitation pulse, which is relatively short compared to normal T_1 and T_2 values, the last two terms in Eq. 4 can be omitted. With this assumption, the Bloch equation takes a much simpler form:

$$\frac{d\boldsymbol{M}}{dt} = \gamma \boldsymbol{M} \times \boldsymbol{B} \qquad [5]$$

To further simplify the mathematics, we will introduce a new coordinate system, known as the rotating frame of reference. The rotating frame is a coordinate system whose transverse plane is rotating clockwise at an angular frequency ω, which is equal to the Larmor frequency (Figure 6). To distinguish this new rotating frame from the conventional stationary frame, we use x', y', and z' to denote the three orthogonal axes of this frame, and correspondingly, $\boldsymbol{i'}$, $\boldsymbol{j'}$, and $\boldsymbol{k'}$ as their unit directional vectors.

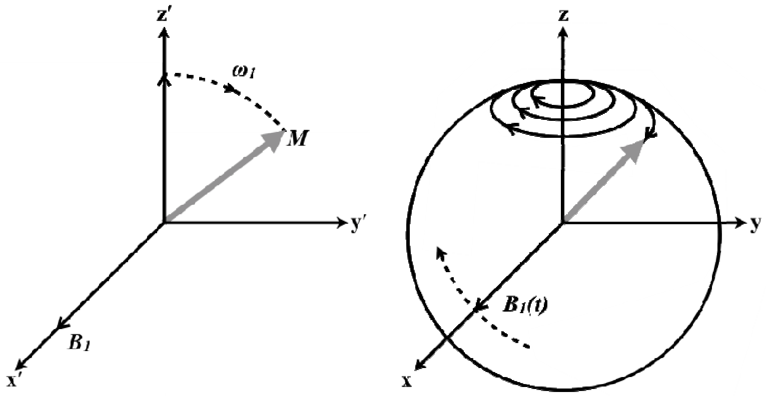

Figure 6. Motion of the bulk magnetization in the presence of a rotating RF field, $B_1(t)$, as observed in (A) the rotating frame and (B) the stationary frame.

Equation 5 can be expressed in the new rotating frame as:

$$\frac{\partial \boldsymbol{M_{rot}}}{\partial t} = \gamma \boldsymbol{M_{rot}} \times \boldsymbol{B_{eff}} \qquad [6]$$

where

$$\boldsymbol{B_{eff}} = \boldsymbol{B_{rot}} + \frac{\boldsymbol{\omega}}{\gamma} \qquad [7]$$

represents the effective magnetic field that the bulk magnetization vector experiences in the rotation frame.

Next, the effects of an RF pulse on a spin can be characterized by examining the behavior of ***M*** during the excitation period. In addition to its frequency, the applied RF pulse is characterized by its envelope function, B_1^e(t), and the phase of the applied RF pulse, φ. B_1^e(t) uniquely specifies the shape and duration of the RF pulse while φ defines the axis within the transverse plane that spins are rotated about by the RF pulse. Assuming a single spin resonating at the Larmor frequency and an applied RF pulse with an initial phase of zero and a pulse shape defined by B_1^e(t), the effective magnetic field from Eq. 7 can be re-written as:

$$\boldsymbol{B_{eff}} = \boldsymbol{B_1^e}\left(t\right) \qquad [8]$$

Substituting Eq. 8 into the Bloch equation result from Eq. 6 describes the bulk magnetization vector $\boldsymbol{M}$ in the rotating frame:

$$\frac{\partial \boldsymbol{M_{rot}}}{\partial t} = \gamma \boldsymbol{M_{rot}} \times \boldsymbol{B_1^e}\left(t\right) \qquad [9]$$

Equation 9 can be expressed in a more traditional scalar form as:

$$\begin{aligned} \frac{d\boldsymbol{M_{x'}}}{dt} &= 0 \\ \frac{d\boldsymbol{M_{y'}}}{dt} &= \gamma \boldsymbol{B_1^e}\left(t\right)\boldsymbol{M_{z'}} \\ \frac{d\boldsymbol{M_{z'}}}{dt} &= -\gamma \boldsymbol{B_1^e}\left(t\right)\boldsymbol{M_{y'}} \end{aligned} \qquad [10]$$

A closed form solution to Eq. 10 under the initial conditions of $M_{x'}(0) = M_{y'}(0) = 0$ and $M_{z'}(0) = M_z^0$ yields:

$$\begin{aligned} \boldsymbol{M_{x'}}\left(t\right) &= 0 \\ \boldsymbol{M_{y'}}\left(t\right) &= \boldsymbol{M_z^0} sin\left(\int_0^t \gamma \boldsymbol{B_1^e}\left(t\right)dt\right) \\ \boldsymbol{M_{z'}}\left(t\right) &= \boldsymbol{M_z^0} cos\left(\int_0^t \gamma \boldsymbol{B_1^e}\left(t\right)dt\right) \end{aligned} \qquad [11]$$

These equations indicate that the effect of the on-resonance excitation B_1 field, as observed in the rotating frame, is a precession of the bulk magnetization about the x'-axis. The precession of $\boldsymbol{M}$ about the B_1 field is called forced precession. The applied RF pulse leads to forced precession, which tips the bulk magnetization away from the z'-axis, resulting in a measureable transverse magnetization, component $\boldsymbol{M_{xy}}$. An RF pulse of duration, t_{RF}, and flip angle, α, is described as the angle between $\boldsymbol{M}$ and the the z'-axis, which can be described by the following equation (Figure 7)

$$\alpha = \int_0^{t_{RF}} \boldsymbol{\omega_1}(t)\,dt = \int_0^{t_{RF}} \gamma \boldsymbol{B_1^e}(t)\,dt. \qquad [12]$$

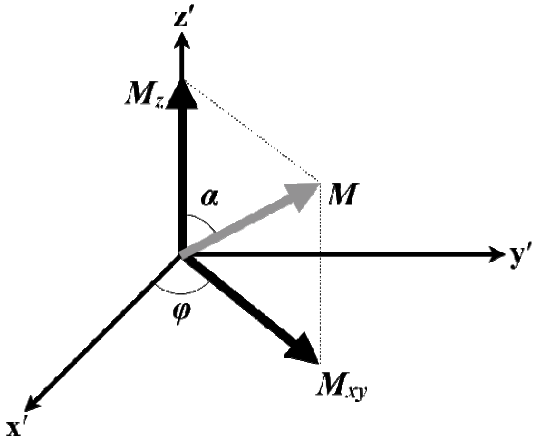

Figure 7. An RF pulse with an initial phase angle, *φ*, and flip angle, *α*, tips the magnetization into the transverse plane producing a measureable signal in MRI.

The signal magnetization (ignoring relaxation from T_1 and T_2) in the longitudinal, M_z, and transverse, $\boldsymbol{M_{xy}}$, planes can be calculated from Eqs. 11 and 12, where $\boldsymbol{M_{xy}} = M_x + iM_y$:

$$\begin{aligned} M_z &= M_z^0 cos\left(\alpha\right) \\ M_{xy} &= M_z^0 sin\left(\alpha\right) \end{aligned} \qquad [13]$$

MAGNETIC FIELD GRADIENTS

Up to this point, two of the main components of MRI hardware have been discussed: the main magnetic field, B_0, and the rotating RF magnetic field, B_1. A third and final magnetic field component is used to determine the physical location of the signal generated by B_0 and B_1. This component, known as the magnetic field gradient system, consists of three orthogonal gradient coils (Figure 8), which are designed to produce a time-varying magnetic field. These gradient coils are referred to as the x-gradient, y-gradient, and z-gradient, which vary the z-component of the magnetic field linearly along the x-, y-, and z-directions, respectively. The overall magnetic field in the presence of a gradient field can be expressed as

$$\boldsymbol{B} = (\boldsymbol{B_0} + \boldsymbol{G} \cdot \boldsymbol{r})\, \boldsymbol{k} \qquad [14]$$

where

$$\boldsymbol{G} = (G_x, G_y, G_z) = G_x\boldsymbol{i} + G_y\boldsymbol{j} + G_z\boldsymbol{k}. \qquad [15]$$

Magnetic field gradients are usually defined by their gradient amplitude or strength, the rate at which this maximum gradient strength can be achieved, which determines the duration of the gradient risetime, and the applied gradient direction. Gradient strength is normally measured in units of millitesla per meter (mT/m) and a higher value represents a stronger gradient. The rate at which this gradient strength is achieved is referred to as the gradient slew rate and is normally measured in units of millitesla per meter per millisecond (mT/m/ms). A larger slew rate means the gradient reaches is maximum strength faster than a smaller slew rate.

When a gradient is applied, the magnetic field strength that a spin experiences is increased/decreased depending on the spins position with respect to the magnet isocenter. This change in magnetic field leads to an increases/decreases in the spins precessional frequency based on (Eqs. 3 and 14). Changes in precessional frequency lead to changes in the phase of the spins, which allow each spin to be uniquely identified based on their location with respect to the main magnetic field and magnetic field gradient.

SPATIAL ENCODING

Previously, it has been described how an object placed in the presence of a main magnetic field and excited by an RF generates a signal, $\boldsymbol{M_{xy}}$, which can be detected via Faraday's Law of induction and a nearby and appropriately tuned coil. The generated signal is the sum of the local signals from all parts of the object. Since most objects imaged in MRI are heterogeneous, such as the human body, we need to isolate the spatial origin of the measured signal to differentiate local signals from different parts of the imaged object. This process, known as spatial localization, is achieved by means of selective excitation and spatial encoding. Central to both forms of spatial localization are magnetic field gradients, which are used to produce local signals with distinct spatial information.

Slice selection is the simplest form of selective excitation and is the first step to spatial localization. Slice selection involves both a magnetic field gradient and an RF pulse. RF excitation was previously described as an oscillating magnetic field gradient. An RF pulse transmitted at the Larmor frequency (i.e. the frequency of the oscillating RF magnetic field matches the resonance frequency of hydrogen nuclei) will produce transverse magnetization and a signal from the entire imaged object. Conversely, if the RF pulse is transmitted at a frequency that does not match the Larmor frequency, excitation of the hydrogen nuclei will not occur and no transverse magnetization will be generated. However, if the magnetic field varies spatially, then parallel planes within the imaged object will have a distinct frequency. Magnetic field gradients are applied in the direction of the desired slice selection to vary the magnetic field spatially along that direction (Figure 8).

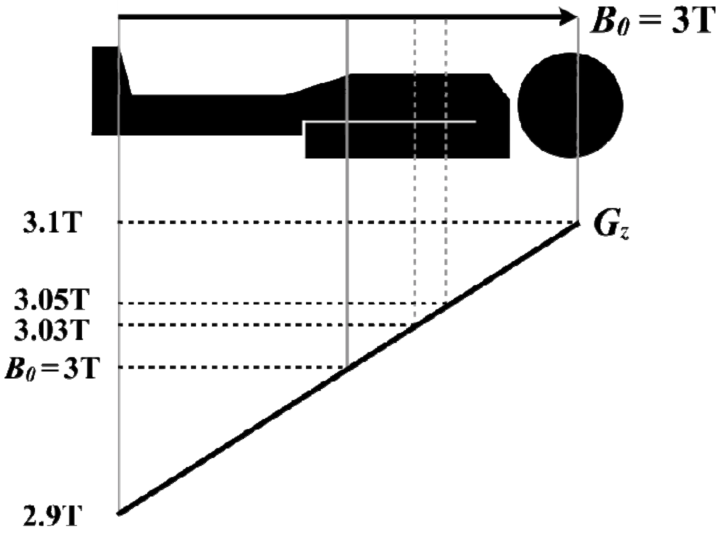

Figure 8. A magnetic field gradient, G_z, applied along the direction of the main magnetic field, B_0, spatially alters the magnetic field strength to be higher (3.1T) or lower (2.9T) than the main magnetic field, B_0 = 3T.

The application of a magnetic field gradient and an RF pulse at a range of frequencies results in slice selection (Figure 9).

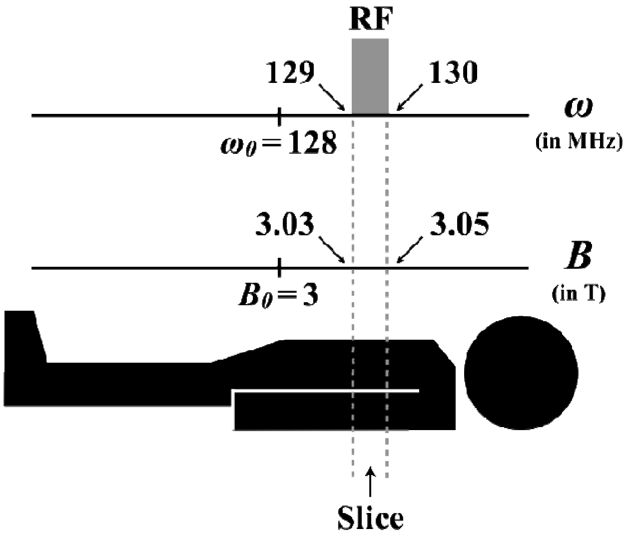

Figure 9. A spatially varying magnetic field produced by an external magnetic field, B_0, and an applied magnetic field gradient, G, in conjunction with an RF pulse applied at a range of frequencies, $\boldsymbol{\omega}$, results in slice selection.

To select a narrow band of frequencies the RF pulse needs to have a square shape in the frequency domain. The Fourier transform of a square shape in the frequency domain results in a sinc shape in the time domain. Figure 10 demonstrates this relationship and also relates the width of the applied sinc shaped RF pulse to the range of selected frequencies.

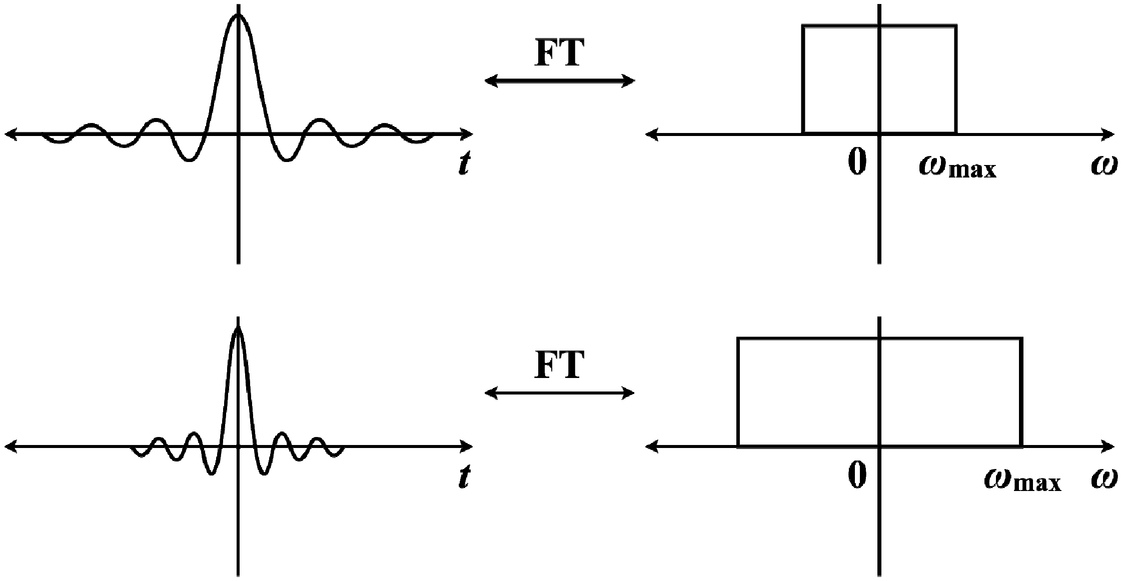

Figure 10. A square shape RF pulse in the frequency domain results in a sinc shaped RF pulse in the time domain. Additionally, a comparison of wide and narrow RF waveforms and their Fourier transforms illustrates that narrow RF pulses select a wide range of frequencies and wide RF pulses select a narrow range of frequencies.

An applied magnetic field gradient introduces a linear phase shift across the slice thickness. If uncorrected, this phase shift leads to undesirable signal loss. Due to the fact that the phase shift is a linear function of position, it can be removed by applying what is called a slice select refocusing gradient. Refocusing gradients are designed with the opposite polarity and half the area of the slice select gradient (Figure 11).

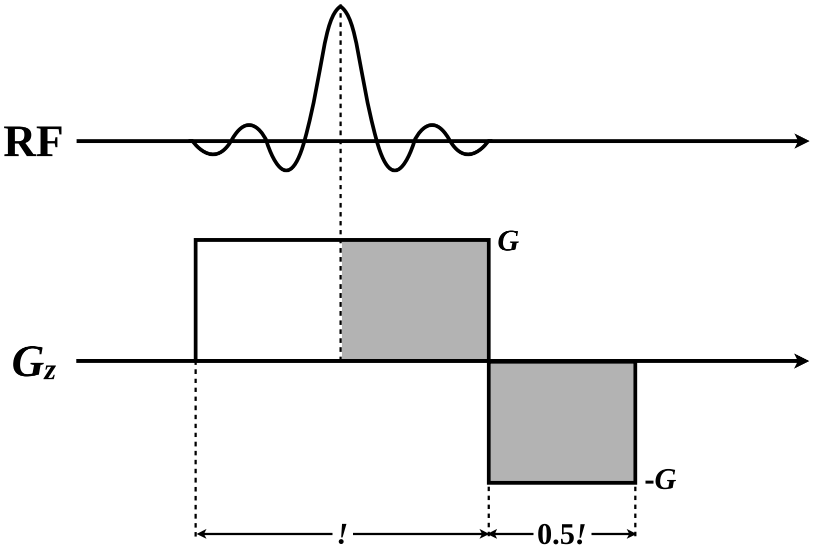

Figure 11. Slice select gradient, G_z, of amplitude G and duration τ and accompanying sinc shaped RF pulse of duration τ. The shaded grey region of the applied gradients indicates the spins have been refocused by the refocusing gradient of amplitude -G and duration 0.5τ.

Within the selected slice, all the spins have the same resonant frequency and thus it is impossible to differentiate the signal contribution of spins at different spatial locations. The next step is to spatially encode the measured signal along the x- and y-axis (assuming slice selection was conducted along the z-axis).

Phase encoding results in a change of the Larmor frequency along the y-axis through the use of an applied magnetic field gradient. Suppose a 3×3 spin matrix is selected through the use of a slice selection gradient as seen in Figure 12A.

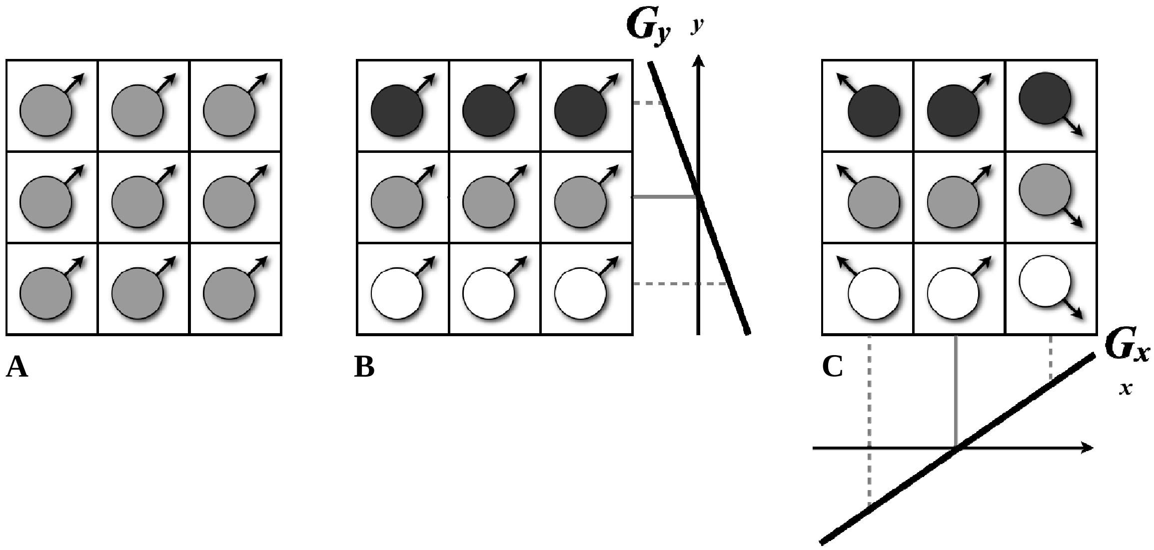

Figure 12. Following slice selection there is no way to associate the available signal to a given spatial coordinate as all spins possess the same frequency and phase (A). Phase encoding is achieved by applying a magnetic field gradient along the y-axis to induce a linear phase shift (different color) across the hydrogen nuclei (B). Following phase encoding, each spin has the same frequency with a phase that depends on their position along the direction of the applied phase encoding gradient (shown here as the y-axis). Frequency encoding is achieved by applying a magnetic field gradient along the x-axis to induce a linear frequency shift (arrow orientation) across the hydrogen nuclei (C). Following phase and frequency encoding, each spin in the resulting phase and frequency encoded 3×3 spin matrix has a unique frequency and phase that can be related to its position along the x- and y-axes.

A phase encoding gradient modifies the resonant frequencies of each hydrogen nuclei based on its position along the y-axis, inducing a phase, which persists after the gradient is turned off. This results in all the hydrogen nuclei precessing at the same frequency (orientation of the arrow in Figure 12A) but in different phases (color in Figure 12B) and leads to a unique phase component along the y-axis based on spatial location. Next, a frequency encoding gradient is applied to modify the resonant frequency along the x-axis. The result of both phase and frequency encoding produces a unique frequency and phase component of the signal for each hydrogen nuclei that is related to its spatial position along the x- and y-axis. Slice selection and spatial encoding allow the isolation of the spatial origin (x,y,z) of the measured signal, which allows differentiation of the local signals from different locations of the imaged object. Following the application of a low-pass filter and phase sensitive detection (details not described here) the measured signal following slice selection, phase encoding, and frequency encoding becomes

$$s\left(t\right) = \int_x \int_y M_{xy} e^{-i\gamma G_x x t} e^{-i\gamma G_y y t_{PE}} dx dy, \qquad [16]$$

where G_x and G_y are the frequency and phase encoding gradient amplitudes, respectively, x and y are the spatial position along the x- and y-axes, respectively, t is time, and t_{PE} is the duration of the phase encoding gradient.

IMAGE RECONSTRUCTION

Equation 16 represents the measured signal in the time domain. This signal is a combination of signals from all over the object being imaged. Any signal is composed of a series of sine waves, each with an individual frequency and amplitude. The Fourier transform allows us to determine what those frequencies and amplitudes are. That is to say, the Fourier transform converts the signal from the time domain into the frequency domain. The signal in MR is encoded using magnetic field gradients, which relate frequency and (rate of change of) phase to position. The separation of these frequencies allows an image to be comprised of the amplitude of these signals within an image.

At this point, two new terms k_x(t) and k_y(t), need to be introduced as the time integrals of G_x(t) and G_y(t)

$$\begin{aligned} k_x(t) &= \frac{\gamma}{2\pi}\int_0^t G_x(s)\,ds \\ k_y(t) &= \frac{\gamma}{2\pi}\int_0^t G_y(s)\,ds. \end{aligned} \qquad [17]$$

Both k_x(t) and k_y(t) represent the frequency space (or k-space) coordinates of the path followed by the frequency and phase encoding gradients, G_x and G_y. In the simplified case of constant gradient waveforms (i.e. rectangular shaped gradient pulses) both G_x and G_y are constant. Thus, Eqs. 16 and 17 produce the following signal in k-space:

$$s(k) = \int_x \int_y M_{xy} e^{-i2\pi k_x x} e^{-i2\pi k_y y}\,dx\,dy. \qquad [18]$$

Taking the inverse Fourier transform of the complete k-space signal of Eq. 18, which is repeated for each phase encoding step, results in the final measured signal in image space. The final reconstructed signal for each x and y pixel location in the image is thus

$$I(x,y) = \int_{k_x} \int_{k_y} s(k) e^{i2\pi k_x x} e^{i2\pi k_y y}\,dk_x\,dk_y. \qquad [19]$$

GRADIENT RECALLED ECHO IMAGING

Using the principles of nuclear magnetic resonance in combination with RF excitation and spatial encoding by magnetic field gradients, there are many ways to form an image. One of the more common types of image acquisition strategies is called Gradient Recalled Echo (GRE) imaging. A basic overview of a typical GRE imaging sequence is shown in Figure 13 through a schematic diagram that details the application of the RF pulse(s) and gradient waveforms known as a pulse sequence diagram.

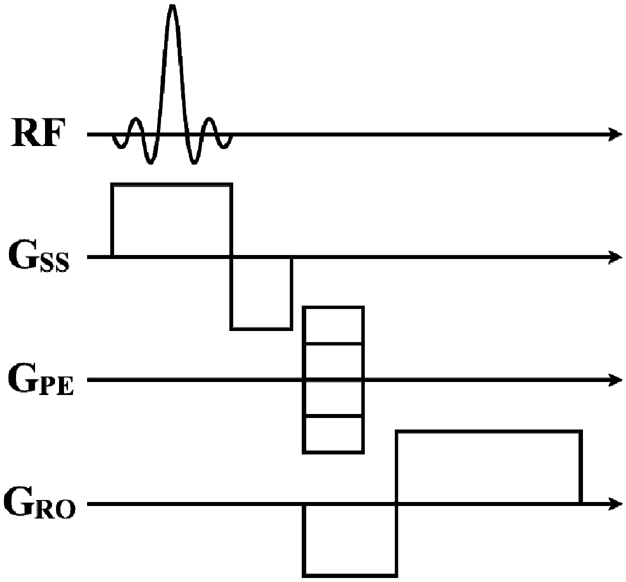

Figure 13. Pulse sequence diagram of a standard GRE imaging sequence showing the application of a radiofrequency pulse (RF), slice select encoding gradient (SS), phase encoding gradient (PE), and the frequency encoding readout gradient (RO).

An initial RF pulse is played to produce transverse magnetization. Phase encoding and frequency encoding gradients are played to produce a linear spatial variation in the phase and frequency of the magnetization along the phase and frequency direction. The formation of a gradient echo (signal) results from applying a dephasing gradient before the frequency encoding readout gradient. The goal of this dephasing gradient is to obtain the peak of the echo in the middle of the readout gradient when the data are acquired. The time during which the peak signal is obtained is called the Echo Time (TE). The dephasing readout gradient has the opposite polarity of the readout gradient applied during data acquisition. Moreover, its dephasing effect is designed so that it corresponds to half of the dephasing effect of the readout gradient during data acquisition (i.e. half the area of the readout gradient during data acquisition). Consequently, during data acquisition, the readout gradient will rephase the spins in the first half of the readout (by reversing the dephasing effect of the dephasing lobe), and the spins will dephase in the second half (due to the dephasing effect of the readout gradient). The phase encoding gradient area is varied to fill k-space based on the desired image matrix size N_{PE}, field-of-view (FOV_{PE}), and pixel size, Δy, in the phase encode direction. From Eq. [17] the location in k-space for phase encode line n is:

$$k_{PE}(n) = \frac{\gamma}{2\pi} \int_0^t G_{PE}\left(n, t\right) dt = \frac{\gamma}{2\pi} A_{PE}\left(n\right), \tag{20}$$

where $A_{PE}(n)$ is the area of the phase encoding gradient for line n. Thus, a different phase encoding gradient is needed for each line in k-space. The distance in k-space between one phase encoding line and the other (Δky, where Δky = $k_{PE}(n+1) - k_{PE}(n)$) must be chosen such that:

$$\Delta k_{PE} = \frac{1}{FOV_{PE}} = \frac{1}{N_{PE}\Delta y}. \tag{21}$$

The frequency encoding readout gradient area is similarly determined by the desired image matrix size N_{RO}, field-of-view (FOV_{RO}), pixel size, Δx, and readout bandwidth (sampling rate), 1/Δt, in the frequency encode direction (see Eq. 24 below). The duration of data acquisition, T_{acq}, is determined by the readout receiver bandwidth, Δf, and the number of k-space lines in the frequency encode direction, N_{RO}:

$$T_{acq} = \frac{N_{RO}}{2\Delta f}. \tag{22}$$

Similar to Eq. [20], the location in k-space for frequency encode line n is:

$$k_{RO}(n) = \frac{\gamma}{2\pi}\int_0^t G_{RO}\,(t)\,dt = \frac{\gamma G_{RO} T_{acq}}{2\pi N_{RO}}, \qquad [23]$$

while the distance in k-space between one frequency encoding readout point and the other must be chosen such that:

$$\Delta k_{RO} = \frac{1}{FOV_{RO}} = \frac{1}{N_{RO}\Delta x}. \qquad [24]$$

The gradient amplitude for the plateau duration of the readout gradient can be determined by combining Eqs. [22-24]:

$$G_{RO} = \frac{4\pi\Delta f}{\gamma FOV_{RO}}. \qquad [25]$$

Figure 14 shows how a GRE pulse sequence diagram results in acquisition of data in k-space and the resulting image after applying the Fourier transform.

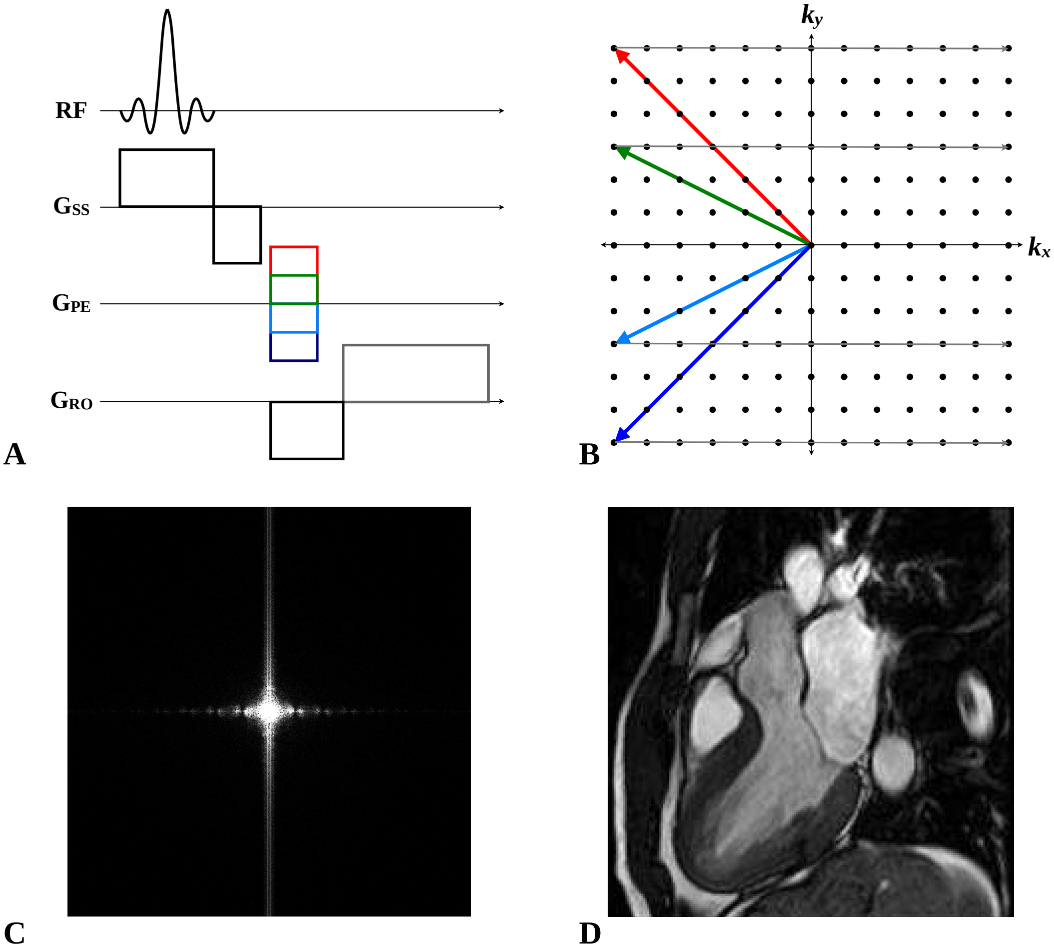

Figure 14. Pulse sequence diagram of a standard GRE imaging sequence (A) and corresponding k-space acquisition (B) resulting in the final magnitude k-space data (C) and image space data following the application of the Fourier transform (D).

CHAPTER 2

CARDIOVASCULAR MAGNETIC RESONANCE IMAGING

Acquiring MRI images of the cardiovascular system is complicated by the intrinsic motion of the heart during image acquisition. To enable imaging of the heart while it beats, images are acquired in segments during different time points throughout the cardiac cycle and pieced together to create a movie of a single heart beat comprised of image data acquired during several heartbeats. This requires longer scan times compared to standard non-segmented imaging, but enables imaging of the heart as it beats. Additionally, respiratory motion can pose a problem during cardiac MR acquisitions, but this is commonly avoided by having the patient hold their breath during image acquisition. This chapter discusses the main techniques used to make cardiac MRI feasible in the presence of cardiac motion

CARDIAC TRIGGERING AND SEGMENTATION

An electrocardiogram (ECG) records the electrical activity of the heart as detected by electrodes, which are attached to the surface of the skin and recorded by a device external to the body. The most prominent characteristic of a typical ECG signal is the QRS complex, which reflects the depolarization of the right and left ventricles just prior to contraction. In particular, the R amplitude is generally the most significant feature in the ECG signal and can easily be distinguished from other electrical events during the cardiac cycle. The time between two consecutive R-peaks (RR-interval) can therefore serve as a trigger for data acquisition. More specifically, the detection of the R-wave can be used to synchronize MR imaging with the cardiac cycle, which is commonly referred to as cardiac triggering.

There are two types of cardiac synchronization used in MR imaging methods: prospective triggering and retrospective gating (Figure 15). Prospectively triggered ECG pulse sequences make use of trigger delays and acquisition windows for data acquisition. Following the detection of an RR-interval, an optional trigger delay prolongs the start of image acquisition after which image acquisition begins for a duration specified by the user. Afterwards, there exists another delay, which represents the difference of the RR-interval and the user-specified acquisition window. Only a portion of the k-space data, called a segment, is acquired during each heartbeat. Following this delay, another RR-interval is detected and the process is repeated to acquire additional k-space segments. This process is repeated for as many heartbeats as needed to fill all of k-space. For retrospectively gated pulse sequences, the detection of an RR-interval initiates data acquisition, which continues until the detection of the next RR-interval. Unlike prospective ECG triggering, retrospective ECG gating updates the next segment without a gap.

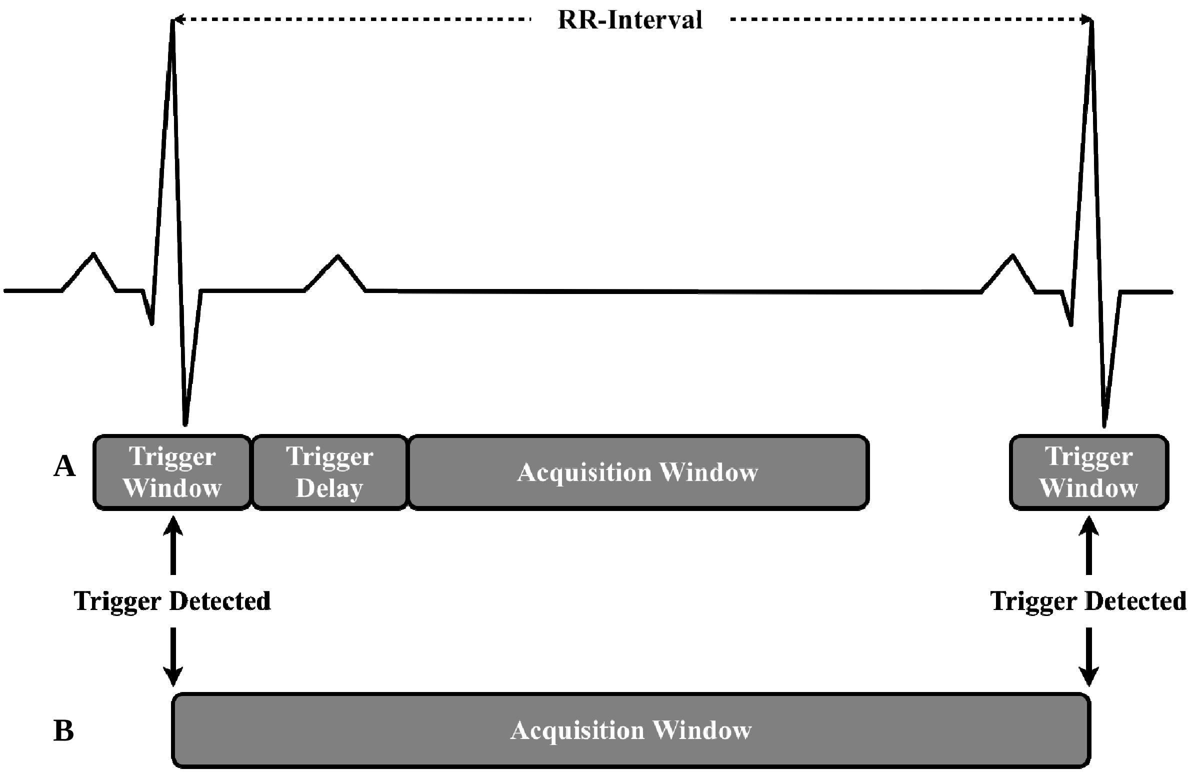

Figure 15. Depiction of prospective triggering (A) and retrospective gating (B).

Cardiac segmentation is used to reduce the total imaging time of for cardiac cine imaging (Figure 16). Each segment is then used to acquire 1/Nth of the image data during a single heartbeat, where N is the total number of heart beats required to reconstruct a cardiac cine representing the motion of a single heart beat, “averaged” over N heart beats. Each image of the cardiac cine represents a snapshot of the heart’s motion corresponding to a certain time point in the cardiac cycle. The individual images of the cardiac cine are referred to as cardiac phases. The number of k-space lines acquired during each segment is called the views per segment (VPS). As the number of imaging segments increases, more lines of k-space are collected during one cardiac phase, resulting in a reduction in the total acquisition time at the expense of reduced temporal resolution, T_{Res}.

$$
\begin{aligned}
T_{Res} &= TR \times VPS, & & [1] \\
\text{Cardiac Phases} &= \frac{\text{RR-interval}}{T_{Res}}, & & [2] \\
\text{Acquisition Time} &= \frac{N_{PE}}{VPS} & \text{(heart beats)}, \quad & [3] \\
&= \frac{N_{PE}}{VPS} \times \text{RR-interval} & \text{(seconds)}. \quad & [4]
\end{aligned}
$$

Equations [1-4] show that segmented MR imaging represents a tradeoff between total acquisition time (in either heartbeats or seconds) and temporal resolution.

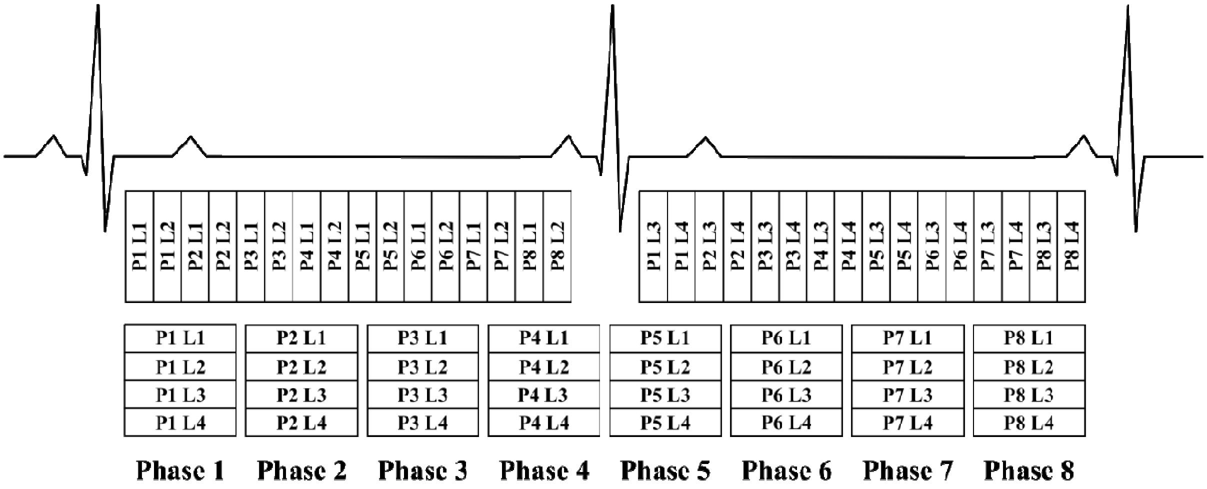

Figure 16. Segmented k-space for a multiphase cardiac MR image acquisition with N_{PE} = 4 and VPS = 2 leading to 8 cardiac phases reconstructed over the course of 2 heart beats. The nomenclature (P# and L#) refers to the cardiac phase # and k-space line #. Note, for example, that lines 1 and 2 are acquired repeatedly during the first heart beat. Typical cardiac MR imaging sequences use TR~5ms, N_{PE}=192, and VPS=10 (not depicted here for simplicity and to save space), which would result in 20 cardiac phases reconstructed with a 50ms temporal resolution and require 20 heart beats, or 19.2 second breath hold duration for a 1 second RR-interval (60 beats per minute heart rate).

CHAPTER 3

PHASE CONTRAST MAGNETIC RESONANCE IMAGING

MRI techniques offer a non-invasive imaging method for the highly accurate anatomic depiction of the heart and vessels. In addition, the intrinsic sensitivity of MRI to tissue motion offers the possibility to acquire spatially registered functional information simultaneously with morphological data. Most MRI sequences demonstrate sensitivity to flow and motion, which can often lead to undesired image artifacts for many applications. However, the intrinsic motion sensitivity of MRI can also be applied with flexible spatial and temporal resolution (4,5) in a variety of applications to quantify cardiovascular function and hemodynamics. In particular, Phase Contrast MRI (PC-MRI) enables clinicians to evaluate vascular flow, cardiac output, ventricular function, valvular regurgitation, stenotic flow velocities, pulmonary-systemic shunt volumes, vessel wall shear stress, pulse wave velocities, pressure gradients, and myocardial motion (18,19).

VELOCITY ENCODING

As previously described, the signal in MRI, $\boldsymbol{M}_{xy}$, is a vector quantity, thereby having a magnitude and phase component. Traditionally, MR images are viewed by looking at the magnitude of $\boldsymbol{M}_{xy}$, but phase images can similarly be constructed (Figure 17). The evolution of the MR signal phase for moving spins can be derived from the precessional frequency of the spins in a local magnetic field. The Larmor frequency of the spins at any time and location, $\omega(\boldsymbol{r},t)$, in the presence of a static magnetic field B_0, local field inhomogeneity ΔB_0, and an applied time varying magnetic field gradient $\boldsymbol{G}(t)$ is given by

$$\omega\left(\boldsymbol{r},t\right)=\gamma B_z\left(\boldsymbol{r},t\right)=\gamma B_0+\gamma\Delta B_0+\gamma\boldsymbol{r}\left(t\right)\cdot\boldsymbol{G}\left(t\right). \qquad [1]$$

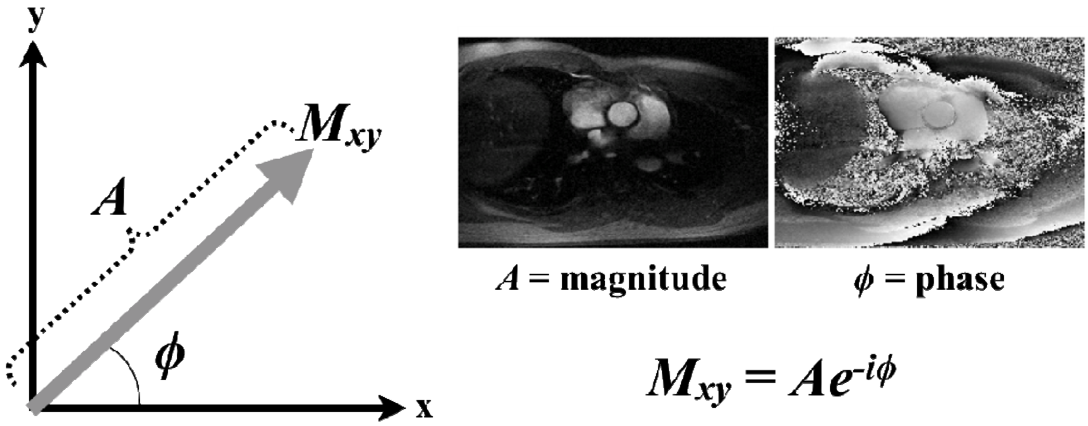

Figure 17. The measured complex signal, $\boldsymbol{M}_{xy}$, can be used to construct a magnitude and/or phase image.

After signal reception, the acquired signal is demodulated with respect to the Larmor frequency in the static magnetic field (transformation of the MR signal into the rotating frame of reference, which results in exclusion of the main magnetic field term, B_0, from Eq. [1]). Integration of Eq. [1] results in the phase of the corresponding measured signal after an applied RF pulse (at t_0) at the time of the echo (TE):

$$\begin{aligned}\phi\left(\boldsymbol{r}, TE\right) &= \phi\left(\boldsymbol{r}, t_0\right) + \int_{t_0}^{TE} \omega\left(\boldsymbol{r}, t_0\right) dt \\ &= \phi\left(\boldsymbol{r}, t_0\right) + \gamma \Delta B_0 \left(TE - t_0\right) + \gamma \int_{t_0}^{TE} \boldsymbol{G}(t)\boldsymbol{r}(t) dt. \qquad [2]\end{aligned}$$

Using a Taylor series expansion, Eq. [2] can be re-written as

$$\phi\left(\boldsymbol{r}, TE\right) = \phi_0 + \sum_{n=0}^{\infty} \gamma \frac{\boldsymbol{r}^{(n)}}{n!} \int_{t_0}^{TE} \boldsymbol{G}(t)(t - t_0)^n dt. \qquad [3]$$

with $\boldsymbol{r}^{(n)}$ representing the motion of the imaged tissue (described below). If the motion of the imaged tissue does not change fast with respect to the temporal resolution of data acquisition, then the corresponding velocities can be approximated to be constant during data acquisition. Thus $\boldsymbol{r}(t)$ can be represented as a first order displacement $\boldsymbol{r}(t) = \boldsymbol{r}_0 + \boldsymbol{v}(t - t_0)$. Equation [3] can then be simplified as

$$\phi(\boldsymbol{r}, TE) = \phi_0 + \gamma \boldsymbol{r}_0 \int_0^{TE} \boldsymbol{G}(t)dt + \gamma \boldsymbol{v} \int_0^{TE} \boldsymbol{G}(t)tdt, \qquad [4]$$

where the zero and first order gradient components describe the influence of magnetic field gradients on spins with position, $\boldsymbol{r}$, and velocity, $\boldsymbol{v}$, respectively:

$$\boldsymbol{M}_0 = \int_0^{TE} \boldsymbol{G}(t)dt \qquad [5a]$$

$$\boldsymbol{M}_1 = \int_0^{TE} \boldsymbol{G}(t)tdt. \qquad [5b]$$

Equations 5a and 5b shows the integrals describing the contribution of the magnetic field gradients are also known as n^{th} order gradient moments $\boldsymbol{M}_n$ such that the first gradient moment $\boldsymbol{M}_1$ determines the velocity induced signal phase for moving spins while the zero gradient moment $\boldsymbol{M}_0$ determines the position induced signal phase for stationary spins. When $\boldsymbol{M}_0 = 0$ to refocus the position-related phase (Chapter 1), the measured phase in Eq. [4] depends on the velocity of the imaged tissue:

$$\phi(\boldsymbol{r}, TE) = \phi_0 \qquad [6a]$$

$$\phi(\boldsymbol{r}, TE) = \phi_0 + \gamma \boldsymbol{M}_1 \cdot \boldsymbol{v}, \qquad [6b]$$

where Eq. [6a] represents the measured phase for stationary tissue ($\boldsymbol{v} = 0$) and Eq. [7] represents the measured phase for moving tissue ($\boldsymbol{v} \neq 0$). As a result, the first gradient moments can be manipulated to specifically encode information about a spins position and/or velocity, which is directly related to the measured phase.

GRADIENT MOMENTS

Gradient moments were described mathematically in Eq. [5]. The zero gradient moment, $\boldsymbol{M_0}$, represents the area of the gradient waveform and has units of mT/m/ms. The first gradient moment, $\boldsymbol{M_1}$, represents the product of area of the gradient waveform and it's duration, which has units of mT/m/ms^2. These values are better understood by visualizing the gradient waveforms and their corresponding moments (Figure 18). A simple positively lobed trapezoid gradient waveform results in a non-zero $\boldsymbol{M_0}$ and $\boldsymbol{M_1}$. A bi-polar trapezoid gradient waveform results in $\boldsymbol{M_0} = 0$ and a non-zero $\boldsymbol{M_1}$. A tri-polar trapezoid gradient waveform, which is commonly referred to as a flow compensated waveform, results in $\boldsymbol{M_0} = \boldsymbol{M_1} = 0$.

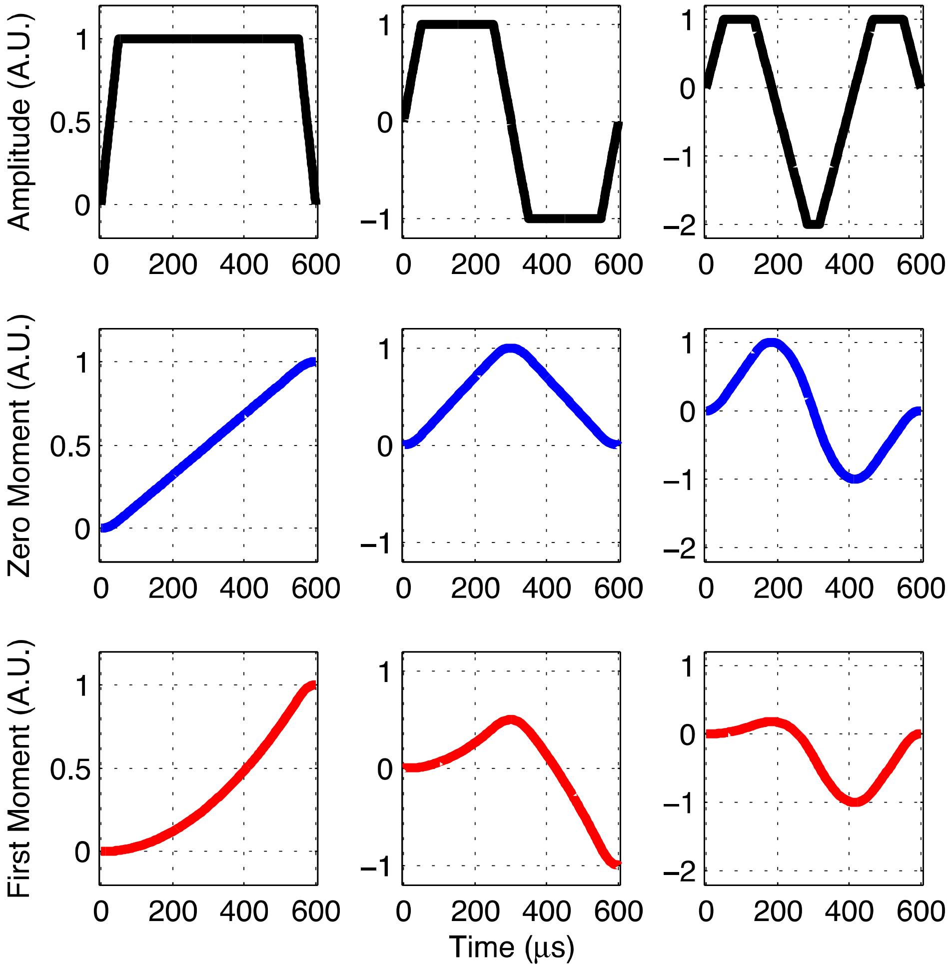

Figure 18. Different gradient waveforms and their corresponding zero (blue), $\boldsymbol{M_0}$, and first (red), $\boldsymbol{M_1}$, moments.

By applying gradient waveforms with specific $\boldsymbol{M_0}$ and $\boldsymbol{M_1}$ characteristics, the measured phase from Eq. [4] can be dependent upon both a spins position and velocity, just the spins position, or just the spins velocity. For example, the application of a gradient waveform with non-zero values for $\boldsymbol{M_0}$ and $\boldsymbol{M_1}$ results in a measured phase that depends on the spins position and velocity. Similarly, a gradient waveform with $\boldsymbol{M_1} = 0$ and a non-zero $\boldsymbol{M_0}$ results in a measured phase that depends on the spins position. Finally, a gradient waveform with $\boldsymbol{M_0} = 0$ and a non-zero $\boldsymbol{M_1}$ results in a measured phase that depends on the spins velocity, which is the primary objective in PC-MRI. However, background phase arising from magnetic field susceptibility and/or magnetic field inhomogeneity ($\square_0$ in Eq. [4]) cannot be eliminated by manipulating the gradient moments. As a result, typical PC-MRI experiments use two measurements with different gradient waveforms for cancellation of these phase errors (14-16). In each measurement, the gradient waveforms are designed to null $\boldsymbol{M}_0$, $\boldsymbol{M}_{0,1} = \boldsymbol{M}_{0,2} = 0$ (where $\boldsymbol{M}_{0,1}$ and $\boldsymbol{M}_{0,2}$ are the zero gradient moment for the first and second measurement, respectively), to refocus the position-related phase, but with a net difference in $\boldsymbol{M}_1$, $\Delta\boldsymbol{M}_1 = \boldsymbol{M}_{1,1} - \boldsymbol{M}_{1,2}$, to yield provide a velocity dependent phase that is devoid of $\square_0$:

$$\phi\left(\boldsymbol{r}, TE\right) = \gamma \boldsymbol{v} \cdot \left(\boldsymbol{M}_{1,1} - \boldsymbol{M}_{1,2}\right) = \gamma \boldsymbol{v} \cdot \Delta \boldsymbol{M}_1. \qquad [7]$$

In Eq. [7], $\phi\,(\boldsymbol{r},TE)$ is the phase difference between the two velocity encoded images, γ is the gyromagnetic ratio, $\boldsymbol{v}$ is the velocity, and $\boldsymbol{M}_{1,1}$ and $\boldsymbol{M}_{1,2}$ are the first gradient moments for the two measurements, which produce a net difference of $\Delta\boldsymbol{M}_1$. Phase images can be reconstructed with values ranging from $[-\pi,+\pi]$. The velocity encoding strength (VENC), defined as the velocity that produces a phase shift of $|\pi|$ radians, is determined by $\Delta\boldsymbol{M}_1$:

$$VENC = \frac{\pi}{\gamma |\Delta \boldsymbol{M}_1|}. \qquad [8]$$

The desired VENC is achieved by manipulating $\boldsymbol{M}_{1,1}$ and $\boldsymbol{M}_{1,2}$, which can be done using several velocity encoding strategies.

VELOCITY ENCODING STRATEGIES

The target ΔM_1 is achieved by acquiring two velocity encoded acquisitions of the form:

$$M_{1,1} = \alpha \Delta M_1 \qquad [9a]$$

$$M_{1,2} = (\alpha - 1)\, \Delta M_1, \qquad [9b]$$

where α describes first moment distribution and depends on the selected velocity encoding strategy. Conventionally, velocity encoding is employed by using either a pair of equal and opposite bipolar flow encoding gradients (Bipolar) or a set of flow compensated and flow encoded gradients (FCFE). Bipolar encoding is designed with α = 0.5 (14,15) while FCFE is designed with α = 0 (16,17). Although not widely appreciated, Bipolar velocity encoding is more time-efficient for low VENCs, which is important for measuring cerebral spinal fluid (CSF) flow and myocardial motion, while FCFE is more time efficient for mid to high VENCs (Figure 20). Furthermore, FCFE has reduced signal loss during the flow compensated acquisition images due to intravoxel velocity-related phase dispersion (20,21) and reduced ghosting artifacts in the phase encode direction arising from large $\boldsymbol{M_1}$ induced velocity-related phase shifts (15).

Both velocity encoding strategies demand specific values of α to produce the required ΔM_1 in Eq. [9]. This requirement can be inefficient and typically leads to velocity encoding gradient waveforms that are unequal in duration, which limits the minimum achievable TE/TR. Bernstein et al. (22) used velocity encoding gradients without constraining α. The only requirement was that the encoding acquisitions produced the required $\Delta\boldsymbol{M_1}$. This results in shorter velocity encoding gradient waveforms compared to FCFE and Bipolar encoding methods. Although not widely adopted, this velocity encoding strategy, referred to as asymmetric velocity encoding and discussed further in Chapters 7 and 8, results in the shortest velocity encoding gradient durations and concomitant reductions in TE/TR.

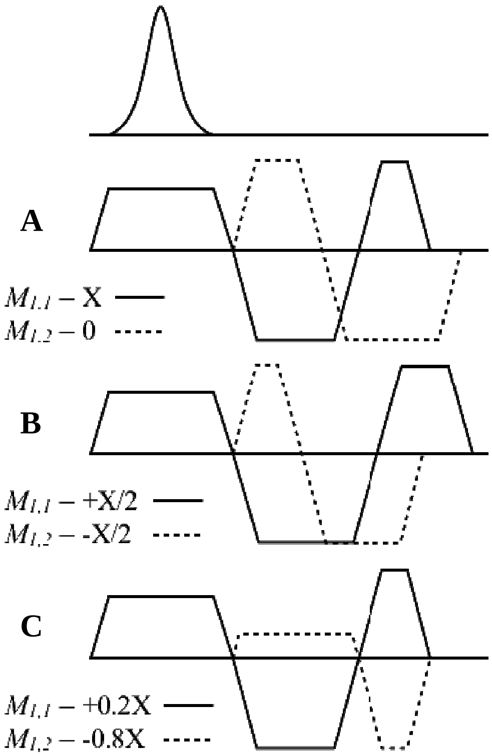

Figure 19. Comparison of FCFE (A), Bipolar (B), and Asymmetric (C) velocity encoding strategies for the same imaging parameters and VENC. $M_{1,1}$ and $M_{1,2}$ represents the first gradient moments for each PC-MRI experiment. ΔM_1=X for all methods. Asymmetric encoding always achieves the target ΔM_1 (i.e. VENC) the fastest.

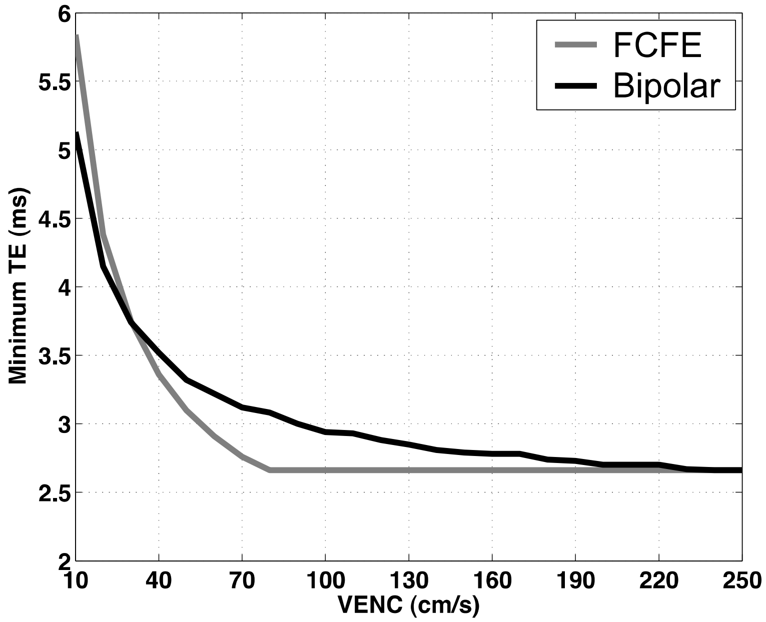

Figure 20. Minimum achievable TE (ms) plotted as a function of the target VENC (cm/s) for conventional Bipolar (grey) and FCFE (black). Imaging parameters were 192 × 120 encoding matrix, 1.6 mm × 1.6 mm × 5 mm acquisition voxel, 30° flip angle, 4 views-per-segment, 600 μs RF pulse width, 814 Hz/px receiver bandwidth, and a maximum slew rate of 157 mT/m/ms.

CARDIAC IMAGE LOCALIZATION AND ACQUISITION

Before PC-MRI measurements can be made, several steps are required in order to obtain specific views of the heart. After the patient is prepared and placed inside the MRI scanner, a three-plane scout image is acquired to begin localization. From an axial pseudo-long axis view of the heart, an imaging plane is defined, which passes through the base and apex of the left ventricle. This gives another oblique pseudo-long axis view of the heart. A 4-chamber view of the heart is obtained by again defining a plane through the base and apex of the left ventricle, providing a doubly-oblique view of the left and right atria and ventricles. A stack of short axis images of the heart are then acquired by defining multiple planes spanning from the apex of the left ventricle to the valves above the base of the heart. Next, a plane is defined by selecting three points within the aortic valve, mitral valve, and apex of the left ventricle. This provides a view of the left ventricular outflow tract (LVOT), which shows the left ventricle and the ascending aorta (aAo). A plane parallel to the aAo, gives us a view perpendicular to the LVOT. For PC-MRI images of the aAo above the level of the aortic valve, a final perpendicular plane distal to the aortic valve and coronary ostia is prescribed. From here aAo PC-MRI images are acquired. A complete overview of PC-MRI aAo localization is shown in Figure 5. Similarly, a view of the right ventricular outflow tract (RVOT), which shows the right ventricle and the main pulmonary artery (PA) is obtained by selecting three points within the pulmonary valve, tricuspid valve, and apex of the right ventricle. A plane parallel to the PA, gives us a view of the perpendicular RVOT. For PC-MRI images of the PA above the level of the pulmonary valve, a final perpendicular plane located downstream from the pulmonary valve and proximal to the first bifurcation is prescribed. From here PA PC-MRI images are acquired. Additionally, a stack of transverse black blood images at the level of the valves can be used to locate the pulmonary bifurcation where the PA splits into the right and left branch pulmonary arteries (RPA/LPA). RPA/LPA PC-MRI images are acquired by defining planes perpendicular to the RPA and LPA that are distal to the bifurcation. Once PC-MR images are acquired, careful post-processing must be completed to accurately convert measurements of phase into meaningful hemodynamic properties, such as blood velocity and flow.

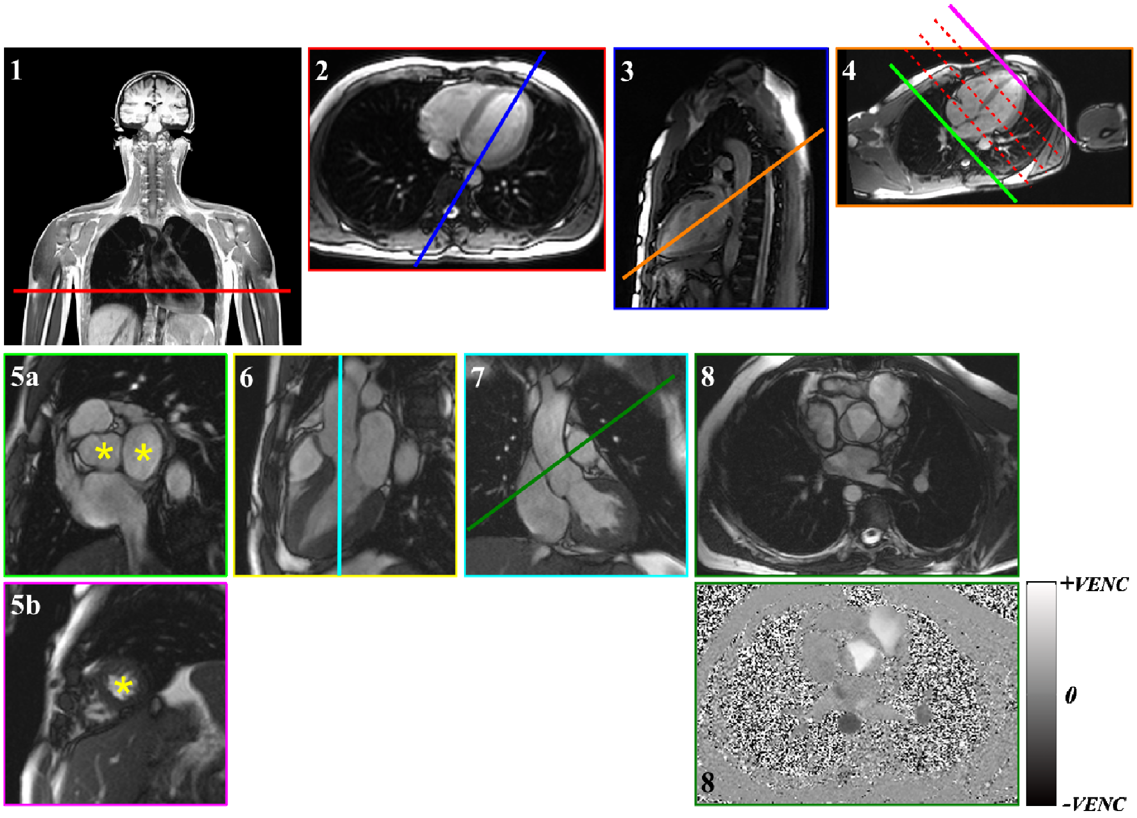

Figure 21. A detailed description of localization for the aortic valve. A coronal localizer (1) image is used to prescribe (red) a transverse long axis view of the heart (2). A plane prescribed through the base and apex of the left ventricle (blue) produces a sagittal long axis view of the heart (3). A four chamber view of the heart (4) is produced by prescribing a plane through the base and apex of the left ventricle (orange). A series of short axis transverse slices (sea green and magenta) of the heart are used to provide a view of the valves (5a) and the apex of the heart (5b). Three points defined within the aortic valve, mitral valve, and apex of the heart (yellow) produce a view of the left ventricular outflow tract (6). A plane is prescribed parallel to the aorta (cyan) to provide a perpendicular view of the left ventricular outflow tract (7). Another perpendicular plane (hunter green) is used to produce a view of the aortic valve (8), where blood flow can be measured (9).

QUANTITATIVE MEASURES OF BLOOD VELOCITY AND FLOW

Each pixel within a PC-MR image contains a phase measurement that is proportional to the velocity of moving spins. The pixel values range from [-π, π], which corresponds to [-VENC,+VENC]. First, a region-of-interest (ROI) must be contoured to include blood pixels within the lumen of the vessel of interest. From the pixels within this ROI, measurements of velocity and flow can be obtained. Measurements of velocity and flow can be computed by scaling the mean ROI signal intensity in the PC-MRI phase images by VENC/π, which assigns a velocity value to each pixel in units of cm/s. From this, the measured mean velocity within a ROI can be measured for each cardiac phase. The mean flow rate in units of mL/s can be calculated by multiplying the mean ROI velocities by the area of the ROI. Furthermore, the net flow in units of mL can be calculated by integrating the mean flow rate over the duration of the cardiac cycle. Similarly, the total forward or total reverse flow can be calculated by multiplying positive or negative mean ROI velocities by the area of the ROI, respectively.

BACKGROUND PHASE ERRORS

The application of a linear magnetic field gradient induces additional magnetic fields with non-linear spatial dependence (23). This is a consequence of Maxwell's equations for the divergence and curl of the magnetic field. Furthermore, considerable gradient non-linearities can introduce deviations from the nominal gradient strength and orientation (24). Both phenomena result in altered gradient moments used for velocity encoding. Resulting errors in the measured phase shifts used for velocity encoding due to deviations in the expected $\boldsymbol{M_0}$ and $\boldsymbol{M_1}$ values of the applied gradient waveforms, which can cause significant deviations in velocity quantification. Background phase errors arising from concomitant (Maxwell) gradient terms can be corrected through the application of online analytic correction techniques, which are commonly applied within the reconstruction framework of most vendors.

Time-varying magnetic fields (e.g. velocity encoding gradients) induce eddy currents in nearby conducting structures. Eddy currents create unwanted magnetic fields, which lead to phase errors in velocity measurements because they do not subtract in phase difference processing. Unlike the other background phase errors previously discussed, eddy currents cannot be corrected with an analytic solution. Non-compensated eddy current-induced background phase errors can introduce substantial errors in flow quantification. These errors result in a baseline shift of the velocity vs. time curve that is integrated to calculate blood flow. The magnitude of the baseline velocity shift depends on a number of imaging parameters, including where the imaging is conducted, relative to the magnetic isocenter, the imaging plane, and the velocity encoding strength. Importantly, small velocity offset errors often lead to much larger errors in blood flow quantification. This is because blood flow is calculated by integrating the velocity values within the cross-section of a vessel over time. Small velocity errors sum into a larger flow error that increases linearly with the cross-sectional area of the vessel. This is perhaps best illustrated with an example. Consider the measurement of aortic flow in a patient who has an aortic cross-sectional area of 5 cm^2. Assuming a VENC of 150 cm/s and a 1% velocity offset error (1.5 cm/s), a patient with a typical stroke volume of 80 mL/beat will have about a 10% error ($1.5 \text{ cm/s} \times 5 \text{ cm}^2 = 7.5 \text{ mL/s}$) in the measured flow due to eddy current-induced background phase errors. With this in mind, Gatehouse et. al (25) have established an acceptable eddy current threshold criteria. Based on theoretical calculations, a velocity offset error of 0.6 cm/s (representing just 0.4% of a VENC of 150 cm/s) is barely acceptable, potentially causing about 5% miscalculation of cardiac output and up to 10% error in shunt measurement.

Several eddy current correction methods have been proposed, which include image-based techniques and phantom calibration. Image-based techniques include the analysis of a background region of interest in stationary tissue adjacent to the vessel of interest, as well as using more distant stationary tissue and estimating phase offsets using linear or higher order interpolation (26-28). Errors can also be corrected by repeating the same imaging sequence with identical slice prescriptions and sequence parameters with a stationary fluid phantom and then subtracted from the patient PC-MRI phase images (29,30). Stationary phantom techniques, while widely considered to be the "gold standard" for eddy current velocity offset correction, are inefficient because they require additional measurements. Furthermore, image-based techniques may be inaccurate, particularly if there is insufficient stationary tissue in the acquisition plane, if stationary tissue signal is poor, or if velocity and/or image aliasing produces spatial non-linearity of phase offsets (25).

CLINICAL SIGNIFICANCE OF PC-MRI MEASUREMENTS

PC-MRI is a non-invasive, non-ionizing technique which can be used to accurately measure blood velocity and flow with flexible spatial and temporal resolution (4,5) and image orientation. PC-MRI has a range of established cardiovascular applications, especially in the diagnosis and treatment of congenital heart disease (CHD) and impaired heart valves (24, 25). There are many other interesting PC-MRI applications including the measurement of CSF flow and myocardial velocity mapping.

PC-MRI is considered the clinical ‘gold standard’ for non-invasive quantification of blood flow (31,32). Other methods of quantifying blood flow include cardiac catheterization and echocardiography. Cardiac catheterization is the ‘gold standard’ for evaluating hemodynamics, but ionizing radiation, invasiveness, and expense mean that “it is not a practical method for longitudinal follow-ups,” (6) which are needed to identify the optimal timing for clinical intervention. Ionizing radiation concerns also limit the repeated use of computed tomography and nuclear scintigraphy, especially in the case of CHD patients who will undergo a multitude of examinations throughout their lifetime. Body habitus combined with vessel angulation and the interposition of surgical scarring and the lungs limit the effectiveness of echocardiography (7-9). This is especially true for evaluation of the right heart, where echocardiography measures of branch pulmonary artery flow, pulmonary regurgitant fraction/volume, or flow in the main pulmonary artery is challenging.

PC-MRI is most commonly used to quantify vascular flow in the great vessels of the heart. Specifically, total, forward, and reverse flow can be evaluated in addition to measurements of mean and peak velocity. PC-MRI can be performed to calculate cardiac output (31,33) and in the presence of clinically significant valvular regurgitation enables more accurate assessment of cardiac output than does cine MRI. Impaired left ventricular filling, diastolic dysfunction, can be measured with PC-MRI in a variety of ways similar to the methods used in Doppler echocardiography. PC-MRI is a valuable tool for evaluating flow dynamics in CHD. Directionality and quantification of flow in anomalous vascular structures can be directly measured. Pulmonary-systemic shunts can be quantified by measurement of flow in the pulmonary trunk and aorta and calculation of the pulmonary to systemic blood flow ratio (Qp/Qs). PC-MRI can be used for the evaluation of valvular disease by measuring the regurgitant fraction (ratio of forward and reverse flow) across the aortic, pulmonary, mitral, and tricuspid valves. PC-MRI can also be used for measuring the slower velocities of myocardial wall motion, which can be used to obtain multidirectional velocity information similar to that obtained with tissue Doppler imaging without the limitations imposed by acoustic windows.

Despite decades of research, our ability to measure blood flow with phase contrast is still hampered by quantitative inaccuracies leading to clinically significant errors, which dampens clinical enthusiasm for the technique. Nevertheless PC-MRI continues to be a compelling clinical technique because of the need to non-invasively measure flow in a wide range of clinical contexts. Despite clinical preference and guidelines (2,7,10-13) suggesting the use of PC-MRI for flow measurements, its accuracy and reliability are frequently questioned due to poor internal consistency or inconsistent results compared to other clinical findings.

For example, the conservation of mass dictates that blood flow measured in the ascending aorta should be equal to blood flow measured in main and sum of the branch pulmonary arteries. Even in the absence of shunts and regurgitant flow, discrepancies between these territories frequently exist in the clinic. Results such as these continue to be a source of clinical frustration and in order for phase contrast to become an absolutely quantitative measure of flow, both the accuracy and precision of these measurements must be improved. What follows is the discussion and analysis of numerous sources of errors in PC-MRI blood flow measurements and the resulting proposed solutions in an effort towards absolutely quantitative PC-MRI flow measurements.

CHAPTER 4

CHEMICAL SHIFT-INDUCED PHASE ERRORS

In this chapter, PC-MRI errors arising from chemically shifted perivascular fat (Specific Aim #1) is discussed. Perivascular fat that surrounds most vessels can chemically shift across the vessel wall into the lumen. The complex fat signal then adds to the complex water signal and leads to a clinically significant measurement error that does not subtract in phase difference imaging. Herein we define the effects of chemically shifted perivascular fat in PC-MRI and develop a coherent error reduction strategy. We ***hypothesize*** that chemical shift-induced phase errors can be effectively eliminated by careful selection of the receiver bandwidth and echo time (TE), leading to more accurate PC-MRI measures of blood flow.

INTRODUCTION

PC-MRI is subject to numerous sources of error, which decrease clinical confidence in the reported measures. These sources of error include eddy currents (29), Maxwell terms (24), gradient field distortions (23), off-resonance (34), variations in intra-thoracic pressure that arise during breath holding (35,36), non-optimized parameter selection, and chemical shift effects. There exist established correction methods for many of these errors (23,24,29), but chemical shift effects and the concomitant methods to reduce these errors in PC-MRI have not been thoroughly described. Gatehouse et al. described a 5% error in a stroke volume to be a limit of acceptability in PC-MRI flow measurements (25). Herein we adopt this criterion and state that sources of error must contribute <5% flow measurement error to be clinically insignificant.

Herein we outline the theoretical basis of chemical shift in PC-MRI, and then use computational simulations, in vitro, and in vivo experiments to illustrate how perivascular fat can chemically shift across the vessel wall into the lumen and impart a significant phase measurement error. Importantly, we will show that the chemical shift effects in PC-MRI do not subtract in phase difference processing, but these errors can be reduced to clinically insignificant levels with a judicious choice of bandwidth (BW) and TE. As we will demonstrate, the effects of chemical shift on quantitative PC-MRI measurements are complex as they depend on the field strength, receiver BW, echo time, and the presence or absence of perivascular fat. This has important implications for quantitative, longitudinal, multicenter trials, which require both quantitative imaging clinical endpoints and high methodological reproducibility.

To test the theory, we hypothesized that chemical shift induced phase errors in PC-MRI introduce significant flow measurement errors in vivo. Therefore, the objectives of this study were to: (1) analytically define and quantify the contribution of chemically shifted perivascular fat to quantitative PC-MRI flow measurement errors; and (2) define the BW and TE that reduces errors in PC-MRI net forward flow measurements in the ascending aorta (aAo), main pulmonary artery (PA), and sum of the right and left pulmonary arteries (RPA + LPA) to clinically insignificant levels.

THEORY

In PC-MRI, velocity encoded images can be formed from an interleaved set of acquisitions using both flow compensated and flow encoded gradients (22). The complex MRI signals (Z) depend on the signal magnitude (M) from stationary fat (M_{Fat}) and flowing blood (M_{Blood}), the signal phase (ø) from stationary fat ($ø_{Fat}$) and flowing blood of velocity, v, ($ø_V$), as well as off-resonance ($ø_{Off}$):

$$Z_C = \left[M_{Blood} + M_{Fat}e^{i(\phi_{Fat})}\right] e^{i\phi_{Off}} \qquad [1a]$$

$$Z_E = \left[M_{Blood}e^{i(\phi_v)} + M_{Fat}e^{i(\phi_{Fat})}\right] e^{i\phi_{Off}} \qquad [1b]$$

Eq. [1] does not include the effects of eddy currents, Maxwell terms, or other phase errors. From a pair of complex flow images, Z_C (flow compensated) and Z_E (flow encoded), the measured phase difference (θ) is given by Eq. [2] (14,15,37,38).

$$\theta = arg(Z_C) - arg(Z_E) = arg\left(\frac{Z_C}{Z_E}\right) = arg(Z_C Z_E^*) \qquad [2]$$

Where * denotes the complex conjugate and *arg* yields the angle (i.e. phase) between the two complex vectors (i.e. *arg*(x+iy) = atan(y/x)):

$$\begin{aligned}\theta &= arg\left[\left(M_{Blood} + M_{Fat}e^{i(\phi_{Fat})}\right) e^{i\phi_{Off}} \left(M_{Blood}e^{-i(\phi_v)} + M_{Fat}e^{-i(\phi_{Fat})}\right) e^{-i(\phi_{Off})}\right] \\ &= arg\left[M_{Blood}^2 e^{-i(\phi_v)} + M_{Blood}M_{Fat}e^{-i(\phi_{Fat})} + M_{Blood}M_{Fat}e^{-i(\phi_v - \phi_{Fat})} + M_{Fat}^2\right] \qquad [3]\end{aligned}$$

Eq. [3] and Fig. 22 demonstrate that although off-resonance effects due to intravoxel magnetic field inhomogeneity cancel out during phase difference processing, the effects of chemically shifted perivascular fat do not. As a result, stationary perivascular fat contributes to the measurement of θ whenever M_{Fat} or $ø_{Fat}$ is non-zero. Perivascular fat surrounds most vessels and can chemically shift across the vessel wall into the lumen, thereby superposing the off-resonant phase and magnitude of fat onto a pixel containing flowing blood. Depending on the vessel wall thickness, perivascular fat can chemically shift into the vessel lumen and corrupt the complex MRI signal near the vessel wall then adds to the complex blood signal, which can lead to a clinically significant over- or underestimation of blood velocity within a vessel depending on the magnitude and phase of the fat signal relative to the phase of blood.

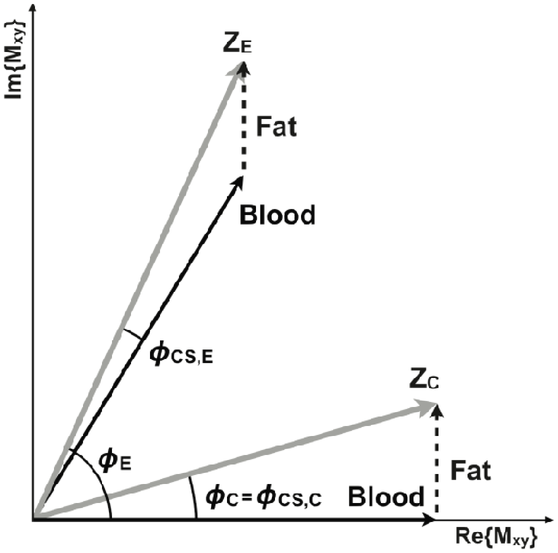

Figure 22. Components of the transverse magnetization from a flow compensated (Z_C) and flow encoded (Z_E) experiment. In the absence of field inhomogeneity, eddy currents, Maxwell terms, and other phase errors, the blood (i.e. water) signal is encoded with a phase that depends upon the first moment of the velocity encoding gradient and the blood velocity (black arrows). The off-resonant effects of chemically shifted fat (dashed arrow) sum with the complex blood signal to form the Z_C and Z_E measured signals (gray arrows). Note that the contribution of fat does not cancel with the phase difference method ($\o_C$ - $\o_E$) because the two required experiments are differentially affected by chemical shift ($\o_{CS,C} \neq \o_{CS,E}$).

The magnitude of the chemically shifted fat signal depends upon the steady-state signal magnitude of M_{Fat} relative to M_{Blood}, the vessel wall thickness, and the percent of chemically shifted fat within a measurement pixel. The percent of chemically shifted fat represents the amount of fat that is spatially shifted into the vessel and is controlled by BW and spatial resolution (Fig. 23) according to the following: pixel shift = $\delta f \cdot BW^{-1} \cdot \Delta x$, where δf is the off-resonance frequency shift between water and fat (δf_{3T} ~420 Hz; scanner reported B_0 = 2.89T) and Δx is the spatial resolution in the readout direction. Chemically shifted perivascular fat shifts further into the vessel at low BW (LBW) compared to high BW (HBW) (39). The spatial shift of fat, and thus the percent of chemically shifted fat within a pixel, is greater at lower bandwidths compared to higher bandwidths. The effects of BW on the accuracy of PC-MRI measurements are summarized in Fig. 24a.

The phase of fat is determined by δf and the TE:

$$\phi_{Fat} = 2\pi \delta f TE \tag{4}$$

A careful distinction is to be made between $ø_{Fat}$ and $ø_{CS}$: $ø_{Fat}$ is the phase of fat, as determined by Eq. [4], whereas $ø_{CS}$ is the chemical shift phase error arising for a given experiment (i.e. $ø_{CS,E}$ is the chemical shift induced phase error for the flow encoded measurement in Fig. 22).

A TE that orients fat to be in-phase with stationary water (i.e. blood) is referred to as an in-phase TE (TE_{IN}) and, similarly, a TE that orients fat to be out-of-phase with stationary water is referred to as an out-of-phase TE (TE_{OUT}). From Eq. [4] it can be shown that at 3T, TE_{IN} occurs at 2n•1.23 ms and TE_{OUT} occurs at (2m-1)•1.23 ms, where n=[0,1,2,…] and m=[1,2,3,…]. Similarly, echo times that orient the fat signal perpendicular to the stationary water signal include $TE_{+\pi/2}$, which occurs at (2n+0.5)•1.23 ms, and $TE_{-\pi/2}$, which occurs at (2m-0.5)•1.23 ms.

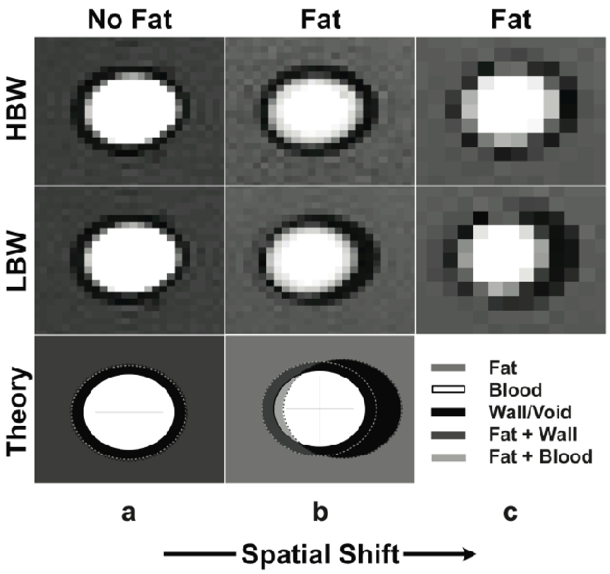

Figure 23. The experimentally measured spatial shift of chemically shifted perivascular fat in a phantom setup depends on the choice of high or low bandwidth (HBW or LBW) and spatial resolution (top two rows). Fat chemically shifts more to the right at LBW (middle row) compared to HBW (top row) and also at lower spatial resolutions (column c). Column a: Images with no "perivascular" fat ("vessel" surrounded by water). Column b: with "perivascular" fat ("vessel" surrounded by oil) at a standard spatial resolution. Column c: with "perivascular" fat at lower spatial resolution. The bottom row is a theoretical representation of the distribution of signal as a consequence of both chemical shift effects and partial voluming at LBW. The black region arises due to fat chemically shifting out of that region (signal void), the green region arises as a result of fat chemically shifting into the vessel wall (signal overlap of wall and fat signal), and the orange region arises due to fat chemically shifting through the vessel wall and into the vessel lumen (signal overlap of blood and fat signal), which leads to chemical shift induced phase errors.

Blood near the vessel wall is typically slow flowing (especially under laminar flow conditions) and therefore has a near zero phase. The effects of TE on the phase difference measurements are summarized in Fig. 24b. The use of $TE_{-\pi/2}$ causes the phase component of a stationary fat vector to be oriented approximately perpendicular in the negative direction to the slow flowing blood vector, which leads to a decrease in the measured θ. The use of TE_{IN} causes the phase component of a stationary fat vector to be oriented in approximately the same direction as the slow flowing blood vector, which leads to a decrease in the measured θ. The use of TE_{OUT} causes the phase component of the fat vector to be oriented in approximately the opposite direction of the slow flowing blood vector, which leads to an increase in the measured θ. The use of $TE_{+\pi/2}$ causes the phase component of the fat vector to be oriented approximately perpendicular to the blood vector, in the positive direction, which leads to an increase in the measured θ.

In summary, Eq. [3] demonstrates that chemical shift differentially affects the flow compensated and flow encoded experiments and, unlike off-resonance effects, does not cancel out during phase difference processing. The chemical shift induced phase error is greater at LBW compared to HBW and also at $TE_{\pm\pi/2}$ compared to TE_{IN} or TE_{OUT}. Collectively, the magnitude of the chemical shift error at different BWs and TEs can be summarized by Eq. [5], where *Truth* is defined as the net forward flow measured in the absence of chemical shift induced phase errors:

$$\begin{aligned} &LBW_{TE_{-\pi/2}} < HBW_{TE_{-\pi/2}} < LBW_{TE_{IN}} < HBW_{TE_{IN}} \\ &< Truth < HBW_{TE_{OUT}} < LBW_{TE_{OUT}} < HBW_{TE_{+\pi/2}} < LBW_{TE_{+\pi/2}} \end{aligned} \qquad [5]$$

Eq. [5] and Fig. [24] show that HBW always reduces errors from fat more than LBW. For a given BW, TE_{IN} leads to reduced errors from fat compared to TE_{OUT} because TE_{IN} places fat more in-phase with slow flowing blood ($ø_v \approx 0$) near the vessel wall (Fig. 24b).

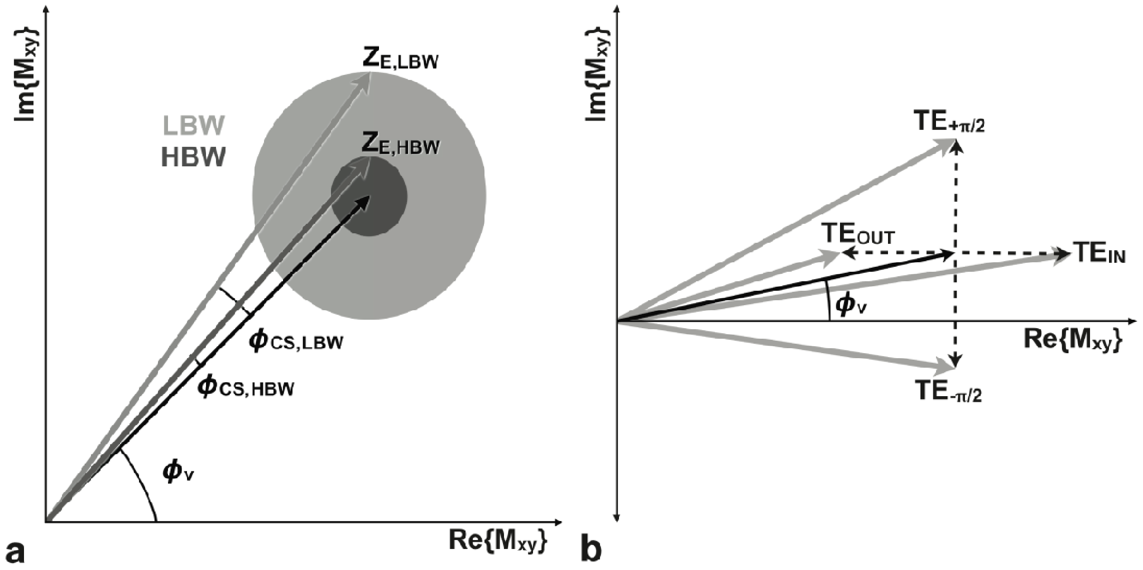

Figure 24. The effects of chemical shift phase ($\square_{CS}$) on quantitative PC-MRI measurements. (a) In the absence of chemical shift and other phase errors, flowing spins are encoded with an amount of phase proportional to their velocity ($\square_{v}$, black arrow). When chemical shift effects are taken into consideration the choice of high or low bandwidth (HBW or LBW) scales the magnitude (radius of the gray circles in (a)) of the complex fat factor because it controls the percent of partial-volume fat. HBW results in a lower percent of partial-volume fat (reduced magnitude) than LBW, which for a fixed TE results in $\square_{CS,HBW} < \square_{CS,LBW}$. In (b) it is apparent that the TE determines the phase of the complex fat factor (dashed arrow), which adds to the blood velocity vector (black arrow) to produce the Z_C or Z_E complex signal (gray arrow) and subsequently impacts the magnitude of the phase error. TE_{IN} leads the fat vector to be closely aligned with the blood vector when the blood velocity is low, which is typical of the vessel lumen periphery where CS effects are likely to be problematic. The use of TE_{IN} leads to reduced errors from chemical shift ($\square_{CS,TE\text{-}\pi/2} < \square_{CS,TE\ IN} < \square_{v,\ Blood} < \square_{CS,TE\ OUT} <$

$\square_{\mathrm{CS,TE}+\pi/2}$).

METHODS

Computational Simulations

A theoretical understanding of chemically shifted perivascular fat in PC-MRI was achieved, in part, through the use of computational simulations. Constant laminar blood flow (v=50 cm/s) and tri-phasic laminar blood flow (v_{Peak} = 50 cm/s; the first 50% of the waveform ranged from 0 to v_{Peak}, the next 25% ranged from 0 to -0.05•v_{Peak} and then back to 0, and the last 25% ranged from 0 to 0.05•v_{Peak} and then back to 0) was modeled using a “vessel” geometry (15.9/1.6 mm inner diameter/wall thickness) that emulated the right or left branch pulmonary artery. The simulations used the following imaging parameters: 8.5/9.1 ms TR (3T/1.5T), 2.80/3.08/3.38/3.69/4.01/4.30/4.60/4.92 ms TEs at 3T and 5.36/5.95/6.55/7.15/2.98/3.57/4.17/4.76 ms TEs at 1.5T ($TE_{+\pi/4}/TE_{+\pi/2}/TE_{+3\pi/4}/TE_{OUT}/TE_{-3\pi/4}/TE_{-\pi/2}/TE_{-\pi/4}/TE_{IN}$), 1.7 mm × 1.7 mm × 6 mm acquisition voxel, 30° flip angle, BWs of 100, 200, 300, 401 (LBW), 500, 600, 700, 814 (HBW), 900, and 1000 Hz/pixel, and VENC = 50 cm/s. The simulated TEs were chosen based on the achievable TEs within our current pulse sequence. The simulated TRs were chosen as the minimum available TR for the longest TE and lowest BW at each field strength.

The signal magnitude of flowing blood, the vessel wall, and fat for a spoiled gradient echo sequence was determined analytically from the work proposed by Gao et al. (40), which was altered to account for in-flow effects:

$$M_{xy}(x,y) = \begin{cases} M_0 \frac{1-e^{-\frac{TR}{T_1}}}{1-\cos\alpha e^{-\frac{TR}{T_1}}} \sin\alpha e^{-\frac{TE}{T_2}} \cdot d\Delta x \Delta y, & v(x,y) = 0 \qquad [6a] \\ \sum_{n=1}^{m} M_{xy}^{n}(x,y) \cdot \dfrac{d}{m} \cdot \Delta x \cdot \Delta y, & 0 < v(x,y) < \frac{d}{TR} \qquad [6b] \\ M_0 \sin\alpha e^{-\frac{TE}{T_2}} \cdot d\Delta x \Delta y, & v(x,y) \geq \frac{d}{TR} \qquad [6c] \end{cases}$$

Where, M_0 is the equilibrium magnetization, *TE* and *TR* are the gradient echo time and repetition time respectively, α is the imaging flip angle, d is the slice thickness, Δx and Δy are the pixel resolutions in the x and y dimensions, v is the tissue velocity, and m, which represents the number of RF excitations a spin experiences, is determined by,

$$m = int\left(\frac{d}{v \cdot TR}\right) \qquad [7]$$

where *int* indicates the integer value corresponding to the round off quotient. M_{xy}^{n} in Eq. [6b] is determined by the following equation:

$$M_{xy}^{n}(x, y, TE) = M_z^0 \left[\left(1 - e^{\frac{-TR}{T_1}}\right)\left(\frac{1 - \cos^{n-1}\alpha e^{\frac{-(n-1)TR}{T_1}}}{1 - \cos\alpha e^{\frac{-TR}{T_1}}}\right) + \cos^{m-1}\alpha e^{\frac{-(n-1)TR}{T_1}}\right] \sin\alpha e^{\frac{-TE}{T_2}} \qquad [8]$$

Values of the T_1, T_2, and proton density (PD) at 3T (1.5T) for each tissue type were obtained from literature results: T_1=1700 ms (T_1=1400 ms), T_2=275 ms, PD=0.90 (blood); T_1=500 ms (T_1=350 ms), T_2=100 ms, PD=0.98 (fat); and T_1=1400 ms (T_1=1000 ms), T_2=30 ms, PD=1.0 (vessel wall) (41,42). The oil spectrum was measured with spectroscopy at 3T and the frequency shift was found to be 1.4ppm. The chemical shift of the mixture of glycerol and water ("blood") was estimated to be 4.35ppm, based on proton weighted peak averaging and literature values of glycerol (43). Our computer simulations assume two single resonances, one for "blood" (water and glycerol) and one for fat (vegetable oil) with a frequency difference of 2.96ppm. Our simulations were conducted with B_0 = 2.89T for 3T B_0 = 1.49T for 1.5T based on the scanner reported field strengths.

Eq. [6] describes three flow regimes. Static spins (v = 0, Eq. [6a]) are subject to multiple RF pulses, resulting in the development of a steady state signal. For spins moving at a velocity such that they do not fully escape the slice during the TR ($v < d/TR$, Eq. [6b]), a portion of the spins occupying the selective slice are replenished each TR by fresh inflowing spins with an equilibrium level of magnetization. Lastly, if the spins have a velocity such that they escape the imaging slice during the TR ($v \geq d/TR$, Eq. [6c]), then they only experience a single RF pulse and exhibit a maximum signal.

The simulations were conducted with perivascular fat at LBW (high partial volume of fat pixels) and HBW (lower partial volume of fat pixels) as well as with stationary water in place of perivascular fat to yield the true flow result in the absence of chemical shift effects. The simulations were conducted under the assumption of a perfect slice profile. The simulated field of view was 25 × 25 mm with a spatial resolution of 1.7 mm × 1.7 mm. The simulation was conducted under super-resolution conditions to better model partial volume effects. To do this, the image was simulated at 100x the imaging resolution yielding a 1500 × 1500 complex array for blood, fat, and the vessel wall. The signal magnitudes were computed using Eq. [6]. The phase of the blood signal was assigned for each matrix element based on the simulated constant laminar or tri-phasic laminar velocity profiles at each spatial position. The off-resonance phase of fat at 1.5 T and 3T was derived using $\delta f_{1.5T}$ and δf_{3T}, the simulated TEs, and Eq. [4]. The vessel wall was assumed to be static and on-resonance with blood, thus its phase matrix consisted entirely of zeros.

For the simulations with perivascular fat, the fat array was spatially shifted by 45 (1.5T) and 91 (3T) pixels in the super-resolution domain (equivalent to 0.45 and 0.91 pixels in the imaging domain, respectively) for LBW (401 Hz/pixel) and by 22 (1.5T) and 45 (3T) pixels in the super-resolution domain (0.22 and 0.45 pixels in the imaging domain, respectively) for HBW (814 Hz/pixel) to simulate the chemical shift effect (pixel shift = $\delta f \bullet BW^{-1} \bullet 100$ spins/pixel). The complex signal from the three simulated tissues was obtained from:

$$Z_{Blood}(x,y) = M_{xy}^{Blood}(x,y)e^{i\left(\frac{v_{Blood}(x,y)}{VENC}\pi\right)} \quad [9a]$$

$$Z_{Fat}(x,y) = M_{xy}^{Fat}(x,y)e^{i(2\pi\Delta fTE)} \quad [9b]$$

$$Z_{Wall}(x,y) = M_{xy}^{Wall}(x,y) \quad [9c]$$

The complex signals for all three tissues within 100 × 100 pixels in the super-resolution domain were added together to constitute one imaging pixel

The net forward flow of blood in the simulated vessel was computed by calculating the velocity of every pixel within the simulated vessel by scaling the phase result by VENC/π (cm/s). The resulting pixel velocities were then multiplied by the spatial resolution (pixel area, cm^2) to calculate the flow rate (mL/s) and finally integrated over the cardiac cycle to yield the net forward flow results (mL).

In Vitro Phantom Experiments

The theoretical effects of chemical shift induced PC-MRI errors were compared to those obtained in flow phantom experiments. All imaging was performed on a Siemens Trio 3 Tesla system (Siemens Medical Solutions, Erlangen, Germany) with 40 mT/m maximum gradient amplitude and 200 T/m/s maximum slew rate. PC-MRI data was acquired in a sealed tube (19.1/1.6 mm diameter/wall thickness) surrounded first by water and then by vegetable oil to simulate perivascular fat. Blood-mimicking fluid (40% glycerol, 60% water) was circulated through the phantom by a CardioFlow 1000MR computer-controlled displacement pump (Shelley Medical Imaging Technologies, Toronto, Ontario, Canada) at a constant programmed flow rate of 25 mL/s. Measurements were performed using a 12-element head coil. The flow rate and tubing were selected to approximate the velocity and vessel dimensions of the branch pulmonary arteries.

The PC-MRI protocol used a cine gradient echo phase-contrast sequence with the following sequence parameters: 8.5 ms TR, 4.92/6.15/5.54/6.77 ms TEs (minimum achievable $TE_{IN}/TE_{OUT}/TE_{+\pi/2}/TE_{-\pi/2}$), 192 × 120 encoding matrix, 1.7 mm × 1.7 mm × 6 mm acquisition voxel, 30° flip angle, BWs of 401 Hz/pixel (LBW) and 814 Hz/pixel (HBW) Hz/pixel, 4 views-per-segment, a temporal resolution of 68ms, 20 phases reconstructed from a 20 second acquisition using retrospective ECG gating, and GRAPPA (44) parallel imaging with an acceleration factor of 2 and 24 central *k*-space reference lines. An artificial ECG signal was generated using a physiologic signal simulation tool available as part of the scanner's software environment. The R-R interval was adjusted to 1000 ms (60 beats per minute). Through-plane velocity encoding was performed using interleaved flow-compensated and flow-sensitive encoding with a VENC of 70 cm/s.

In Vivo Imaging Experiments

Based upon the theoretical and experimental findings, *in vivo* experiments were performed to demonstrate the effects of chemical shift errors in PC-MRI in healthy volunteers (N=10). The university's Institutional Review Board (IRB) approved the study and informed consent was obtained for each subject prior to MRI scanning. After addressing each subject's concerns, each subject was positioned head first in the supine position on the scanner bed and imaged using a 6-element body matrix and 6-element spine matrix coils for signal reception. Blood flow was measured using PC-MRI in the aAo, PA, RPA, and LPA of ten (N=10) volunteers (3 female, 7 male; age 25.9±4.7 years) with no previous history of cardiovascular disease. High-resolution black blood turbo spin echo (TSE) images were also acquired with and without fat saturation (45,46) during end-systole in order to define the presence (or absence) of perivascular fat for the vessel of interest in the same slices used for PC-MRI flow measurement.

The imaging plane for aAo flow was located in the ascending aorta distal to the aortic valve and coronary ostia. The imaging plane for flow in the PA was located downstream from the pulmonary valve and proximal to the bifurcation. The imaging planes for the LPA and RPA were located ~1 cm distal to the pulmonary bifurcation. All imaging planes were prescribed on the cine images during end-systole with end-expiratory breath holds.

PC-MRI flow measurements were obtained using the same sequence parameters as in the *in vitro* phantom experiments with the following changes: 8.5 ms TR, 4.92/5.54 ms $TE_{IN}/TE_{+\pi/2}$, 340 × 233 FOV, 256 × 160 matrix, 1.3 mm × 1.3 mm × 6 mm acquisition voxel, BWs of 399 Hz/pixel (LBW) and 814 Hz/pixel (HBW), and a VENC of 125 cm/s for all flow territories.

Note that the minimum available TR at LBW was used during HBW scans in order to ensure the resulting differences in the PC-MRI measurements were only due to the change in BW, and not due to changes in TR.

Image Processing

Data were processed offline using MATLAB (The MathWorks, Natick, MA) and a DICOM viewing tool (Osirix, www.osirix-viewer.com). Eddy current correction was conducted through the use of a stationary phantom (25,29,30,47) for *in vivo* studies after the subject was removed from the scanner and, in the case of the *in vitro* phantom studies, with the flow turned off. For quantitative flow assessment, a region-of-interest (ROI) was drawn in Osirix for each vessel territory. This same ROI was copied into the stationary eddy current phantom images and background phase errors were subtracted in MATLAB. The net forward flow was calculated as described in the Methods section for the computational simulations.

Statistical Analysis

Chemical Shift Effects on Net Forward Flow – An analysis of the maximum difference (Δ_{Max}) in the measured net forward flow for measurements obtained in the aAo, PA, RPA, and LPA at LBW-TE_{IN}, HBW-TE_{IN}, HBW-$TE_{+\pi/2}$, and LBW-$TE_{+\pi/2}$ for ten patients was conducted. Pulmonary to systemic blood flow ratios (Qp/Qs, PA flow divided by aAo flow) were calculated for each individual. A two-sample t-test with Holm-Sidak post hoc correction was used to measure the statistical significance of the differences in Δ_{Max} between vessels with and without perivascular fat and Qp/Qs at HBW-TE_{IN} vs. LBW-$TE_{+\pi/2}$. Additionally, the mean Δ_{Max} was calculated for each patient's flow territory in mL and also as a percentage (percent mean Δ_{Max}).

Relative Blood Flow Comparison – For the *in vivo* experiments, according to Eq. [5] and Fig. 24, we expect the net forward flow measurements to be ordered as follows:

$$LBW_{TE_{IN}} < HBW_{TE_{IN}} < Truth < HBW_{TE_{+\pi/2}} < LBW_{TE_{+\pi/2}} \qquad [10]$$

Blood Flow Comparison Between Flow Territories – Bland-Altman (48) plots were constructed to show that the reduction of chemical shift induced flow errors improved the intra-patient agreement of flow in the various territories as evidenced by a decrease in the measurement bias (mean difference between the two measurements) and limits of agreement (95% confidence intervals, 95%-CI) between the net forward flow in the aAo and PA, aAo and RPA+LPA, and PA and RPA+LPA at HBW-TE_{IN} and LBW-$TE_{+\pi/2}$. In addition, the measurement bias was evaluated using a paired t-test with Holm-Sidak post hoc correction.

RESULTS

Computational Simulations versus In Vitro Phantom Studies

Figure 25A demonstrates that constant laminar flow computational simulations and *in vitro* phantom studies show nearly identical chemical shift effects over a range of BWs and TEs. Net flow results follow the expected trends of Eq. [5], with HBW-TE_{IN} being closest to programmed volume flow rate (“*Truth”*=48mL*)* and LBW-$TE_{+\pi/2}$ being furthest from “*Truth*.” The 3T tri-phasic laminar flow computational simulations (Fig. 25C) overestimate the net forward flow compared to “*Truth*” at LBW-$TE_{+\pi/2}$ (54mL vs. 48 mL, 12%) compared to HBW-TE_{IN} (47.9 mL vs. 48 mL, 0.2%)**,** whereas the 1.5T tri-phasic laminar flow computational simulations (Fig. 25E) overestimate the net forward flow LBW-$TE_{+\pi/2}$ (50mL vs. 48 mL, 4%) compared to HBW-TE_{IN} (47.9 mL vs. 48 mL, 0.2%).

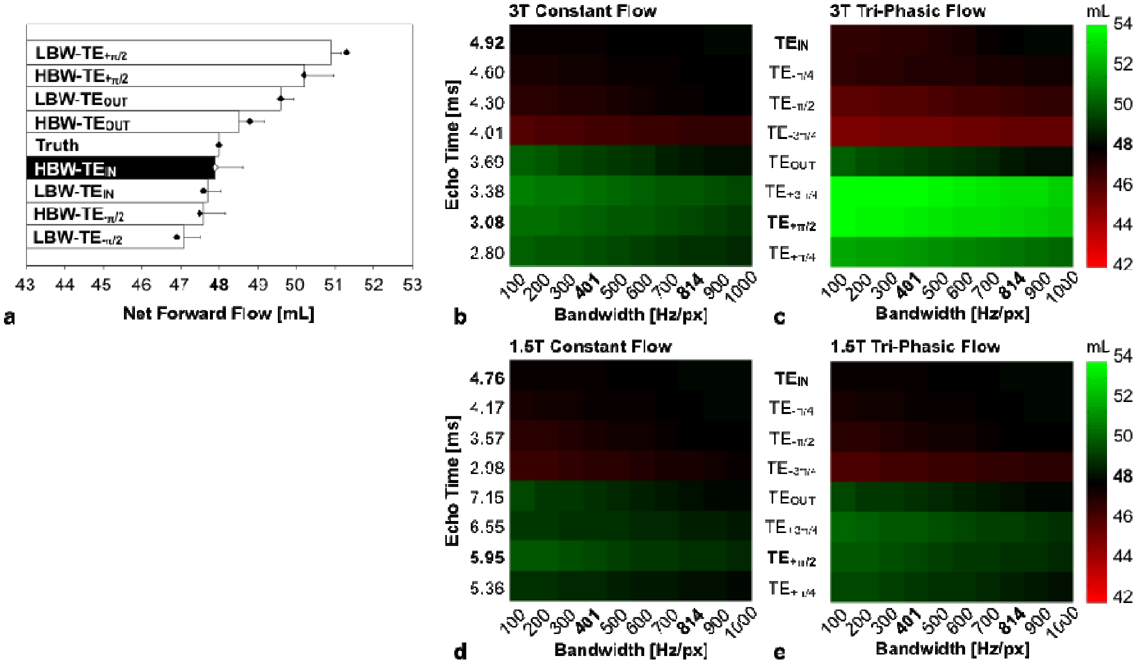

Figure 25. Impact of receiver bandwidth (BW) and echo time (TE) on PC-MRI flow measurements. (A) Constant laminar flow computer simulations (dots) and *in vitro* (bars) 3T results show nearly identical chemical shift effects (“*Truth*”=48mL). Computer simulations of constant laminar flow (B,D) and tri-phasic flow (C,E) at 3T and 1.5T demonstrate that the use of HBW-TE_{IN} is closest to the known flow of 48mL and has the least chemical shift induced PC-MRI errors. Other BW and TE combinations at 3T (1.5T) can lead to as much as a 12% (3%) underestimate (LBW-$TE_{-\pi/2}$) or a 12% (4%) overestimate (LBW-$TE_{+\pi/2}$) for tri-phasic flow.

In Vivo Studies

Chemical Shift Effects on Net Forward Flow – Not every volunteer had visible perivascular fat surrounding every measured vessel (Fig. 26). To qualitatively illustrate the effects of chemical shift the net forward flow data from the aAo, PA, RPA, and LPA at LBW-TE_{IN}, HBW-TE_{IN}, HBW-$TE_{+\pi/2}$, and LBW-$TE_{+\pi/2}$ for all ten patients were arranged in a bar-chart to show that changing the BW and TE can systematically lead to changes in measured flow. The results for each vessel are arranged in order of their theoretically expected trend (Fig. 27). For vessels in which minimal perivascular fat was observed in the TSE images (annotated with an * below each dataset) the bar-charts appear much flatter (low Δ_{Max}) than vessels wherein perivascular fat was detected. In the presence of perivascular fat the bar-charts step upward from LBW-TE_{IN} (smaller Δ_{Max}) to LBW-$TE_{+\pi/2}$ (larger Δ_{Max}) as expected in Eq. [5].

The Δ_{Max} in aAo, PA, LPA, and all vessels with fat is significantly greater than Δ_{Max} in those vessels with minimal perivascular fat (Table 1). The analysis could not be conducted in the RPA because every vessel had visible perivascular fat.

The mean Δ_{Max} and percent mean Δ_{Max} for the aAo, PA, RPA, and LPA is summarized in Table 2. The mean Δ_{Max} was greatest in the PA (8.9±6.7 mL) and smallest in the LPA (3.1±1.8 mL). The percent mean Δ_{Max} was greatest in the RPA (13.8±7.9%) where every vessel had observed perivascular fat and the vessel wall was thinnest. The percent mean Δ_{Max} was smallest in the aAo (5.3±3.7%) where perivascular fat was not observed in 4 of the 10 vessels and had the thickest vessel walls.

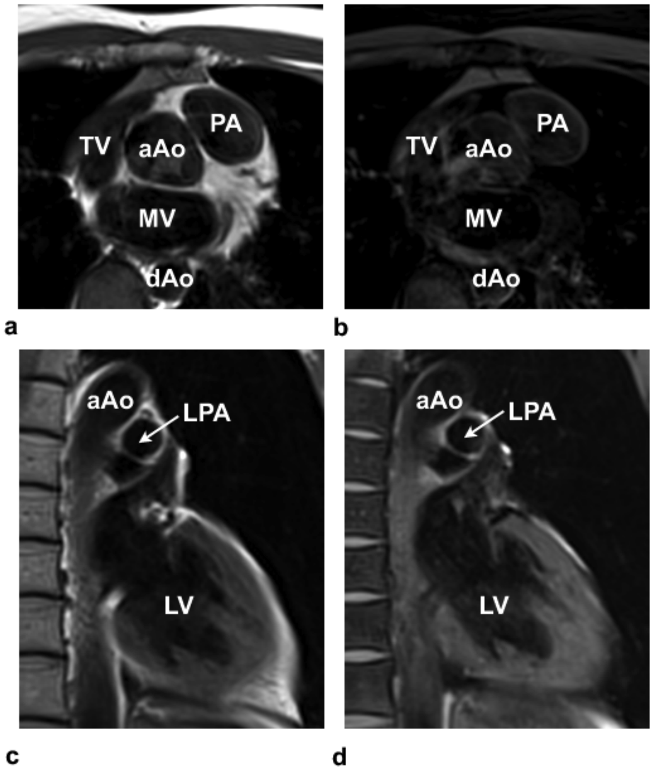

Figure 26. Turbo spin-echo (TSE) (a,c) and TSE with Fat-Sat images (b,d) highlight the presence of perivascular fat, especially around the PA in (a) and (b) and the lack of perivascular fat around the LPA in (c) and (d). TV-Tricuspid valve; MV-mitral valve; aAo-ascending aorta; and dAo-descending aorta; PA-pulmonary artery; LPA-left pulmonary artery; LV-left ventricle.

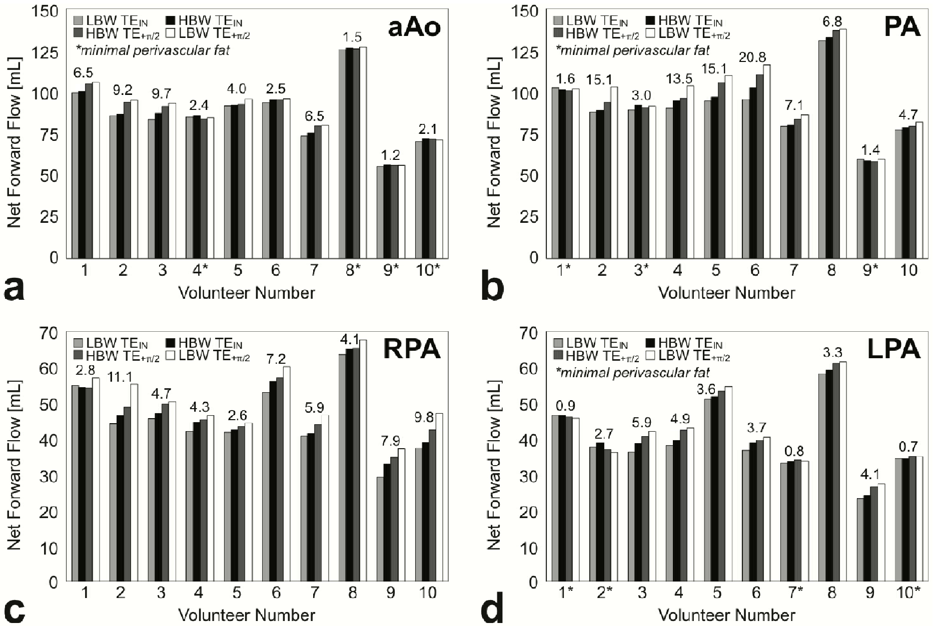

Figure 27. Net forward flow (mL) data at LBW-TE$_{IN}$, HBW-TE$_{IN}$, HBW-TE$_{+\pi/2}$, and LBW-TE$_{+\pi/2}$ in normal subjects (N=10). The maximum difference (Δ_{Max}) in the measured net forward flow is presented above each dataset. An asterisk ('*') is used to indicate that minimal perivascular fat was observed in the TSE images. In general, the trends follow the expectation in Eq. [5]. a) The mean Δ_{Max} in the aAo are small compared to other vascular territories due to the small amounts of observed perivascular fat and a thicker vessel wall. b) The chemical shift induced flow measurement errors in the PA can be large due to the presence of perivascular fat and a relatively thin vessel wall. c) Note that no subject had an RPA that had minimal perivascular fat, whereas this was common in the aAo, PA, and LPA. Additionally, the thin wall of the RPA makes it easy for perivascular fat to spatially shift into the vessel lumen. Therefore, all subjects' RPAs were susceptible to chemical shift induced flow errors. d) Perivascular fat was not as consistently observed in the LPA compared to the RPA.

Table 1: Comparison of the maximum difference between LBW-TE_{IN}, HBW-TE_{IN}, HBW-$TE_{+\pi/2}$, and LBW-$TE_{+\pi/2}$ forward flow measurements in the aAo, PA, RPA, and LPA in normal subjects.

	Δ_{Max} No Fat [mL]	**Δ_{Max} Fat [mL]**	**n / m**	***P-Value**
aAo	1.8 ± 0.5	6.4 ± 2.8	4 / 6	0.01
PA	2.0 ± 0.9	11.9 ± 5.8	3 / 7	0.04
RPA	--	6.0 ± 2.9	0 / 10	--
LPA	1.3 ± 1.0	4.3 ± 1.0	4 / 6	0.003
All Vessels	1.7 ± 0.8	7.2 ± 4.4	10 / 30	0.001

Data is expressed as mean ± standard deviation in mL.

n is the number of vessels where minimal perivascular fat was observed.

m is the number of vessels where perivascular fat was observed.

*P-values<0.05 show a significant difference in Δ_{Max} indicating the presence of perivascular fat leads to significant flow errors in PC-MRI.

Table 2: Comparison of the mean maximum difference between LBW-TE_{IN}, HBW-TE_{IN}, HBW-$TE_{+\pi/2}$, and LBW-$TE_{+\pi/2}$ forward flow measurements in the aAo, PA, RPA, and LPA in normal subjects (N=10).

	Mean Δ_{Max} [mL]	**Percent Mean Δ_{Max}**
aAo	4.6 ± 3.2	5.3 ± 3.7
PA	8.9 ± 6.7	9.4 ± 6.8
RPA	6.0 ± 2.9	13.8 ± 7.9
LPA	3.1 ± 1.8	8.0 ± 5.5

Data is expressed as mean ± standard deviation in mL.

Relative Blood Flow Comparison – The measured phase at LBW-TE_{IN}, HBW-TE_{IN}, HBW-$TE_{+\pi/2}$, and LBW-$TE_{+\pi/2}$ follow the expected trends of Eq. [10] for all of the volunteers. Note that when there is not an apparent trend this is always associated with a lack of observable perivascular fat in the black blood TSE images, hence the trend is still as expected. The Qp/Qs ratios were closer to one with lower variance when measured with HBW-TE_{IN} and compared to LBW-$TE_{+\pi/2}$ (1.05±0.03 vs. 1.08±0.09, p=0.10), but not statistically different.

Blood Flow Comparison Between Flow Territories – The Bland-Altman plots and statistics (Fig. 27) show higher internal consistency (lower bias and smaller 95%-CIs) at HBW TE_{IN} compared to LBW $TE_{+\pi/2}$ across all flow territories.

The magnitude of the bias in net forward flow between the aAo and PA, aAo and RPA+LPA, and PA and RPA+LPA demonstrates a larger flow discrepancy in different subjects when using LBW-$TE_{+\pi/2}$ compared to HBW-TE_{IN} (Table 3). The PA vs. RPA+LPA comparison failed to reach a significant statistical difference due to the fact that seven of the thirty vessels in this comparison did not have notable perivascular fat.

The bias in net forward flow between the aAo and PA, aAo and RPA+LPA, and PA and RPA+LPA was shown to be significantly lower at HBW-TE_{IN} compared to LBW-$TE_{+\pi/2}$ (Table 3). The PA vs. RPA+LPA comparison failed to reach a significant statistical difference likely due to the fact that seven of the ten vessels in this comparison contained no notable perivascular fat. If these seven vessels were excluded from the statistical comparison, the comparison reaches statistical significance. The internal consistency between the net forward flow in the aAo and RPA+LPA was higher at both HBW-TE_{IN} (0.5 mL bias) and LBW-$TE_{+\pi/2}$ (-2.4 mL bias) compared to across any other vessel combination.

Table 3: Comparison of the bias (mean difference) between HBW-TE$_{IN}$ and LBW-TE$_{+\pi/2}$ forward flow measurements in the aAo vs. PA, aAo vs RPA+LPA, and PA vs. RPA+LPA in normal subjects (N=10).

	HBW-TE$_{IN}$	**LBW-TE$_{+\pi/2}$**	***P-Value**
aAo vs. PA	4.9 ± 2.4	9.8 ± 6.4	0.01
aAo vs. RPA+LPA	1.3 ± 0.8	4.0 ± 3.2	0.03
PA vs. RPA+LPA	5.4 ± 3.1	7.4 ± 5.9	0.25
[†]PA vs. RPA+LPA	2.0 ± 0.3	5.0 ± 2.9	0.03

Data is expressed as mean ± standard deviation in mL.

[†] Excludes seven vessels that contained minimal perivascular fat.

*P<0.05 show a significant difference in the measurement bias indicating HBW-TE$_{IN}$ is less susceptible to chemical shift flow errors compared to LBW-TE$_{+\pi/2}$.

DISCUSSION

Both theory and an *in vivo* comparison of the maximum difference in net forward flow between vessels with and without perivascular fat indicated that the effects of chemically shifted perivascular fat are minimized by the use HBW-TE_{IN}. In healthy volunteers (N=10) HBW-TE_{IN} significantly improves intrapatient net forward flow agreement as indicated by decreased measurement biases and limits of agreement across the ascending aorta, pulmonary artery, left pulmonary artery, and all vessels (Table 3 and Fig. 28).

In these experiments we suggest that the use of HBW-TE_{IN} mitigates chemical shift induced phase errors, but increasing the spatial resolution will also help, all other things being equal. Throughout the description of chemical shift effects on quantitative PC-MRI measurements we have assumed that fat has a single resonant peak, which belies the spectral complexity of fat. Additionally, this means that even at TE_{IN}, not all spectral components of fat are in phase with water.

It is important to note that perivascular fat is not always present; therefore not all PC-MRI flow measures are subject to errors from chemical shift effects. Additionally, the presence or absence of perivascular fat can lead to spurious agreement or disagreement in PC-MRI flow measures between territories. For example, the presence of perivascular fat could erroneously leads to a good or poor agreement in flow across the aAo, PA, and RPA+LPA. Although the internal consistency may be observed to be high, the flow in each territory could be over- or underestimated due to chemical shift errors.

The observed error arising from the chemical shift effect is greater in our *in vivo* studies and tri-phasic laminar computational simulations compared to our *in vitro* studies

(Fig. 25 and Table 1) due to differences in the velocity profiles. The chemical shift induced flow error is larger for dynamic flow when compared to constant laminar flow and the largest for $TE_{+\pi/2}$, when the total true forward flow is the same. This effect is evident in Fig. 25 and arises as a consequence of the fact that dynamic flow has more low-velocity pixels, which are the most affected by these chemical shift induced errors.

Fat-water separated PC-MRI should be considered to solve for both the phase of fat and the phase of water, thereby eliminating the contamination of the water phase by perivascular fat phase (49). The physics and mathematics of this problem are interesting, but the clinical utility of this approach is uncertain. This approach requires the acquisition of additional imaging data, which may prohibitively increases breath hold duration or significantly decrease spatial and/or temporal resolution.

In addition, fat saturation techniques could be combined with PC-MRI to minimize chemical shift induced phase errors. Fat saturation techniques, however, are spatially inhomogeneous and provide inconsistent fat saturation throughout the cardiac cycle and therefore may require multiple saturation pulses to be effective.

The results of this study focused entirely on Cartesian based trajectories. Non-Cartesian trajectories, such as radial and spiral, lead to distortion and blurring of the fat signal (49,50). This blurring effect may not be as resilient to the proposed chemical shift reduction strategy (HBW-TE_{IN}) and may necessitate the use of spatial-spectral pulses (51) or non-Cartesian based multipoint fat-water separation techniques (e.g. IDEAL (49) or Dixon (52))

Breathing artifacts and parallel imaging reconstruction artifacts, for example, can cause the signal from fat in regions distant from a vessel to alias into a vessel and corrupt the phase. Under these conditions the magnitude of the error is governed by the relative magnitudes and phases of the fat and blood signals and can lead to large errors in velocity and flow.

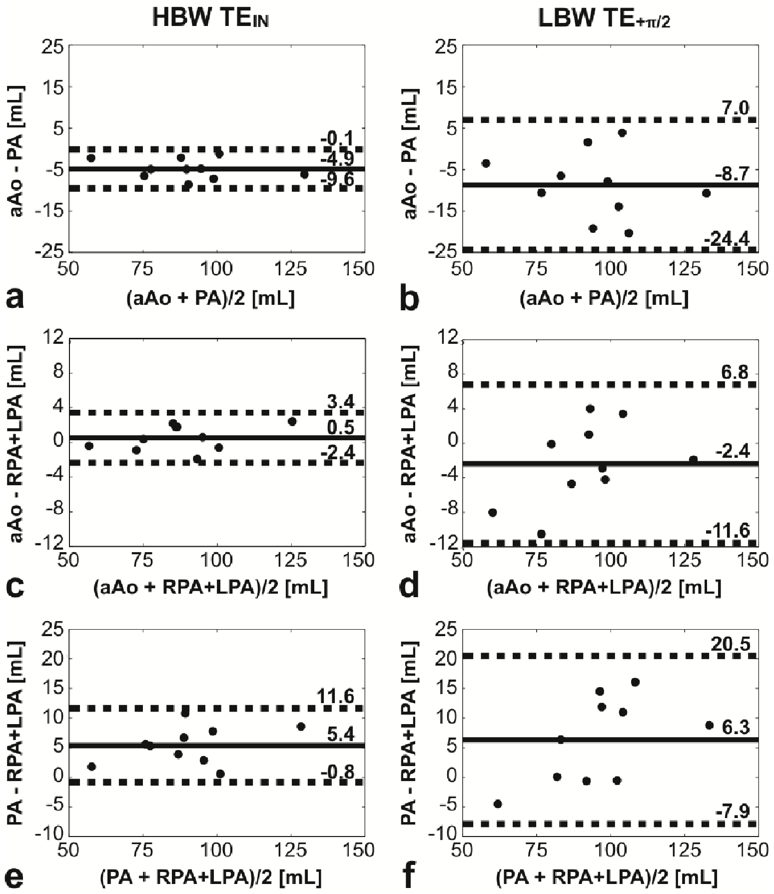

Figure 28. Bland-Altman analysis of the net forward flow in the ascending aorta (aAo), main pulmonary artery (PA), and right and left pulmonary branches (RPA and LPA) in normal subjects (N=10). The solid lines represent the measurement bias while the dashed lines represent the limits of agreement (95%-CIs). (a) Bland-Altman statistics for aAo versus PA at HBW-TE$_{IN}$; (b) aAo versus PA at LBW-TE$_{+\pi/2}$; (c) aAo versus RPA+LPA at HBW-TE$_{IN}$; (d) aAo versus RPA+LPA at LBW-TE$_{+\pi/2}$; (e) PA versus RPA+LPA at HBW-TE$_{IN}$; (f) PA versus RPA+LPA at LBW-TE$_{+\pi/2}$. The measurement bias and limits of agreement are reduced at HBW-TE$_{IN}$ (a, c, e) compared to LBW-TE$_{+\pi/2}$ (b, d, f) for all flow territories. The HBW-TE$_{IN}$ measurements are less susceptible to chemical shift induced errors and demonstrate better internal consistency.

Limitations – This study compared the results at TE_{IN} and $TE_{+\pi/2}$ as a means of characterizing and quantifying the effects of chemical shift. In clinical practice, it is common to use the minimum available TE, which may or may not be near the TEs chosen for this study. In our clinical setting, the minimum TE used at 1.5T and 3T are 2.67ms and 1.99ms, respectively. These TEs differ from TE_{IN} by 202° (approximately TE_{OUT}) and 291° (approximately $TE_{-\pi/2}$), implying that the use of these minimum clinical TEs can lead to a significant deviation in net forward flow, especially at 3T.

The use of HBW leads to a reduction in chemical shift induced phase errors, but also leads to an inherent reduction in both SNR and velocity-to-noise (53,54). Based on our theoretical description of chemical shift induced phase errors, future work is needed to define the imaging BW that provides optimal quantitative PC-MRI accuracy. Westenberg et al. reported previously that a 55% reduction in SNR (187±116 vs. 84±60) did not lead to flow inaccuracies in measurements across the mitral valve (55). Our SNR measurements indicate that both the LBW (103±6) and HBW (72±4) data are similar to Westenberg's acceptable and lower SNR measures. Therefore, the trends in our net forward flow results were largely chemical shift related and not SNR related. The use of HBW at 1.5T may lead to an SNR below these acceptable levels.

The *in vitro* and *in vivo* studies were conducted at 3T field strength. The spatial shift of chemically shifted perivascular fat at 1.5T is half of that at 3T because $\delta f_{1.5T} \approx \frac{1}{2}\delta f_{3T}$ (56), which leads to ~1/2 the spatial shift and half the off-resonance phase accumulation for fat at 1.5T. Therefore, the chemical shift induced phase error is lower at 1.5T when spatial resolution and SNR effects are not considered (Fig. 25d-e). The SNR performance of 1.5T, however, is ~1/2 that of 3T and to compensate for this, larger imaging voxels and/or lower bandwidths are typically employed; both of which increase chemical shift induced phase errors. Therefore, depending on the specific imaging parameters, quantitative PC-MRI measurements conducted at 1.5T are susceptible to similar chemical shift induced flow quantification errors.

All subjects included in this study were normal healthy volunteers. We propose that HBW and TE_{IN} parameters in PC-MRI minimize the phase corrupting effects of chemical shift, but this needs to be clinically validated in patients. In doing so, the assumption that flow at the vessel lumen periphery is near-zero, may not be true due to complex flow patterns, areas of turbulent flow, and partial volume effects. In future studies involving clinical patients with complex flow patterns, the optimum TE for the minimization of chemical shift effects may be different than TE_{IN}, because the flow won’t meet the requirement of being near-zero near the vessel wall. Under these circumstances fat-water separated or fat-saturation PC-MRI techniques may be necessary.

CHAPTER 5

VELOCITY ENCODING WITH THE SLICE SELECT REFOCUSING GRADIENT

The chemical shift reduction strategy described in Specific Aim #1 necessitates the use of a prohibitively long TE. In this chapter, a description and evaluation of a novel encoding method for time efficient chemical shift reduction (Specific Aim #2) is discussed. The velocity encoding method described herein uses the slice select gradient and a time-shifted refocusing gradient lobe for velocity encoding. We ***hypothesize*** that chemical shift-induced phase errors can be efficiently eliminated using slice select refocused gradient encoding, which shortens the TE/repetition time (TR) and increases temporal resolution.

INTRODUCTION

Our previous work (Chapter 4) has shown that chemically shifted perivascular fat can significantly corrupt PC-MRI flow measurements (57). In that work, we characterized the impact of chemical shifted lipid signals in PC-MRI and defined a coherent strategy to reduce chemical shift errors. Briefly, the amount of chemically shifted fat pixels that shift into the vessel can be reduced by increasing receiver bandwidth (BW) at the expense of signal-to-noise ratio (SNR). Secondly, an in-phase TE (TE_{IN}) will ensure fat and water resonances are in-phase, which minimizes the resulting errors in the calculated velocity.

Chemical shift errors are more challenging to address at 3T, as compared to 1.5T, due to the larger frequency difference between water and fat, which leads to a larger spatial shift of fat for a given bandwidth. Furthermore, the shorter minimum in-phase TE ($TE_{IN,MIN}$) at 3T (2.46 ms for δ_{3T} ~420 Hz and scanner reported B_0 = 2.89T) is shorter than at 1.5T (4.76 ms for $\delta_{1.5T}$ ~210 Hz and scanner reported $B_0 = 1.49$T), and may not be routinely achievable with standard flow encoding methods at conventionally targeted velocity encoding strengths (VENCs).

Herein we describe and evaluate a method for flow-encoding in PC-MRI that uses the slice select gradient and a time shifted refocusing gradient lobe to generate the target gradient moments, which shortens the TE/TR (increases temporal resolution) and enables the use of $TE_{IN,MIN}$ at 3T for time efficient reduction of chemical shift induced errors.

THEORY

For a typical PC-MRI experiment, two velocity-encoded acquisitions with different first moments are necessary to encode flow along a single direction (14-16). All encoding schemes are designed to null the zero gradient moment for both encoding steps, $M_{0,1} = M_{0,2} = 0$, to refocus the position-related phase, but with a net difference in first moments to yield velocity dependent phase with no dependence on non-velocity background phase,

$$\Delta\phi = \gamma v_z \left(M_{1,1} - M_{1,2}\right) = \gamma v_z \Delta M_1. \qquad [1]$$

In Eq. [1], Dϕ is the phase difference between the two velocity encoded images, γ is the gyromagnetic ratio, v_z is the velocity in the through-plane direction and $M_{1,1}$ and $M_{1,2}$ are the first gradient moments for encoding step 1 and 2. The velocity encoding strength, defined as the velocity that produces a phase shift of π radians, is determined by ΔM_1 for any encoding strategy:

$$VENC = \frac{\pi}{\gamma \, \Delta M_1|}. \qquad [2]$$

The target ΔM_1 is conventionally achieved by employing either bipolar velocity encoding gradients or a set of flow compensated and flow encoded (FCFE) velocity sensitizing gradients. For bipolar encoding, $M_{0,1} = M_{0,2} = 0$ and the equal and opposite gradient polarities yield $M_{1,1} = X/2$ and $M_{1,2} = -X/2$ (14,15). For FCFE encoding strategies, $M_{0,1} = M_{0,2} = 0$, while $M_{1,1} = 0$ and $M_{1,2} = X$ (16,17). Although not widely appreciated bipolar encoding is more time-efficient for low VENCs and FCFE is more time efficient for mid to high VENCs. Furthermore, FCFE provides reduced signal loss due to intravoxel coherent velocity-related phase dispersion (20,21), such as in the presence of shear or complex flow, and reduced ghosting artifacts in the phase encode direction arising from large M_1 induced velocity-related phase shifts (15).

However, in the presence of perivascular fat, the chemical shift difference between water and lipids can give rise to non-velocity phase, which can be minimized by selection of optimal timings, to keep the water and lipid signals in-phase (5). The design of the flow-encoding gradients is thus further constrained by their total duration if the criteria for minimum in-phase echo-time is to be satisfied: $TE_{IN,MIN} = 2.46$ ms at 3T. Bernstein et al. (22) previously defined strategies for minimizing TE times in PC-MRI sequences for both bipolar and FCFE encoding and our proposed methods makes further reductions in TE possible.

Previously, time-efficient velocity-encoding without the need for time-consuming bi-lobe encoding gradients has been achieved by taking advantage of the intrinsic first-moment of the slice-selection gradient waveform and refocusing lobe (9,10). Markl et al. (58) previously developed a balanced steady-state free precession phase contrast pulse sequence that used a slice selection gradient with alternating polarity for each encoding step, thereby combining the velocity encoding with the slice selection and slice select refocusing gradient. Thompson et al. (59) used a time-shift of the refocusing lobe and bipolar flow encoding lobe to control the velocity encoding strength without altering the slice-selection gradient. Herein, we adopt similar principles to significantly reduce the time needed to achieve velocity encoding over a range of clinically useful VENCs by using a time-shift of the refocusing lobe and no other flow encoding lobes. Our proposed technique is referred to throughout as the slice select refocusing gradient (SSRG) sequence.

The most common implementations of flow encoding gradients are shown in Fig. 28A, for flow compensated and flow encoded gradient waveforms (FCFE) and bipolar gradient waveforms, whereas our proposed SSRG velocity encoding technique is shown in Fig. 28B.

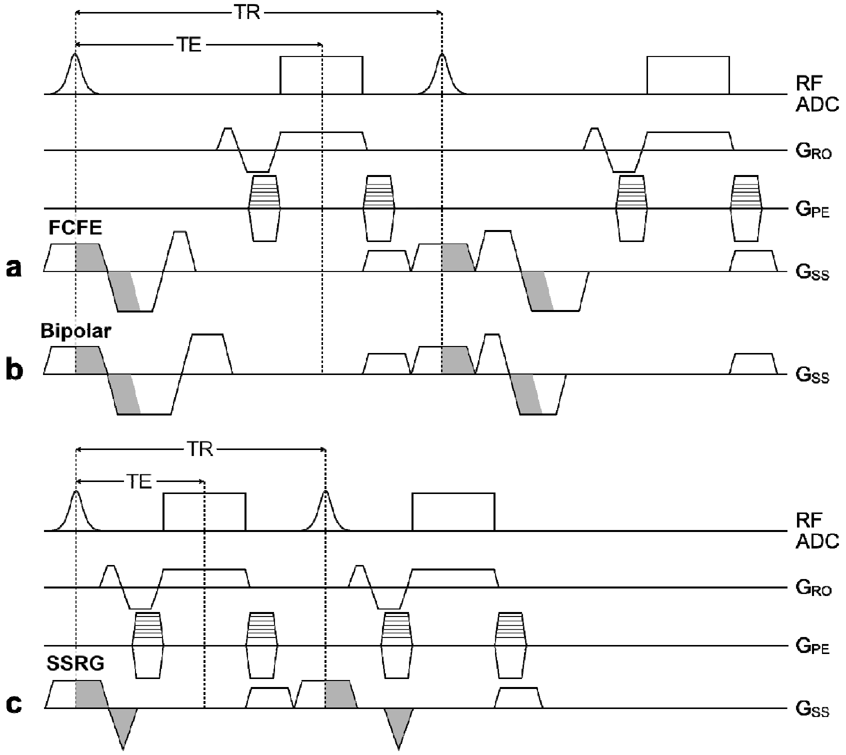

Figure 28. Pulse sequence diagrams for a conventional bipolar velocity encoded sequence at HBW and TE_{IN}, which uses a negative and positive velocity encoded waveform along slice select axis (a), our previous chemical shift optimized PC-MRI sequence using a conventional flow compensated and flow encoded (FCFE) velocity encoded sequence at HBW and TE_{IN}, (b), and slice select refocusing gradient (SSRG) velocity encoded sequence at HBW and $TE_{IN,MIN}$ (c). The SSRG sequence conducts velocity encoding using the slice selection and corresponding refocusing gradients that inherently has a nulled zero gradient moment ($M_0=0$), and a non-zero first moment ($M_1 \neq 0$), which provides velocity sensitivity. For the second measurement, the slice select refocusing gradient is shifted in time to produce the targeted velocity encoding strength (VENC) as detailed in Fig. 29 and Eq. [8]. The SSRG sequence permits the use of $TE_{IN,MIN}$ whereas the other conventional sequences cannot achieve this TE.

For our SSRG method, the relationship between the gradient parameters and the resulting zero, M_0, and first moments, M_1, and thus the VENC, can be determined analytically. Parameters characterizing a typical slice select and refocusing gradient waveform for a symmetric RF pulse are shown in Fig 29. For any given RF pulse, the amplitude, G_S, is determined by the desired slice thickness while the length of the slice select gradient lobe, t_S, is determined by the duration of the RF pulse. The M_0 of the slice select gradient lobe, $M_{0,S}$, and refocusing gradient lobe, $M_{0,R}$, must be equal ($M_{0,S} = M_{0,R}$) to ensure that all excited spins are refocused over the thickness of the slice after excitation:

$$M_{0,R} - G_S t_S. \qquad [3]$$

The amplitude of the refocusing gradient lobe, G_R, can be determined by using the minimum available gradient rise time of the system, r_R, and the result of Eq. [3]:

$$G_R = \frac{M_{0,R}}{r_R}. \qquad [4]$$

The first moment for a symmetric gradient waveform (i.e. the refocusing lobe) centered at any point in time, t, can be determined by $M_1 = M_0\, t$. Thus, for the first encoding step, with the refocusing gradient lobe centered at $t = t_S + r_R$, the first moment of the refocusing gradient lobe can be calculated as $M_{0,R}\,(t_S + r_R)$. The non-zero first moment of the entire gradient waveform for the first encoding step, $M_{1,1}$, is thus given by

$$M_{1,1} - M_{1,S} + M_{1,R} - M_{1,S} - M_{0,R}\left(t_S + r_R\right). \qquad [5]$$

For the second encoding step, the refocusing gradient lobe is shifted in time by Δt and is thus centered at $t = t_S + r_R + \Delta t$, resulting in a first moment of $M_{0,R}\,(t_S + r_R + \Delta t)$. The non-zero first moment of the entire gradient waveform for the second encoding step, $M_{1,2}$, can be determined as

$$M_{1,2} - M_{1,S} + M_{1,R} - M_{1,S} - M_{0,R}\left(t_S + \Delta t + r_R\right). \qquad [6]$$

The slice select gradient lobe is identical for the two encoding steps and thus it’s first moment contribution cancels when calculating the net first moment, ΔM_1

$$\Delta M_1 = M_{1,1} - M_{1,1} = M_{0.R}\Delta t. \qquad [7]$$

Substituting Eq. [7] in Eq. [2] above, the time shift for the target VENC is

$$\Delta t = \frac{\pi}{\gamma M_{0,R} VENC}. \qquad [8]$$

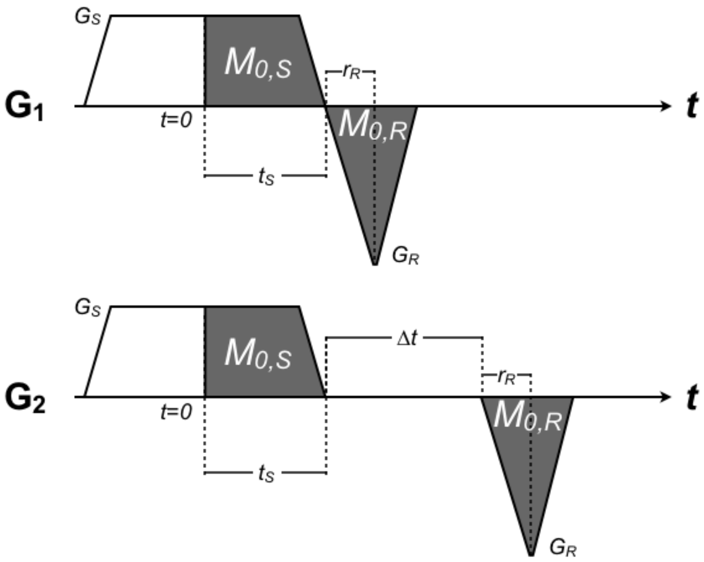

Figure 29. Slice select and refocusing gradient lobes for the SSRG PC-MRI sequence. The slice thickness and RF duration determines $M_{0,S}$ of the slice select gradient lobe from $t=0$. A time efficient triangular refocusing gradient lobe is constructed such that $M_{0,R} = M_{0,S}$. The refocusing gradient lobe for the second measurement is shifted in time by Δt to produce the target VENC. $M_{0,S}$ is the area of the slice select gradient; G_S is slice select gradient amplitude; t_S is the duration of the slice select gradient; $M_{0,R}$ is the area of the refocusing gradient; r_R is the duration of the refocusing gradient ramp from 0 to G_R; and Δt is the time shift of the refocusing gradient needed to produce the ΔM_1 associated with the target VENC.

METHODS

Comparison of Velocity Encoding Strategies

The minimum available TE as a function of VENC was determined for FCFE, bipolar, and SSRG sequences. The TE and VENC were determined at both low bandwidth (LBW) = 401 Hz/px and high bandwidth (HBW) = 814 Hz/px with all other parameters held constant (192 × 120 encoding matrix, 1.6 mm × 1.6 mm spatial resolution, 5 mm slice thickness, 30° flip angle, 4 views-per-segment, 500 μs RF pulse width, and a maximum slew rate of 157 mT/m/ms).

Preclinical Evaluation in Normal Volunteers

A preclinical evaluation of SSRG was performed in ten normal volunteers (N=10) to show that SSRG suppresses chemical shift effects while shortening the TE/TR compared to FCFE. All imaging was performed on a Siemens Trio 3 Tesla system (Siemens Medical Solutions, Erlangen, Germany) with 40 mT/m maximum gradient amplitude and 200 T/m/s maximum slew rate. Our university's Institutional Review Board approved the study and informed consent was obtained for each subject prior to MRI scanning. Subjects were positioned head first in the supine position on the scanner bed and imaged using an anterior 6-element body matrix coil and a posterior 6-element spine matrix coil for signal reception. Blood flow was measured using PC-MRI in the ascending aorta (aAo), main pulmonary artery (PA), and right/left pulmonary arteries (RPA/LPA) of ten (N=10) volunteers (2 female, 8 male; age 27.6 ± 4.0 years) with no previous history of cardiovascular disease. High-resolution black blood turbo spin echo images were also acquired with and without fat saturation (45,46) during end-systole in order to define the presence (or absence) of perivascular fat for the vessel of interest at the same slice location used for PC-MRI flow measurements.

The imaging plane for aAo flow was located distal to the aortic valve and coronary ostia. The imaging plane for flow in the PA was located downstream from the pulmonary valve and proximal to the first bifurcation. The imaging planes for the LPA and RPA were located ~1 cm distal to the pulmonary bifurcation. All imaging planes were prescribed on bSSFP cine images during end-systole with end-expiratory breath holds.

PC-MRI flow measurements were obtained using a FCFE cine gradient echo phase-contrast sequence with retrospective ECG gating: mid-phase TE (TE_{MID}=3.08ms), which orients the fat vector to be approximately perpendicular to the blood vector, TR=6.04 ms, 192 × 132 matrix, 1.6 mm × 1.6 mm × 5 mm acquisition voxel, 30° imaging flip angle, 401 Hz/pixel receiver bandwidth (LBW), 4 views-per-segment (60), a total scan time of 20 heartbeats, a temporal resolution of 48.3 ms, 20-24 cardiac phases (heart rate dependent) reconstructed during one end-expiratory breath hold with retrospective ECG gating, and GRAPPA (44) parallel imaging with an acceleration factor of 2 and 24 reference (central) *k*-space lines. 2D through-plane velocity encoding was performed using VENC of 200 cm/s for all flow territories. While it is possible to fine-tune the VENC for each subject and each particular vessel, this will introduce changes in the TE and TR, which can be confounding when making comparisons in a controlled study. Therefore, the VENC was kept high enough to reduce the risk of aliasing and was therefore held constant for all subjects and all vessels. Fractional echo was not used for any sequence.

Both TE_{MID} = 3.08 ms and LBW = 401 Hz/px were found to be close approximations to commonly used values in clinical scans found in current PC-MRI literature (61-63). This combination of TE and BW sensitizes the measurements to the effects of chemical shift. Measurements were also obtained using the SSRG velocity encoding sequence with identical parameters as described above, except for the following changes: $TE_{IN,MIN}$/TR =

2.46/4.46 ms, 814 Hz/px receiver bandwidth (HBW), a temporal resolution of 35.65 ms, and 27-32 reconstructed cardiac phases (heart rate dependent). Additional data was also acquired using FCFE with our previously defined optimized chemical shift protocol: TE_{IN}/TR = 4.92/6.91 ms, 814 Hz/pixel receiver bandwidth (HBW), a temporal resolution of 55.3 ms and 17-21 reconstructed cardiac phases. Both FCFE at HBW+TE_{IN} and SSRG at HBW+$TE_{IN,MIN}$ theoretically provide the same insensitivity to chemical shift induced phase errors, but SSRG at HBW+$TE_{IN,MIN}$ provides increased SNR and a shorter TR (i.e. improved temporal resolution or shorter breath hold durations) due to the TE/TR reduction.

Image Processing

Data were processed offline using MATLAB (The MathWorks, Natick, MA) and a DICOM viewing tool (Osirix, www.osirix-viewer.com). Eddy current background phase errors were measured and corrected, for all sequences, using a stationary phantom (25,29,30,47) after each exam. For quantitative flow assessment at each vessel territory, a region-of-interest (ROI) was drawn in Osirix around the contours of each vessel boundary as indicated in the magnitude images. The same ROIs were imported into the eddy current correction images for correction of background phase errors. The resulting ROI information was then exported from Osirix to MATLAB for quantitative velocity and flow analysis. The measured net forward flow of blood was computed by scaling the mean ROI signal intensity (velocity related phase shift) by VENC/π (cm/s). The resulting mean ROI velocities were then multiplied by the area of the ROI (cm^2) to calculate the flow rate (mL/s) and finally integrated over the cardiac cycle to yield the net forward flow results (mL).

Data Analysis

Chemical Shift Effects on Net Forward Flow – To analyze the effects of chemical shift on net forward flow, measurements were made in the aAo, PA, RPA, and LPA for FCFE with LBW+TE_{MID} and HBW+TE_{IN} as well as SSRG with HBW+$TE_{IN,MIN}$.

Internal Blood Flow Consistency – An analysis of the internal blood flow consistency was conducted by comparing the measured net forward flow in the aAo and PA, aAo and RPA+LPA, and the PA and RPA+LPA for FCFE with LBW+TE_{MID} and SSRG with HBW+$TE_{IN,MIN}$. In the absence of shunts or regurgitant flow (neither of which is expected within our normal volunteer population) we expect that the blood flow in the PA = 1.05•aAo (accounting for coronary flow (64)) = RPA + LPA. A two-sample t-test with Holm-Sidak *post hoc* correction was used to measure the statistical significance of the differences in the measured net forward flow between the two sequences.

Eddy Current Comparison – Eddy current-induced velocity offsets were measured by copying the manually contoured ROIs from each volunteer and vessel to the eddy current correction images. The eddy current-induced velocity offsets were compared by averaging the mean velocity from each ROI through time for SSRG at HBW+$TE_{IN,MIN}$ and FCFE at LBW+TE_{MIN} and HBW+TE_{IN}.

The magnitude of chemical shift and eddy current-induced flow errors were compared. Chemical shift-induced flow errors were obtained by calculating the mean, standard deviation, and minimum/maximum of the flow error (mL) between the aAo and PA, aAo and RPA+LPA, and the PA and RPA+LPA, between FCFE at LBW+TE_{MID} and SSRG at HBW+$TE_{IN,MIN}$. Eddy current-induced flow errors were similarly calculated as the flow difference arising from measurements with and without eddy current correction, for both sequences. A two-sample t-test was used to measure the statistical significance of the differences in flow errors arising from eddy currents and chemical shift.

Pulmonary to Systemic Blood Flow Ratios – Pulmonary to systemic blood flow ratios (Qp/Qs, PA flow divided by aAo flow) were calculated for each volunteer. A two-sample t-test with Holm-Sidak *post hoc* correction was used to measure the statistical significance of the differences in the measured Qp/Qs ratios for FCFE with LBW+TE_{MID} and SSRG with HBW+$TE_{IN,MIN}$.

Signal-to-Noise Ratio Comparison – A quantitative analysis of the measured SNR for FCFE with HBW+TE_{IN} and LBW+TE_{MID} and SSRG with HBW+$TE_{IN,MIN}$ was conducted by placing two ROIs within the magnitude images to produce an estimate of the signal and the noise. One set of ROIs was contoured to the aAo, PA, RPA, or LPA to obtain a measurement of the mean signal for each cardiac phase. Another set of ROIs was placed outside the subject's body to obtain an estimate of the background signal standard deviation (noise) for each cardiac phase. The noise ROIs were placed near the top left portion of the images in a region that was devoid of any artifacts as observed under window/level extremes. The mean ± standard deviation SNR for each vessel and each subject was computed as the mean of the mean signal intensity divided by the standard deviation for each cardiac phase for each sequence. The mean ± standard deviation of the SNR for each vessel territory was compared between sequences.

RESULTS

Comparison of Velocity Encoding Strategies – Figure 30 shows the minimum available TE (ms) plotted as a function of the available VENC (cm/s) for FCFE, bipolar, and SSRG velocity encoding strategies at both LBW (Fig 30a) and HBW (Fig 30b). SSRG is the only encoding strategy that permits the use of $TE_{IN,MIN}$ = 2.46 ms at HBW, which occurs for VENCs ≥ 190 cm/s. The minimum achievable TE at LBW is 2.84 ms, which can only be reached with SSRG for VENCs ≥ 190 cm/s. SSRG also permits the shortest TE for all VENCs ≥ 165 cm/s. FCFE yields the shortest TE for 35 cm/s < VENC < 165 cm/s. The bipolar sequence provides the use of the shortest TE for VENCs ≤ 35 cm/s. FCFE allows shorter minimum TEs compared to the bipolar sequence for the VENCs used in this study, therefore our new SSRG velocity encoding sequence was only compared to FCFE.

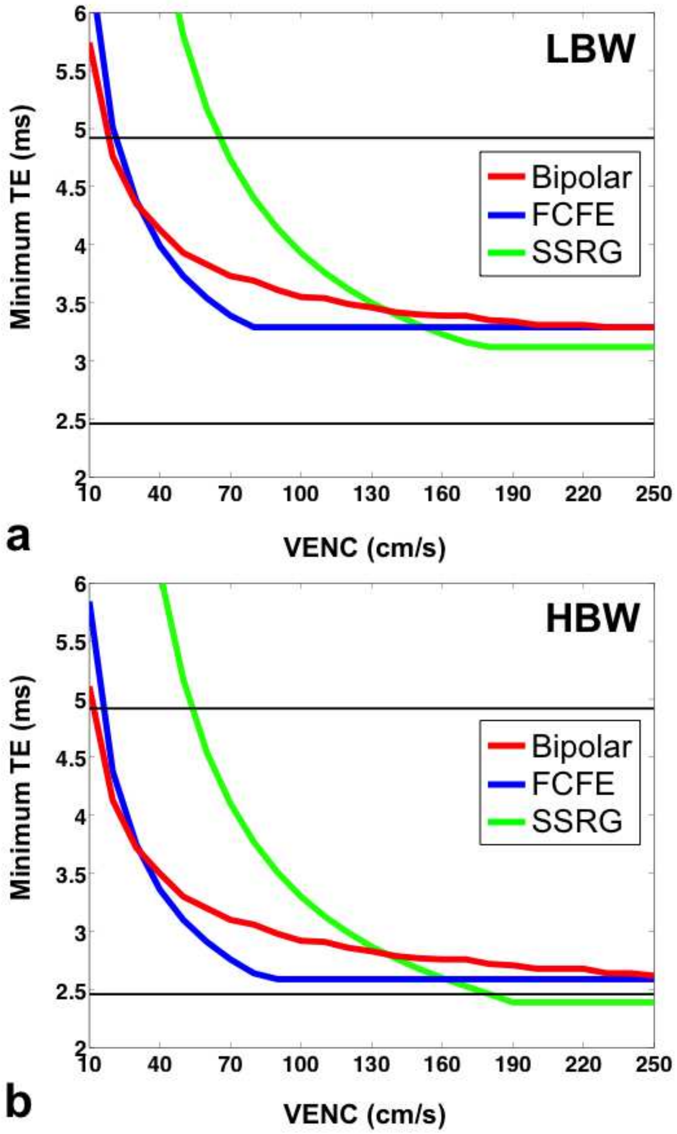

Figure 30. Minimum achievable TE (ms) plotted as a function of the target VENC (cm/s) for conventional bipolar velocity encoding (red), conventional flow compensated and flow encoded (FCFE) velocity encoding (blue), and slice select refocusing gradient (SSRG) velocity encoding (green) shown for (a) low bandwidth (LBW) = 401 Hz/px and (b) high bandwidth (HBW) = 814 Hz/px. The SSRG sequence is the only encoding strategy that permits the use of $\text{TE}_{\text{IN,MIN}}$ = 2.46 ms at HBW, which occurs for VENCs ≥ 190 cm/s. The minimum achievable

TE at LBW is 2.84 ms, which can only be reached with the SSRG sequence for VENCs ≥ 190 cm/s. The SSRG sequence also permits the shortest TE for all VENCs ≥ 165 cm/s at HBW and VENCs ≥ 130 cm/s at LBW. The FCFE sequence yields the shortest TE for 35 cm/s < VENC < 165 cm/s at HBW and 35 cm/s < VENC < 130 cm/s at LBW. The bipolar sequence permits the shortest TE for VENCs ≤ 35 cm/s at HBW and LBW. As the VENC increases, a theoretical minimum TE is reached due to limitations associated with the plateau of the readout gradient overlapping with the refocusing gradient. The SSRG sequence can generate a larger M_1 (lower VENC) within this time, compared to the other encoding strategies, thus permitting the use of a shorter TE. All other parameters were held constant (192 × 120 encoding matrix, 1.6 mm × 1.6 mm × 5 mm acquisition voxel, 30° flip angle, 4 views-per-segment, 500 μs RF pulse width, and a maximum slew rate of 157 mT/m/ms).

In Vivo Studies

Chemical Shift Effects on Net Forward Flow – Figure 31 shows the difference in the measured net forward flow data from the aAo, PA, RPA, and LPA for FCFE with LBW+TE_{MID} and SSRG with HBW+$TE_{IN,MIN,}$ which qualitatively illustrates chemical shift induced flow errors. The TSE images with and without fat saturation were used to detail the presence or absence of perivascular fat for each vessel in each volunteer (Fig. 32). In the presence of perivascular fat, FCFE with LBW+TE_{MID} led to an overestimation of the net forward flow compared to SSRG with HBW+$TE_{IN,MIN}$ (aAo: 7.2±1.6% vs. 1.6±0.3%; PA: 8.5±2.7% vs. 3.8%; RPA: 11.4±2.3% vs. 3.3%; and LPA: 8.8±2.8% vs. 2.3±2.8%). The mean difference, across all volunteers and vessels, between the measured net flow for FCFE with HBW+TE_{IN} and SSRG with HBW+$TE_{IN,MIN}$ was 1.1 ml (2.1%).

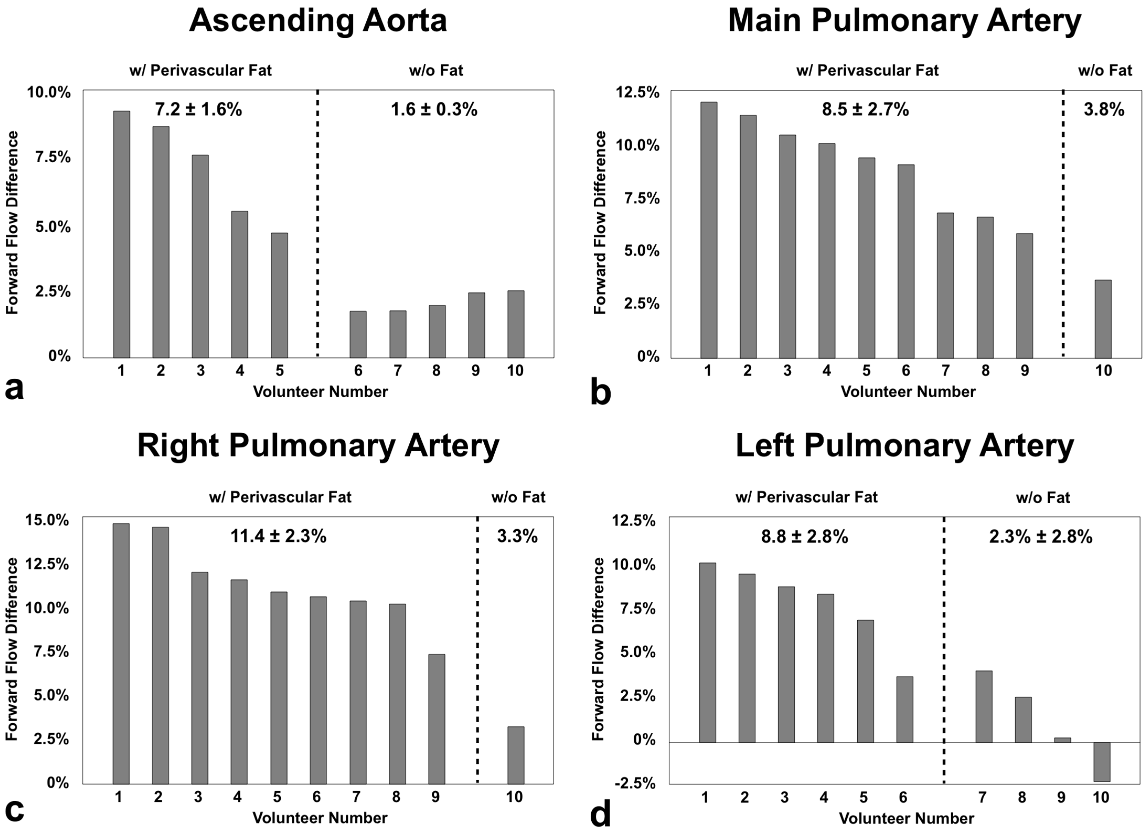

Figure 31. Differences in measured net forward flow between the conventional flow compensated and flow encoded (FCFE) velocity encoding sequence at LBW+TE_{MID} and the slice select refocusing gradient (SSRG) sequence at HBW+$TE_{IN,MIN}$ expressed as a percentage. Vessels with observed perivascular fat on TSE black blood images are shown to the left of the vertical dashed line whereas vessels with minimal perivascular fat are shown to the right of the vertical dashed line. Results were obtained in the (a) ascending aorta (aAo), (b) main pulmonary artery (PA), and the (c) right and (d) left branch pulmonary arteries (RPA/LPA). In the presence of perivascular fat, FCFE at LBW+TE_{MID} leads to an overestimation in net forward flow (theoretically and empirically) compared to SSRG at HBW+$TE_{IN,MIN}$ sequence, for all vessel territories except volunteer number 10 in the LPA. Chemical shift induced phase errors are largest

for low pressure vessels (PA, RPA, and LPA) compared to the aAo which has a thicker vessel wall, thus limiting the perivascular fat signal from spatially shifting into the vessel lumen.

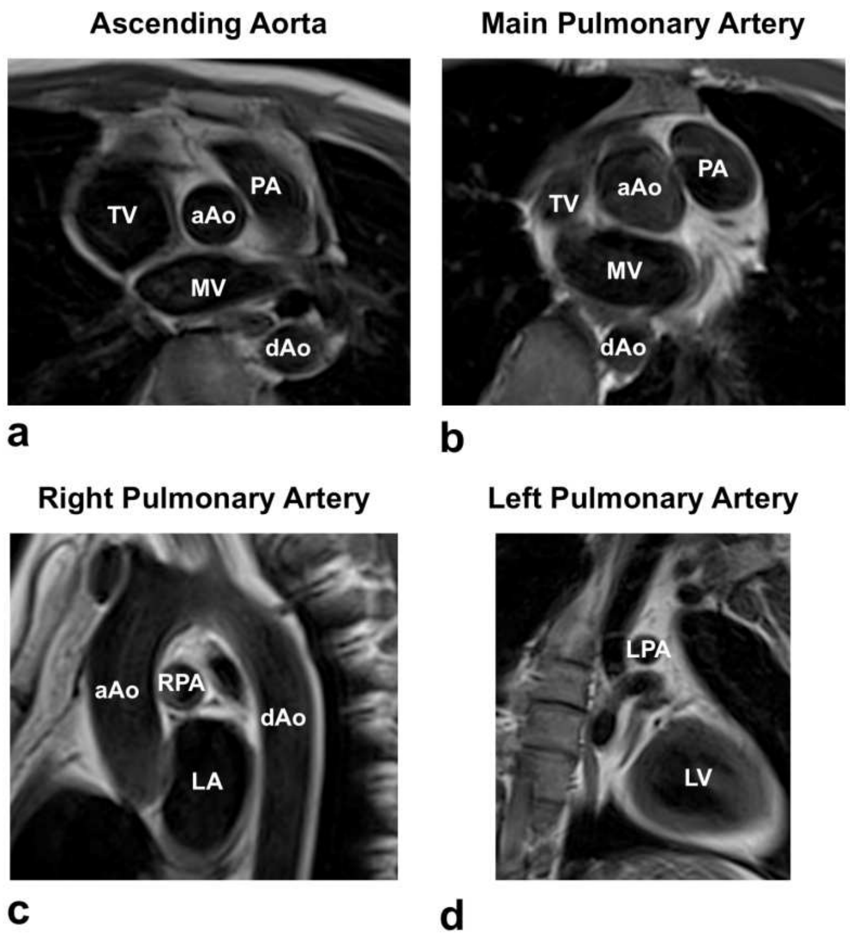

Figure 32. Black blood turbo spin-echo images highlight the presence of perivascular fat around the ascending aorta (aAo) (a), main pulmonary artery (PA) (b), right pulmonary artery (RPA) (c), and left pulmonary artery (LPA) (d). TV-Tricuspid valve; MV-mitral valve; dAo-descending aorta; LA-left atrium; and LV-left ventricle.

Internal Blood Flow Consistency – Table 4 shows an analysis of the internal consistency for net forward flow measurements made in the aAo, PA, RPA, and LPA from our preclinical evaluation of ten normal volunteers (N=10). Included in the analysis is the mean percent agreement and the minimum and maximum percent agreement (shown in brackets). In all three territory comparisons (aAo vs. PA, aAo vs. RPA+LPA, and PA vs. RPA+LPA) a statistically significant difference ($P<0.05$) between the measured net forward flow for FCFE with LBW+TE_{MID} and SSRG with HBW+$TE_{IN,MIN}$ is observed. This indicates significant improvement in the internal consistency of flow measures through the reduction of chemical shift-induced phase errors using SSRG with HBW+$TE_{IN,MIN}$. A comparison of the measured net flow between FCFE with HBW+TE_{IN} and SSRG with HBW+$TE_{IN,MIN}$ showed no significant difference.

Table 4: Intra-patient percent flow difference from the pre-clinical evaluation of ten normal volunteers (N=10) expressed as a mean±SD [minimum, maximum].

	FCFE LBW+TE$_{MID}$	**SSRG HBW+TE$_{IN,MIN}$**	***P-Value**
aAo vs. PA	5.8 ± 2.8% [0.98, 8.9%]	1.7 ± 1.9% [0.16, 2.8%]	0.002
aAo vs. RPA+LPA	6.0 ± 4.3% [0.85, 9.8%]	2.1 ± 1.7% [0.60, 2.5%]	0.03
PA vs. RPA+LPA	6.1 ± 6.3% [0.11, 7.6%]	2.9 ± 2.1% [0.57, 2.2%]	0.04

*P < 0.05 show a statistical significant difference between FCFE LBW+TE$_{MID}$ and SSRG HBW+TE$_{IN,MIN}$ indicating significant improvement in internal consistency flow measures using SSRG HBW+TE$_{IN,MIN}$ in PC-MRI.

Figure 33 shows an analysis of the internal consistency for net forward flow (aAo vs. PA, aAo vs. RPA+LPA, and PA vs. RPA+LPA) measured by FCFE with LBW+TE_{MID} and SSRG with HBW+$TE_{IN,MIN}$ with and without eddy current correction. SSRG with HBW+$TE_{IN,MIN}$ improves the intra-subject forward flow agreement for every subject. Eddy current corrected SSRG with HBW+$TE_{IN,MIN}$ leads to better intra-subject flow agreement on average compared to FCFE with LBW+TE_{MID}.

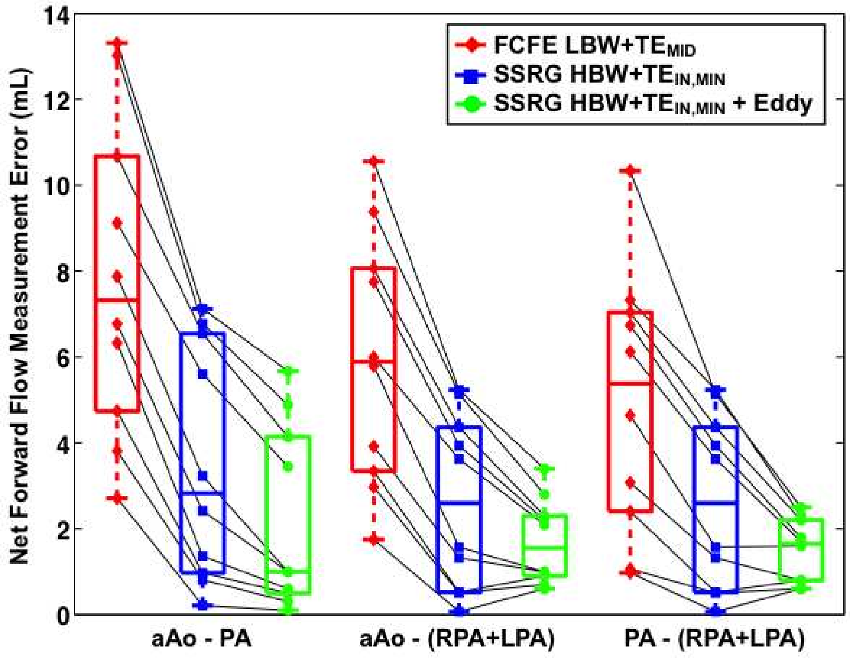

Figure 33. Net forward flow measurement error between the conventional FCFE velocity-encoding sequence at LBW+TE$_{MID}$ without (orange) and with (blue) eddy current correction compared with the SSRG sequence at HBW+TE$_{IN,MIN}$ without (green) and with (red) eddy current correction. Data from individual subjects (N=10) are connected to show that eddy current-corrected SSRG at HBW+TE$_{IN,MIN}$ improves the intrasubject forward flow agreement for every subject compared with eddy current-corrected FCFE with LBW+TE$_{MID}$. Correcting for eddy currents further improves the agreement. The box plot shows the median and 25th and 75th percentiles and the error bars show the 95% confidence intervals.

Table 5 shows the importance of comparing relative and absolute blood flow comparisons for both SSRG with HBW+$TE_{IN,MIN}$ and FCFE with LBW+TE_{MID} from a single volunteer with observed perivascular fat.

Table 5: Internal consistency from the preclinical evaluation of one normal volunteer (N=1) showing the importance between absolute and relative blood flow quantification. The SSRG technique is known theoretically and empirically to produce more accurate flow measurements.

	FCFE LBW+TE_{MID}	**SSRG HBW+$TE_{IN,MIN}$**	**Δ Inter Flow**
PA	99.3 mL	90.7 mL	8.6 mL
RPA+LPA	98.0 mL	89.9 mL	8.1 mL
Δ Intra Flow	1.3 mL	0.8 mL	

Δ Inter Flow = FCFE LBW+TE_{MID} - SSRG HBW+$TE_{IN,MIN}$ for each flow territory

Δ Intra Flow = PA - (RPA+LPA) for each sequence

All vessels contained perivascular fat

Eddy Current Comparison – Eddy current-induced velocity offsets for SSRG with HBW+$TE_{IN,MIN}$, FCFE with LBW+TE_{MIN}, and FCFE with HBW+TE_{IN} were 0.6 ± 0.37cm/s, 0.4 ± 0.19cm/s, and 0.52 ± 0.27 cm/s, respectively. The average magnitude of chemical shift induced flow errors was 2.9 ± 1.6mL [0.0mL, 6.4mL] (mean ± SD [min, max]). The average magnitude of eddy current-induced flow errors was 1.56 ± 1.16mL [0.03mL, 4.6mL].

Pulmonary to Systemic Blood Flow Ratios – The Qp/Qs ratios for SSRG with HBW+$TE_{IN,MIN}$ were lower and significantly different than FCFE with LBW+TE_{MID} (1.00 ± 0.02 vs. 1.05 ± 0.04, $P<0.005$).

SNR Comparison – The average measured SNR for SSRG with HBW+$TE_{IN,MIN}$, FCFE with HBW+TE_{IN}, and FCFE with LBW+TE_{MID} was 58.5 ± 24.8, 87.7 ± 40.8, and 116.8 ± 54.4, respectively.

Sequence Timing Comparison – Table 6 shows a comparison of the timing parameters for FCFE with LBW+TE_{MIN} and HBW+TE_{IN} as well as SSRG with LBW+TE_{MIN} and HBW+$TE_{IN,MIN}$ for a VENC of 200 cm/s.

Table 6: Comparison of parameters for different velocity encoding sequences for a VENC of 200 cm/s.

	Reduced Chemical Shift Induced Phase Errors		**Fastest Sequence at Low Bandwidth**	
	FCFE HBW+TE$_{IN}$[a]	**SSRG HBW+TE$_{IN,MIN}$**	**FCFE LBW+TE$_{MIN}$**	**SSRG LBW+TE$_{MIN}$**
TE (ms)	4.92	2.46	3.29	2.84
TR (ms)	6.91	4.46	5.98	5.24
Temporal Resolution (ms)	55.3	35.65	47.85	41.95

[a] TE$_{IN,MIN}$ is unachievable with the FCFE velocity encoding sequence at 3T without the use of higher BW, fractional echo, or increasing the resolution.

DISCUSSION

Comparison of Velocity Encoding Strategies – In Fig. 30, as the VENC increases, a theoretical minimum TE is reached due to limitations associated with the plateau of the readout gradient overlapping with the refocusing gradient. SSRG can encode larger velocities within this time, compared to the other encoding strategies, thus permitting the use of a shorter TE. For a fixed slice select gradient and RF pulse, smaller VENC values require a Δt that causes the refocusing gradient lobe to overlap with the readout gradient plateau for $TE_{IN,MIN}$, thus causing an increase in the minimum achievable TE.

In Vivo Studies

Chemical Shift Effects on Net Forward Flow – In Fig. 31 it can be seen that chemical shift induced phase errors are largest in the PA, RPA, and LPA compared to the aAo. For low pressure vessels (PA, RPA, and LPA) the vessel wall is thicker, thus limiting the complex signal from perivascular fat from spatially shifting into the vessel lumen. In the presence of minimal perivascular fat, the difference between the two sequences is much lower. Only one volunteer lacked perivascular fat in the PA and another volunteer lacked perivascular fat in the RPA. Only once did FCFE with $LBW+TE_{MID}$ lead to an underestimation of the net forward flow compared to SSRG with $HBW+TE_{IN,MIN}$.

Internal Blood Flow Consistency – Table 4 shows a statistically significant difference ($P<0.05$) between the measured net forward flow for FCFE with $LBW+TE_{MID}$ and SSRG with $HBW+TE_{IN,MIN}$ in all three territory comparisons (aAo vs. PA, aAo vs. RPA+LPA, and PA vs. RPA+LPA). This indicates significant improvement in the internal consistency of flow measures through the reduction of chemical shift-induced phase errors using SSRG with HBW+$TE_{IN,MIN}$.

Internal consistency measures can only reflect a relative agreement in net forward flow, whereas for PC-MRI to provide the most clinically useful results, absolute flow measurements are preferred. In Table 5, FCFE with LBW+TE_{MID} shows a small intra sequence difference of ~1 mL (1.4%). Importantly, SSRG with HBW+$TE_{IN,MIN}$ shows a similar result (Δ intra flow < 1 mL). However, when the inter sequence flow differences are compared FCFE with LBW+TE_{MID} shows an overestimation of blood flow by ~8 mL (9.3%). In this work FCFE with LBW+TE_{MID} led to an overestimation of blood flow in all but one vessel territory (39 out of 40) in ten volunteers, which is also consistent with our previous results (5). While this study reports a consistent overestimation of flow when using LBW+TE_{MID}, the magnitude and sign of the flow discrepancy depends on the superposition of the complex fat and water vectors. For this work, the use of LBW causes more fat pixels to partial volume with blood pixels within the vessel, while the use of TE_{MID} causes the fat vector to be oriented approximately perpendicular to the blood vector. Together, LBW+TE_{MID} leads to an increase in the measured phase (flow), whereas our chemical shift optimized sequence reduces the extent of fat pixels that partial volume with blood pixels by using a HBW and orients the fat vector more closely with that of slow flowing blood near the vessel wall by using TE_{IN}. Table 5 shows that FCFE with LBW+TE_{MID} demonstrates excellent relative agreement in blood flow (Δ Intra flow) between the PA and the RPA+LPA, but a poor agreement in absolute blood flow (Δ Inter flow) due to chemical shift effects arising from the presence of perivascular fat surrounding these vessels for this volunteer. Similar results are observed in flow phantom experiments, where the measured flow is known (data not shown). These examples highlight why improvements need to be made to make PC-MRI an absolute method for quantifying blood flow and also underscores an important source of variability in clinical PC-MRI measurements.

Eddy Current Comparison – Eddy current-induced velocity offsets for SSRG with HBW+$TE_{IN,MIN}$ were greater than both FCFE with LBW+TE_{MIN} and HBW+TE_{IN}, but importantly just within the 0.6 cm/s threshold of acceptable eddy current-induced velocity offsets (26,27). Eddy current background phase error corrections significantly improve the flow accuracy of PC-MRI (2,18,20). In this study we have shown that the average magnitude of chemical shift induced flow errors are almost two-times larger and statistically different ($P<5e-5$) than eddy current effects. Therefore, for studies in which flow accuracy is important both eddy currents and chemical shift induced phases errors need to be minimized.

Pulmonary to Systemic Blood Flow Ratios – Relative to SSRG, FCFE measurements of Qp/Qs are higher on average by 0.05. Chemical shift effects primarily account for the 0.05 difference between SSRG and FCFE. Our Qp/Qs results for SSRG at HBW $TE_{IN,MIN}$, however, do not match the expected result of 1.05 when a 5% coronary flow contribution is assumed (22). Uncorrected phase errors could be influencing the measurements made with either SSRG or FCFE. Uncorrected phase errors that differentially contribute approximately 0.3cm/s, for example, to the aAo and PA measures could give rise to an error of ±0.05 in Qp/Qs (17), for either SSRG or FCFE, and could account for the deviation of the reported results from the expected value. The source of this error is incompletely understood.

SNR Comparison – A quantitative analysis of the measured SNR shows the SNR for SSRG with HBW+$TE_{IN,MIN}$ is reduced by 50% compared to FCFE with LBW+TE_{MID} and 33% higher than in our previous chemical shift optimized FCFE velocity encoding sequence with HBW+TE_{IN}. Both of these values are in good agreement with our theoretical expectation of 46% and 35%, respectively, determined based on the steady-state gradient echo signal equation and the applied flip angle, TE/TR, receiver bandwidth, and estimates of T_1/T_2^* (1400/50 ms).

Sequence Timing Comparison – Table 6 shows that with chemical shift optimized sequences, SSRG offers a 35% increase in temporal resolution compared to FCFE (35.65 vs. 55.3 ms). When chemical shift effects are not of a concern, the minimum available TE/TR for SSRG offers an 12% increase in temporal resolution compared to FCFE (41.95 vs. 47.85 ms). Regardless of chemical shift induced errors, SSRG always provides the shortest TE/TR (highest temporal resolution) compared to FCFE for the previously described VENC range.

Flow compensated images from a FCFE sequence have reduced flow-related ghosting artifacts in the phase-encode direction. However, FCFE always has one encoding step that is not flow compensated, therefore flow-related ghosting artifacts cannot be avoided within this encoding step. The SSRG sequence has no flow compensated waveforms, but the moment distribution compared to FCFE is similar and consequently flow-related ghosting artifacts were nearly identical to FCFE. For example, when using SSRG with a VENC of 200cm/s, $M_{1,1}$ = 2.3 (mT•ms^2)/m and $M_{1,2}$ = 8.17 (mT•ms^2)/m, whereas for FCFE $M_{1,1}$ = 0 and $M_{1,2}$ = 5.87 (mT•ms^2)/m.

SSRG can also be combined with the shared velocity encoding (SVE) technique proposed by Lin et al. (65) to offer an even greater increase in the effective temporal resolution. The SVE concept shares velocity encoding k-space data between adjacent frames. As a result, the SVE technique cannot be combined with FCFE encoding strategies since adjacent frames sharing the same velocity encoded k-space data would not provide any new information. Thus, an SSRG sequence combined with SVE image reconstruction would represent an important and significant increase in temporal resolution compared to conventional FCFE approaches.

Conventional wisdom for PC-MRI parameter selection has always been to pick a LBW for improved SNR and the corresponding minimum TE to further improve SNR and reduce the TR. While this approach has advantages, a judicious choice of BW and TE can lead to increased measurement accuracy by reducing the effects of chemical shift. Additionally, the 50% decrease in SNR with SSRG at HBW+$TE_{IN,MIN}$ compared to FCFE at LBW+TE_{MID} should not negatively impact measurement accuracy. For example, Westenberg et al. previously reported that a 55% reduction in SNR (187 ± 116 vs. 84 ± 60) did not lead to flow inaccuracies in measurements across the mitral valve (26).

SSRG enables the use of $TE_{IN,MIN}$, but under the conditions evaluated the use of FCFE at HBW+TE_{MIN} results in a TE that is close to $TE_{IN,MIN}$ (Δ = 0.14 ms), but this TE would orient the fat vector at approximately 21 degrees relative to stationary blood (water) for the 3T scanner (scanner reported B_0 = 2.89T) used in this study. Using our previous numerical simulations at 3T (57) indicates that FCFE at HBW+TE_{MIN} (2.6ms) can result in a forward flow error from chemical shift as large as 5% in the RPA/LPA (data not shown); a 2% reduction in SNR; and a 3% decrease in temporal resolution compared to SSRG at HBW+$TE_{IN,MIN}$. As a result, SSRG offers reduced chemical shift effects; faster scanning; and increased SNR for VENC ≥ 190cm/s.

Limitations

SSRG permits the use of a range of VENCs that are within the range of typical blood flow velocities for imaging the aAo, PA, RPA, and LPA. Smaller VENCs lead to a large time shift, Δt, for the refocusing gradient lobe during the second encoding step. Under these low VENC regimes, SSRG loses its velocity encoding time efficiency compared to the FCFE or bipolar sequences, which are more time efficient at encoding lower velocities. Therefore, SSRG is not well suited for measuring myocardial motion, CSF flow measurements, and other studies that require low VENCs (see Fig. 30). Furthermore, in this study the VENC was prospectively chosen to accommodate easily the maximum expected velocity in these subjects. Reducing the VENC requires increasing ΔM_1, which necessitates an increased M_1 for the time shifted slice-select refocusing gradient in SSRG. Consequently, this leads to increased intravoxel spin dephasing and potential ghosting artifacts (66). Furthermore, if the VENC had been more closely matched to the peak velocity, the impact of the higher M_1 values in SSRG compared to FCFE may have been more apparent (66).

The SSRG velocity encoding sequence allows the use of a shorter, previously unachievable $TE_{IN,MIN}$ of 2.46 ms at 3T. At 1.5T, $TE_{IN,MIN}$ = 4.76 ms (assuming ~210

Hz/px) and there is no shorter available TE_{IN} at this field strength. As a result, if chemical shift reduction strategies are to be employed at 1.5T, SSRG does not hold an advantage over FCFE. However, even if reducing the effects from chemical shift are not of interest, SSRG can still afford the use of a shorter TE/TR combination (Table 6) resulting in increased temporal resolution, breath hold duration and/or spatial resolution compared to FCFE.

We have assumed that the use of TE_{IN} aligns the complex fat vector with slow flowing blood at the vessel periphery, but this assumption is not always valid. For example, if the flow velocity is high as may occur for complex flow patterns, then the phase of fat may no longer closely align with the phase accorded by the local velocity. This highlights the importance of using HBW to minimize the contribution of perivascular fat.

When comparing our measured total flow results between the SSRG and FCFE techniques, the temporal resolution was not held constant. Instead, the minimum available TR was chosen for each technique to provide sequence efficiency. Despite the non-matched temporal resolutions, improvements in total flow agreement are considered to be a result of chemical shift effects and not temporal resolution as shown in our previous work (5) where the temporal resolution was held constant.

CONCLUSION

PC-MRI with SSRG velocity encoding is a more time efficient velocity encoding strategy for medium to large VENCs when used in conjunction with HBW. SSRG leads to more accurate and less variable flow measurements through the reduction of chemical shift-induced phase errors in addition to shortening the TE/TR, thus permitting the use of better temporal/spatial resolution and/or reduced breath hold duration.

CHAPTER 6

ASYMMETRIC VELOCITY ENCODING

Traditional PC-MRI methods employ either a pair of equal-and-opposite velocity encoding gradients (Bipolar) (14,15) or a flow compensated and flow encoded gradient pair (FCFE) (16,17). Each strategy has its benefits and drawbacks; but neither sequence is the most time efficiency over a wide range of clinically useful velocity encoding strengths. Asymmetric velocity encoding, which was briefly discussed in Chapter 3, is a more time efficient velocity encoding strategy compared to Bipolar and FCFE that does not mandate the distribution of first moments across the two velocity encoding acquisitions. In this chapter, we define the mathematics behind an iterative algorithm that is used to determine the gradient amplitudes, ramp durations, and plateau durations for a PC-MRI sequence which uses asymmetric velocity encoding for triangular and trapezoidal gradient waveforms (Specific Aim #3). Importantly, this algorithm doesn't just construct time efficient velocity encoding gradients, but also the corresponding flow compensated readout and phase encoding gradients. We ***hypothesize*** that reductions in TE/TR can be achieved by designing the fastest triangular and trapezoidal shaped velocity encoding gradient waveforms, providing significant increases in spatiotemporal resolution over conventional PC-MRI methods and more accurate measures of blood velocity and flow.

A fast iterative solution for time efficient trapezoidal and triangular gradient lobes for a pair of asymmetric velocity encoding gradients, a flow compensated readout gradient, and a phase encoding gradient can be used to determine the upper bound, T_u, for the CVX algorithm.

The gradients along the slice select axis (Fig. 34a,b) must be designed based on the moment constraints required for velocity encoding. In doing so, the velocity encoding gradient plateau variables (T_1, T_2, T_3, and T_4) can be determined as:

$$T_1 = -\frac{\frac{13G_{VE}^2}{8} - \sqrt{36SR_{VE}^2F_S^2G_S^2 + 72SR_{VE}^2F_SG_S^2R_S + 36SR_{VE}^2F_SG_SR_SG_{VE} + 24SR_{VE}^2F_SR_SG_{VE}^2}}{24SR_{VE}G_{VE}} + \cdots$$

$$\frac{\sqrt{36SR_{VE}^2G_S^2R_S^2 + 36SR_{VE}^2G_SR_S^2G_{VE} - 21SR_{VE}^2R_S^2G_{VE}^2 + 288\Delta M1SR_{VE}^2G_{VE}}}{24SR_{VE}G_{VE}} + \cdots$$

$$\frac{\sqrt{36SR_{VE}F_SG_SG_{VE}^2 - 24SR_{VE}F_SG_{VE}^3 + 36SR_{VE}G_SR_SG_{VE}^2 - 42SR_{VE}R_SG_{VE}^3 + 171G_{VE}^4}}{24SR_{VE}G_{VE}} + \cdots$$

$$\frac{SR_{VE}F_SG_S}{4} + \frac{SR_{VE}G_SR_S}{4} + \frac{SR_{VE}R_SG_{VE}}{8} \qquad [1a]$$

$$T_2 = \frac{\sqrt{6}\sqrt{6SR_{VE}^2F_S^2G_S^2 + 12SR_{VE}^2F_SG_S^2R_S + 6SR_{VE}^2F_SG_SR_SG_{VE} + 2SR_{VE}^2F_SR_SG_{VE}^2}}{12SR_{VE}G_{VE}} + \cdots$$

$$\frac{\sqrt{6}\sqrt{6SR_{VE}^2G_S^2R_S^2 + 6SR_{VE}^2G_SR_S^2G_{VE} - SR_{VE}^2R_S^2G_{VE}^2 - 24SR_{VE}^2T2^2G_{VE}^2 + 24\Delta M1SR_{VE}^2G_{VE}}}{12SR_{VE}G_{VE}} + \cdots$$

$$\frac{\sqrt{6}\sqrt{6SR_{VE}F_SG_SG_{VE}^2 - 2SR_{VE}F_SG_{VE}^3 + 6SR_{VE}G_SR_SG_{VE}^2 - 2SR_{VE}R_SG_{VE}^3 - 72SR_{VE}T2G_{VE}^3}}{12SR_{VE}G_{VE}} - \cdots$$

$$\frac{\sqrt{6}\sqrt{39G_{VE}^4} - 18G_{VE}^2}{12SR_{VE}G_{VE}} \qquad [1b]$$

$$T_3 = T_2 - \frac{R_S}{2} + \frac{G_{VE}}{2SR_{VE}} - \frac{F_sG_S}{2G_{VE}} - \frac{G_SR_S}{2G_{VE}} \qquad [1c]$$

$$T_4 = T_1 + \frac{G_S\left(F_S + R_S\right)}{2G_{VE}} \qquad [1d]$$

where the unknown parameters G_{VE} and SR_{VE} represent the plateau's gradient amplitude and slew rate, respectively, for the velocity encoding gradients applied along the slice select axis, which will be solved later. Additionally, the known parameters include F_S, which is the slice select gradient plateau duration, G_S, which is the slice select gradient amplitude, R_S, which is the slice select ramp down duration, and ΔM_1, which is the difference in first gradient moment and is determined by the desired VENC.

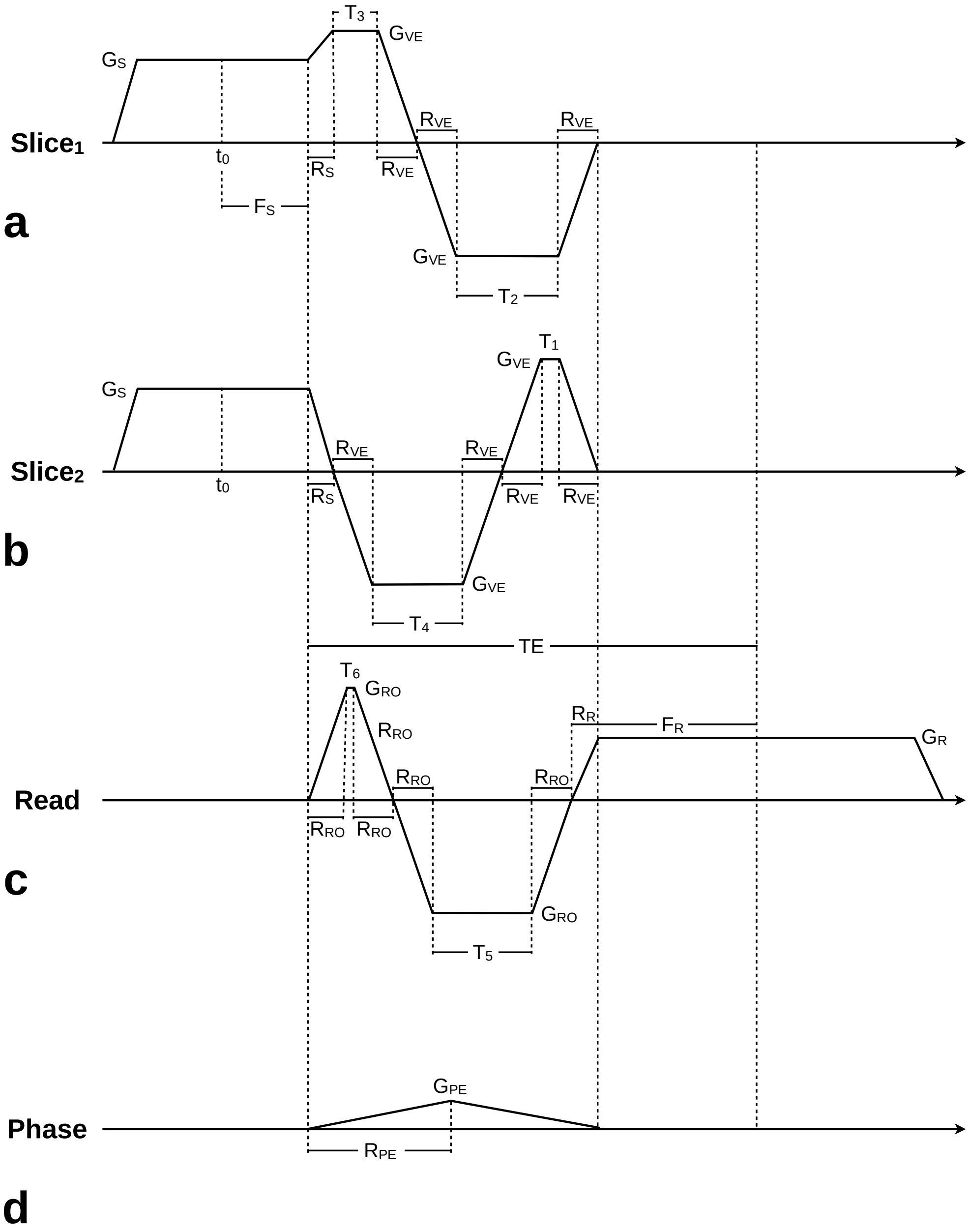

Figure 34. Pulse sequence diagram of the gradient waveform parameters for a pair of asymmetric velocity encoding gradients, a flow compensated readout gradient, and a phase encoding gradient using triangular and trapezoidal gradient waveforms. The unknown variables T_1, T_2, T_3, T_4, T_5, and T_6 are used to construct initial estimates of the gradient waveforms, which then define the upper bound (T_u) for the CVX optimization (Chapter 7).

Next, SR_{VE} is set to $SR_{VE} = SR_{Max}/\sqrt{3}$ and G_{VE} is searched from G_{Max} to 0 mT/m in increments of 0.0001 mT/m until a solution set for T_1, T_2, T_3, and T_4 meets the following condition, which ensures the duration of the two velocity encoding waveforms are equal:

$$|T_4 + T_1 + R_{VE} - T_3 - T_2| \leq 10\mu s \qquad [2]$$

where $R_{VE} = G_{VE}/SR_{VE}$ is the ramp duration of the velocity encoding gradients and 10μs represents the gradient sampling duration.

The phase encoding gradient must have a gradient area that corresponds to the maximum phase encode line and have the same duration as the velocity encoding gradients ($T_4 + T_1 + 4R_{VE} + R_S$). With these constraints in mind, a triangular phase encoding gradient can be constructed with ramp duration, R_{PE}, gradient amplitude, G_{PE}, and slew rate SR_{PE}:

$$R_{PE} = \frac{T_4 + T_1 + 4R_{VE} + R_S}{2} \qquad [3a]$$

$$G_{PE} = \frac{\pi\left(N_y - 1\right)}{\gamma FOV_y R_{PE}} \qquad [3b]$$

$$SR_{PE} = \frac{G_{PE}}{R_{PE}} \qquad [3c]$$

A time efficient flow compensated readout gradient would have a gradient ramp duration, R_{RO}, based on the maximum available gradient amplitude, G_{RO}, and slew rate, SR_{RO}:

$$SR_{RO} = \sqrt{G_{Max}^2 - G_{VE}^2 - G_{PE}^2} \qquad [4a]$$

$$SR_{RO} = \sqrt{SR_{Max}^2 - SR_{VE}^2 - SR_{PE}^2} \qquad [4b]$$

Taking into account the additional moment constraints required to achieve flow compensation at TE (M_0=M_1=0), the gradient plateau variables in Fig. 34c (T_5 and T_6) can be determined as:

$$T_5 = \frac{3\sqrt{\frac{G_R^2 F_R^2 S R_{RO}^2}{2} + \frac{4 G_R^2 F_R R_R S R_{RO}^2}{3} + \frac{17 G_R^2 R_R^2 S R_{RO}^2}{18} + \frac{G_R^2 F_R^2 S R_{RO}^2}{2} + \frac{4 F_R G_R^3 S R_{RO}}{3} + 2 G_R^2 F_R R_R S R_{RO}^2}}{6 G_R S R_{RO}} + \cdots$$

$$\frac{3\sqrt{2 G_R^3 R_R S R_{RO} + \frac{4 G_R^2 R_R^2 S R_{RO}^2}{3} + \frac{G_R^2 R_R S R_{RO}^2}{5} + G_R^4} + S R_{RO}\left(3 G_R F_R + 4 G_R R_R\right) - 9 G_R^2}{6 G_R S R_{RO}} \qquad [5a]$$

$$T_6 = T_5 - \frac{G_R\left(F_R + R_R\right)}{2 G_{RO}}. \qquad [5b]$$

Finally, the flow compensated readout duration must be equal to the duration of the velocity encoding and phase encode gradients (Fig. 34d). Thus, the entire process is repeated for another value of G_{VE} until the following additional criteria is met:

$$|T_4 + T_1 + 4R_{VE} + R_S - 4R_{RO} - T_5 - T_6 - R_R| \leq 10\mu s \qquad [6]$$

The entire process described above takes <1s to arrive at a solution using Matlab, which makes it an excellent method for assigning the upper bound for the CVX optimization.

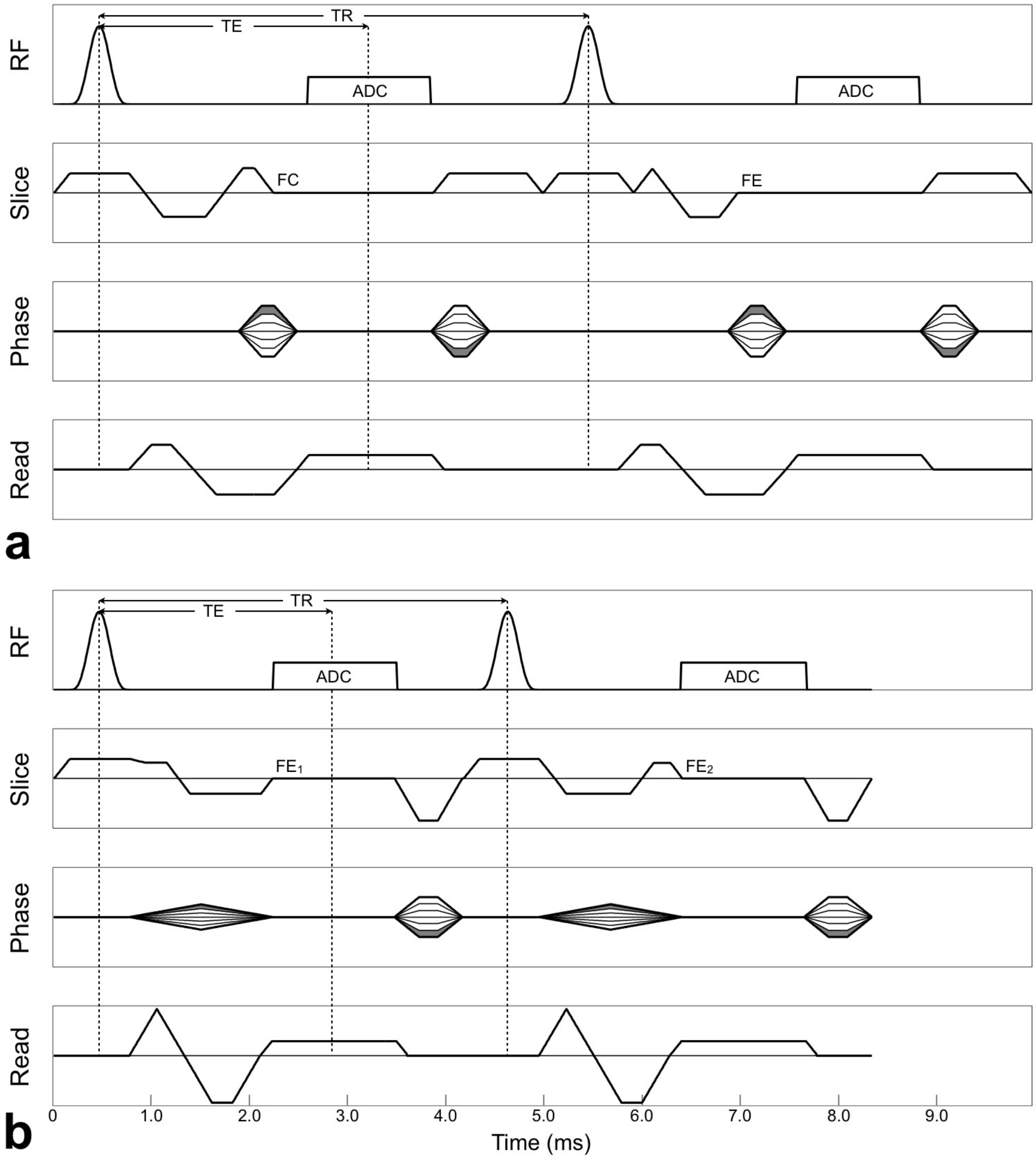

Figure 35. Pulse sequence diagram fro the standard FCFE PC-MRI sequence (A) and the time efficient Asymmetric PC-MRI sequence (B).

CHAPTER 7

CONVEX GRADIENT DESIGN FOR PC-MRI

Conventional gradient waveform design in PC-MRI involves the use of triangular or trapezoidal waveforms which do not optimally use the available gradient hardware. Instead, these waveforms limit the sequence design to $G_{Max}/\sqrt{3}$ and $SR_{Max}/\sqrt{3}$ (where G_{Max} is the maximum gradient amplitude and SR_{Max} is the maximum gradient slew rate) to ensure the sequence performs within the hardware limitations for any given double oblique slice orientation. These limits are only approached during a few instances throughout the sequence, which limits sequence efficiency. In this chapter, an evaluation of convex gradient optimization (CVX) in PC-MRI sequences is conducted in an effort to provide increased spatiotemporal resolution and improved accuracy (Specific Aim #4). We ***hypothesize*** that the use of convex gradient optimization for all gradients within the PC-MRI pulse sequence will lead to more accurate measurements of blood flow and velocity through the reduction of chemical shift-induced phase errors and increased sequence efficiency, which can provide either higher spatial or higher temporal resolution.

INTRODUCTION

Phase contrast MRI (PC-MRI) is a non-invasive imaging technique, which is predominately used clinically to measure 2D through-plane blood velocity [cm/s] and derived measures like peak velocity [cm/s], flow rates [mL/s], and flow [mL]. PC-MRI flow measurements can guide clinical decision-making in congenital heart disease (2,7,67) but current clinical confidence in PC-MRI is relatively modest as a consequence of the frequent occurrence of blood flow and velocity results that contradict other clinical observations or are themselves internally inconsistent. Decades of research have helped mitigate numerous sources of PC-MRI measurement error that arise from eddy currents (29), Maxwell terms (24), gradient field distortions (23), and off-resonance (34). Nevertheless, chemical shift induced phase errors (57) and spatiotemporal undersampling remaining critical sources of error in PC-MRI for which a cogent error mitigation strategy is needed.

As a consequence of chemical shift induced phase errors and suboptimal spatiotemporal resolution, an individual patient’s PC-MRI measurements may demonstrate poor intra-subject agreement. For example, blood flow measured in the main pulmonary (PA) should equal the sum of blood flow measured in the right and left branch pulmonary arteries (RPA and LPA), but they can differ by >10mL (15%). An erroneous +5mL to the RPA and -5mL to the LPA makes a normal 60:40 flow split appear to be 2:1 (25), which is an accepted criteria that triggers clinical concern (2). However, if an abnormal flow split is not expected based on other clinical data, this raises concern for all the subject’s measurements; calls into question the reliability of the technique; confounds clinical decision-making; and may lead to follow-up exams, which incur greater downstream costs.

Chemical shift induced phase errors arise in PC-MRI (57) because the complex signal for perivascular fat chemically shifts across the vessel wall and corrupts the complex blood signal. This error is worse at 3T, does not subtract in phase difference processing, and is present in both conventional flow compensated and flow encoded (FCFE) and bi-polar PC-MRI sequences. This error, however, can be mitigated by using an in-phase TE (TE_{IN}) and a high receiver bandwidth (57). The use of the minimum available TE_{IN} is preferred, but conventional PC-MRI sequences at 3T cannot achieve this short TE ($TE_{IN,MIN} \approx 2.46$ms at 3T) over a range of clinically relevant velocity encoding strengths (VENCs) (68) because of inefficient gradient waveform design. Hence, existing sequences can only reduce chemical shift induced errors by using the next longer TE_{IN}, which is longer than TE_{MIN} and compromises sequence efficiency.

Spatiotemporal undersampling errors arise because suboptimal temporal resolution acts as a low-pass filter on a vessel's temporal velocity waveform and leads to an underestimation of peak velocity and total flow (69,70); and suboptimal spatial resolution compromises measurement accuracy due to partial-volume effects (71,72) and intravoxel spin dephasing (20,21). The spatiotemporal resolution of PC-MRI is more limited than other cardiac imaging techniques because of the need to acquire two echoes with different velocity sensitivities in order to correct background sources of off-resonance within an acceptable breath hold duration.

Improvements in spatiotemporal resolution for PC-MRI can be achieved in several ways including alternative k-space sampling trajectories (73-75), parallel imaging

(44,76), temporal data sharing schemes (65,77,78), partial Fourier imaging (79), compressed sensing (80), and k-t acceleration techniques (81). A judicious approach, which is also compatible with all of these methods, is to optimize each gradient waveform such that their duration is minimized, while maintaining the necessary zero and first order gradient moments required for flow imaging. Previously, Bernstein et al. (22) proposed an analytic solution for the construction of asymmetrically weighted velocity encoding gradients with trapezoidal and triangular gradient lobe shapes to provide a minimum TE PC-MRI sequence. Bolster et al. (82) presented an algorithm to implement three-axis flow-compensation in PC-MRI, which minimized sequence dead time through the construction of trapezoidal and triangular gradient lobe shapes that utilized the full capabilities of the gradient hardware for any oblique slice orientation. Atalar et al. (83) first introduced hardware-optimized trapezoidal gradient lobes and Derbyshire et al. (84) later developed hardware optimized gradients for the slice, phase, and read axes within the physical coordinate system for any oblique slice orientation. While each of these techniques provided reductions in TE/TR due to more efficient gradient construction, their efficiency is limited due to the required construction of trapezoidal and triangular gradient lobe shapes. This design approach cannot, in general, make optimal use of the available gradient hardware. Most recently, Hargreaves et al. (85) have shown that convex gradient optimization (CVX) can be used to minimize gradient waveform durations subject to both gradient hardware and pulse sequence constraints, including the desired gradient moments. This design approach is capable of producing arbitrarily shaped gradient waveforms that cannot be designed analytically.

Herein we propose, implement, and evaluate a time efficient (hardware optimized) chemical shift insensitive 2D through-plane PC-MRI sequence that uses an asymmetric velocity encoding strategy in combination with convex gradient optimization to produce simultaneously the minimum duration gradients for all axes. This sequence mitigates both chemical shift induced phases errors and spatiotemporal undersampling errors, thereby increasing the accuracy of cardiovascular blood flow and velocity measurements.

THEORY

The design target for a time efficient PC-MRI sequence is to minimize gradient waveform durations while staying within both sequence and hardware constraints. Sequence constraints arise due to the choice of RF pulse duration, slice thickness, field of view (FOV), bandwidth, matrix size, and the required gradient moments for velocity encoding. Additionally, hardware constraints limit the maximum available gradient amplitude, $G_{Max,}$ and slew rate, SR_{Max}. For a time efficient PC-MRI pulse sequence, two separate CVX optimizations are conducted. First, two slice select gradients (one for each velocity encoding acquisition), a flow compensated readout gradient, and a phase encoding gradient are optimized, simultaneously, for the interval between RF transmission and data acquisition (Interval 1 in Fig. 36b,c). Second, a spoiler gradient, a readout gradient ramp down, and a phase encode rewinder gradient are optimized, simultaneously, for the interval between the end of data acquisition and the end of the TR (Interval 2 in Fig. 36b,c). What follows is a description of the velocity encoding, pulse sequence, and hardware constraints used for the CVX optimization.

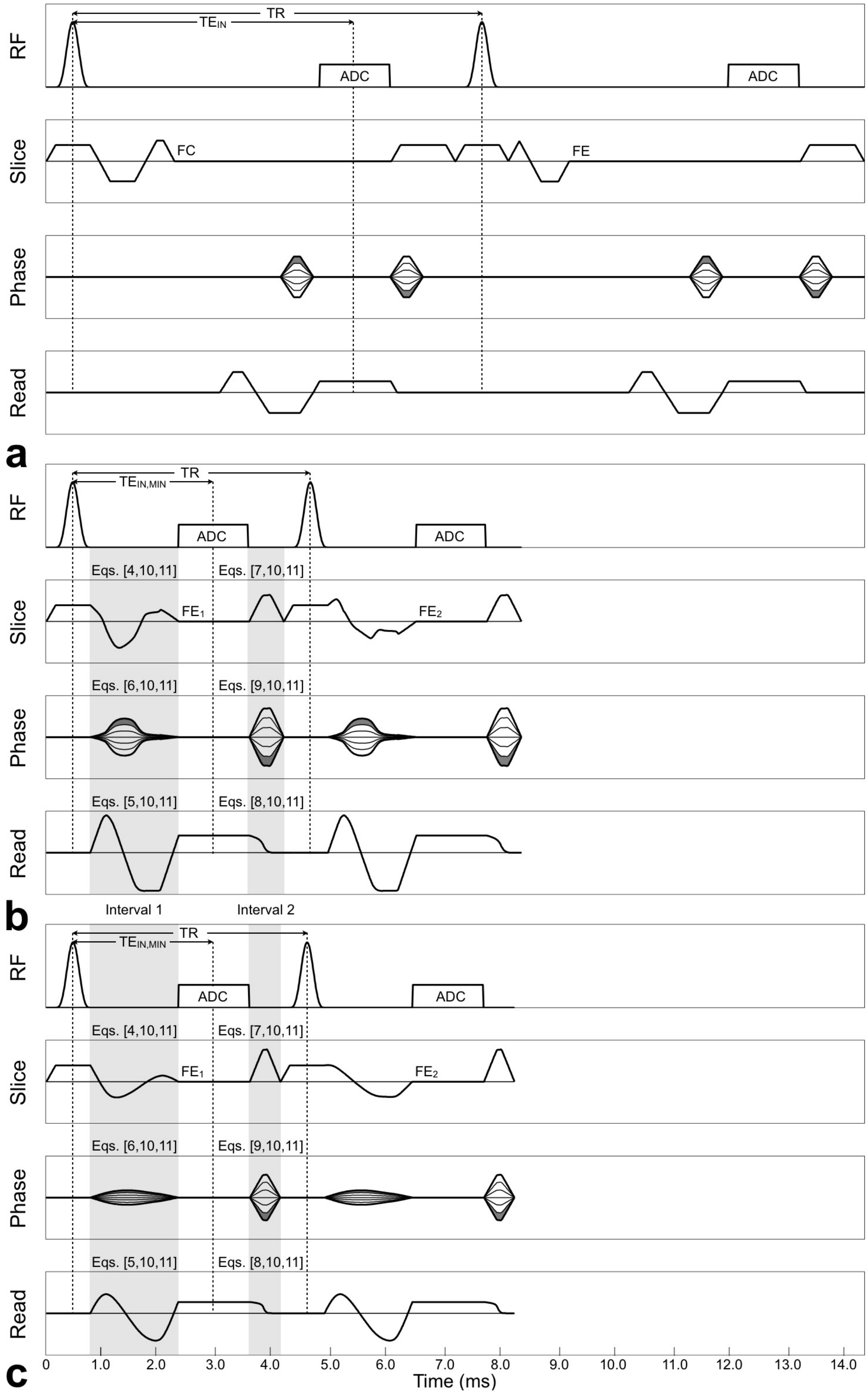
a
RF
TR
TE$_{IN}$
ADC
ADC
Slice
FC
FE
Phase
Read
b
RF
TR
TE$_{IN,MIN}$
ADC
ADC
Eqs. [4,10,11]
Eqs. [7,10,11]
Slice
FE$_1$
FE$_2$
Eqs. [6,10,11]
Eqs. [9,10,11]
Phase
Eqs. [5,10,11]
Eqs. [8,10,11]
Read
Interval 1
Interval 2
c
RF
TR
TE$_{IN,MIN}$
ADC
ADC
Eqs. [4,10,11]
Eqs. [7,10,11]
Slice
FE$_1$
FE$_2$
Eqs. [6,10,11]
Eqs. [9,10,11]
Phase
Eqs. [5,10,11]
Eqs. [8,10,11]
Read
0
1.0
2.0
3.0
4.0
5.0
6.0
7.0
8.0
9.0
10.0
11.0
12.0
13.0
14.0
Time (ms)

Figure 36. Pulse sequence diagrams for 2D through-plane chemical shift mitigated PC-MRI sequences at HBW (814Hz/px) and an in-phase TE (TE_{IN}): (a) conventional flow compensated and flow encoded (FCFE) velocity encoded sequence (TE_{IN}=4.92ms, 1.8mm×1.8mm spatial resolution, 55.9ms temporal resolution); (b) convex gradient optimized (CVX) velocity encoded sequence optimized for high spatial resolution ($TE_{IN,MIN}$=2.46ms, 1.2mm×1.2mm spatial resolution, 56.1ms temporal resolution); and (c) CVX optimized for high temporal resolution ($TE_{IN,MIN}$=2.46ms, 1.8mm×1.8mm spatial resolution, 31.6ms temporal resolution). The equations used to constrain the CVX optimization are labeled for each axis. Two separate CVX optimizations are conducted for each sequence as indicated by the gray regions within the pulse sequence diagrams. The two slice select gradients, the flow compensated readout gradient, and the phase encoding gradient are optimized during the time between RF transmission and data acquisition (Interval 1). The spoiler, readout ramp down, and phase encode rewinder gradients are optimized during the time between the end of data acquisition and the end of the TR (Interval 2).

Velocity Encoding Constraints

For a typical 2D through-plane PC-MRI experiment, two velocity-encoded acquisitions with different first moments are needed to encode flow along the slice select direction. All velocity encoding schemes use a bipolar encoding gradient after the slice select gradient. The combination of the slice select and velocity encoding gradients results in a nulled zeroth gradient moment (M_0) for each encoding step (i.e. $M_{0,1}=M_{0,2}=0$), which refocuses the position-related phase at TE. The velocity encoding scheme must also have a net difference in first moments (M_1) that yields a velocity dependent phase ($\Delta M_1 = M_{1,1} - M_{1,2} \neq 0$) at TE. The phase difference ($\Delta\phi$) mitigates the dependence on non-velocity background phase and is proportional to the velocity (v_z) of flowing blood according to:

$$\Delta\phi = \gamma v_z \Delta M_1. \qquad [1]$$

The applied velocity encoding gradients have a maximum velocity encoding strength (VENC), which is defined as the velocity that produces a phase shift of π radians, or VENC = $\pi(\gamma\,|\Delta M_1|\,)^{-1}$.

The target ΔM_1 is achieved by acquiring two velocity encoded acquisitions of the form:

$$M_{1,1} = \alpha \Delta M_1 \qquad [2a]$$

$$M_{1,2} = (\alpha - 1)\,\Delta M_1, \qquad [2b]$$

where α scales the first moment distribution and depends on the selected velocity encoding strategy. Conventionally, velocity encoding is achieved by using either a pair of equal and opposite bipolar flow encoding gradients (α=0.5) (14,15) or a set of flow compensated and flow encoded gradients (FCFE, α=0) (16,17). This requirement is inefficient and typically leads to velocity encoding gradient waveforms that are unequal in duration. Hence, the minimum achievable TE/TR is limited by the velocity encoding acquisition with the longest duration. Bernstein et al. (22) used velocity encoding gradients without constraining α. The only requirement was that the encoding acquisitions produced the required ΔM_1, which results in shorter velocity encoding gradient waveforms and reductions in TE/TR. We refer to this velocity encoding strategy as asymmetric velocity encoding. Herein, we extend this concept and make the gradient waveforms more efficient by starting the velocity encoding gradients immediately after the slice select gradient plateau, without ramping down. Our CVX PC-MRI sequence is optimized to take full advantage of asymmetric velocity encoding (flexible α):

$$M_{0,slice,n} = 0 \qquad [3a]$$

$$M_{1,slice,1} - M_{1,slice,2} = \frac{\pi}{\gamma VENC}. \qquad [3b]$$

where n is the velocity encoding step (i.e. 1 or 2).

Pulse Sequence Constraints

The specific pulse sequence protocol (e.g. RF pulse duration, slice thickness, FOV, bandwidth, and matrix size) defines the end time and gradient amplitude of the slice select gradient and the gradient amplitude and duration of the readout gradient. The velocity encoding gradient for each encoding step is constructed to begin at the end of the RF pulse and end at the start of data acquisition (Interval 1 in Fig. 36b,c) with the following constraints:

$$G_{slice,n,i} = \frac{2\pi\Delta f}{\gamma\Delta z}, \qquad [4a]$$

$$G_{slice,n,f} = 0, \qquad [4b]$$

where Δf is the bandwidth of the RF pulse [Hz], γ is the gyromagnetic ratio [MHz/T], and Δz is the slice thickness [m]. Therein, *i* and *f* indicate the initial and final gradient amplitudes.

The flow compensated readout gradient is constructed with the following constraints:

$$M_{read,0}\left(TE\right) = 0 \qquad [5a]$$

$$M_{read,1}\left(TE\right) = 0 \qquad [5b]$$

$$G_{read,i} = 0 \qquad [5c]$$

$$G_{read,f} = \frac{4\pi BW}{\gamma FOV_x}, \qquad [5d]$$

where $G_{read,f}$ is the final gradient amplitude for the CVX optimized flow compensated readout [mT/m], which is also the readout gradient plateau amplitude, BW is the receiver bandwidth [Hz], and FOV_x is the field-of-view in the readout direction [m].

The phase encode gradient is optimized only for the phase encoding step that requires the largest gradient area, which is equivalently either the largest positive or largest negative phase encode step for Cartesian k-space acquisitions. It is computationally expensive to optimize the phase encoding gradient for each phase encoding step, and doing so would result in different TE/TR values, which could introduce signal fluctuations and would confound cardiac segmented acquisitions. Hence, the phase encoding gradient is designed such that:

$$M_{phase,0} = \frac{\pi \left(N_y - 1\right)}{\gamma FOV_y} \qquad [6a]$$

$$G_{phase,i} = 0 \qquad [6b]$$

$$G_{phase,f} = 0, \qquad [6c]$$

where N_y is the number of phase encoding steps to be acquired and FOV_y is the field-of-view in the phase encode direction.

Additional constraints are needed for the second interval of CVX optimization (Interval 2 in Fig. 36b,c) for the slice, phase, and read gradients played between the readout gradient plateau and the end of the TR. The spoiler gradient is constructed with the following constraints:

$$M_{spoil,0} = \frac{\varphi}{\gamma \Delta Z} \qquad [7a]$$

$$G_{spoil,i} = 0 \qquad [7b]$$

$$G_{spoil,f} = 0, \qquad [7c]$$

where φ [rad] is the required phase dispersion of the applied spoiler gradient. The ramp down of the readout gradient is constructed with the following constraints:

$$G_{read,i} = \frac{4\pi BW}{\gamma FOV_x} \qquad [8a]$$

$$G_{read,f} = 0. \qquad [8b]$$

The phase encoding rewinder gradient is designed with the following constraints:

$$M_{rewind,0} = -\frac{\pi\,(N_y - 1)}{\gamma FOV_y} \qquad [9a]$$

$$G_{rewind,i} = 0 \qquad [9b]$$

$$G_{rewind,f} = 0. \qquad [9c]$$

Gradient Hardware Constraints

In addition to velocity encoding and pulse sequence constraints, the gradient hardware limits G_{Max} and SR_{Max}. The conventional design of PC-MRI gradients does not optimally use the available gradient hardware for all time points, but rather achieves the maximum only for very brief periods. To accommodate double-oblique scan plane orientations, the slice, read, and phase directions are all individually designed with maximum gradient amplitude and slew rate specifications that are reduced by as much a √3 to avoid overranging the physical gradients when the gradient waveforms are rotated into the image plane coordinate system. The result, however, is that the G_{Max} and SR_{Max} hardware limits may only be reached during a few instances for particular orientations, which unnecessarily limits sequence efficiency. This arises as a consequence of a design strategy that is a holdover from analytic solutions and hand-coded gradient waveform designs that use simple trapezoidal and triangular gradient lobe shapes. PC-MRI sequences can be made significantly more time efficient by optimizing the use of the available gradient hardware to jointly design velocity encoding phase-encoding, pre-winder, rewinder, and spoiler gradients.

For the CVX PC-MRI sequence, the optimization of the gradients for each time point between the slice select and readout gradient plateaus, the gradient amplitudes are constrained according to:

$$\sqrt{max\left(G_{slice,n}^2\right)+G_{read}^2+G_{phase}^2} \leq G_{Max} \qquad [10a]$$

$$G_{slice,n} \leq G_{Max} \qquad [10b]$$

$$G_{read} \leq G_{Max} \qquad [10c]$$

$$G_{phase} \leq G_{Max}, \qquad [10d]$$

where $G_{slice,n}$ is the maximum gradient amplitudes for the pair of velocity encoding gradients and G_{phase} and G_{read} are the maximum gradient amplitudes for the flow compensated readout gradient and the phase encode gradient, respectively. This constraint ensures that for any slice orientation the maximum gradient amplitude used on any given axes will always be less than G_{Max}. Similarly, the slew rates are constrained by replacing G_{Max} with SR_{Max} throughout Eq. [10].

For the CVX optimization of the gradients between the readout gradient plateau and the end of the TR, the gradient amplitudes are constrained for each time point according to:

$$\sqrt{G_{spoil}^2+G_{read}^2+G_{rewind}^2} \leq G_{Max} \qquad [11a]$$

$$G_{spoil} \leq G_{Max} \qquad [11b]$$

$$G_{read} \leq G_{Max} \qquad [11c]$$

$$G_{rewind} \leq G_{Max}, \qquad [11d]$$

where G_{spoil}, G_{read}, and G_{rewind} represent the maximum gradient amplitudes for the spoiler gradient, the ramp down of the readout gradient, and the phase encode rewinder gradient, respectively. Similarly, the slew rates are constrained by replacing G_{Max} with SR_{Max} throughout Eq. [11].

Minimum-Time Solution

As previously described by Hargreaves et al. (38), the minimum-time solution for any constrained gradient waveform involves finding the minimum gradient duration, T ($T=m\tau$, where m is an integer and $\tau=10\mu s$, which is the gradient raster time), that produces a solution to the constrained problem. Convex optimization algorithms use successive binary-searches to divide the interval containing T on each function call. An initial estimate of the upper and lower bounds, T_u and T_l, are defined to start the optimization. For the $TE_{IN,MIN}$ protocols used in this study, T_u and T_l were set to 1.54ms, based on the target of $TE_{IN,MIN}$=2.46ms minus half the slice select (0.3ms) and readout (0.62ms) gradient plateau durations. For TE_{MIN} protocols, T_u can be determined analytically using conventional trapezoid and triangle gradient waveforms and an analytic solution similar to that proposed by Bernstein et al (22) (Appendix A). T_l is then assigned as $T_l=0.8T_u$. The value of T is set to T_u to determine whether the aforementioned constraints are satisfied for all axes, simultaneously. Once a feasible solution exists within the interval of T_u and T_l, T is set to $0.5(T_u+T_l)$, tested based on the assigned constraints, and then repeated until the minimum feasible T is determined.

METHODS

Convex Gradient Optimization

The improved time efficiency of the CVX PC-MRI pulse sequence allows the use of $TE_{IN,MIN}$=2.46ms at 3T. $TE_{IN,MIN}$ cannot be achieved with the conventional FCFE PC-

MRI sequence, which uses the next available in-phase TE: TE_{IN}=4.92ms. In addition, CVX can be used to either reduce scan time or increase spatiotemporal resolution for a fixed breath hold time compared to conventional FCFE. Therefore, two CVX chemical shift insensitive PC-MRI protocols were compared to a conventional chemical shift insensitive FCFE PC-MRI sequence.

Table 8 shows the gradient hardware and pulse sequence constraints used for the CVX sequences. Table 9 shows the PC-MRI sequence parameters used for the chemical shift insensitive FCFE sequence and the chemical shift insensitive CVX sequences with optimized spatial and temporal resolution and Fig. 36 shows the corresponding pulse sequence diagrams. Based on our previous work involving the analysis of time efficient gradient spoiling in PC-MRI (86), the CVX sequences used 4π dephasing for the slice select spoiler gradient compared to FCFE, which uses 9π dephasing.

The CVX optimization was conducted offline using Matlab (The MathWorks, Natick, MA) and a freely available Matlab-based modeling system for disciplined convex optimization (87,88). The resulting CVX gradients for PC-MRI were then exported to a text file, which was read within the pulse sequence environment to construct the gradients. The Matlab scripts used for the CVX optimization are described in Appendix B.

Table 1. Gradient waveform parameters for FCFE and CVX PC-MRI.

	FCFE	CVX Spatial Resolution	CVX Temporal Resolution
Gradient hardware			
G_{Max} (mT/m)	23	38 [Eqs. 10,11]	38 [Eqs. 10,11]
SR_{Max} (T/m/s)	115	170 [Eqs. 10,11]	170 [Eqs. 10,11]
Velocity encoding			
G_i (mT/m)	0	15.66	15.66
G_f (mT/m)	0	0	0
$M_{0,1}$, $M_{0,2}$ (mT/m×ms)	0, 0	0, 0 [Eq. 4]	0, 0 [Eq. 4]
$M_{1,1}$, $M_{1,2}$ (mT/m×ms^2)	0, 7.83	1.55, 9.38 [Eq. 4]	2.09, 9.92 [Eq. 4]
Flow compensated readout			
G_i (mT/m)	0	0 [Eqs. 5,8]	0 [Eqs. 5,8]
G_f (mT/m)	0	16.45 [Eqs. 5,8]	10.79 [Eqs. 5,8]
M_0 (mT/m×ms)	0	0 [Eq. 5]	0 [Eq. 5]
M_1 (mT/m×ms^2)	0	0 [Eq. 5]	0 [Eq. 5]
Phase encode/rewinder			
G_i (mT/m)	0	0 [Eqs. 6,9]	0 [Eqs. 6,9]
G_f (mT/m)	0	0 [Eqs. 6,9]	0 [Eqs. 6,9]
M_0 (mT/m×ms)	±7.37	±10.27 [Eqs. 6,9]	±7.37 [Eqs. 6,9]
Spoiler			
G_i (mT/m)	0	0 [Eq. 7]	0 [Eq. 7]
G_f (mT/m)	0	0 [Eq. 7]	0 [Eq. 7]
M_0 (mT/m×ms)	27.86 (9π)	12.57 (4π) [Eq. 7]	12.57 (4π) [Eq. 7]
M_1 (mT/m×ms^2)	90.78	30.18	29.26

Table 2. PC-MRI parameters.

	FCFE	CVX Spatial Resolution	CVX Temporal Resolution
TE/TR (ms)	4.92/7.00	2.46/4.00	2.46/3.95
Temporal resolution (ms)	55.9	56.1	31.6
VENC (cm/s)	150	150	150
Parallel acceleration	rate-2 GRAPPA with 24 reference lines		
Flip angle (degrees)	30	30	30
Segments	4	7	4
FOV (mm)	340 × 255	340 × 255	340 × 255
Pixel number	192 × 144	288 × 216	192 × 144
Pixel size (mm)	1.8 × 1.8	1.2 × 1.2	1.8 × 1.8
Bandwidth (Hz/px)	814	827	814
Duration (heart beats)	23	20	23
Acquired cardiac phases †	13-18	13-18	23-32

† The number of acquired cardiac phases is heart rate dependent

PC-MR Imaging

All imaging was performed on a Siemens Trio 3T system (Siemens Medical Solutions, Erlangen, Germany) capable of 40mT/m maximum gradient amplitude and 200T/m/s maximum slew rate. The sequence was coded with a G_{Max}=38mT/m SR_{Max}=170T/m/s to avoid overanging the gradients and potential peripheral nerve stimulation effects. For all experiments, PC-MRI data were acquired using an anterior 6-element body matrix coil and a posterior 6-element spine matrix coil for signal reception. All imaging was performed with the imaging slice centered at isocenter, as previously recommended for the reduction of velocity offset errors (89).

Numerical Simulations of Spatiotemporal Sampling

The effect of spatiotemporal resolution on PC-MRI total flow and peak velocity measurements was evaluated using a numerical simulation. A 400ms half sine wave temporal velocity waveform was modeled with 1ms temporal sampling. The peak velocity was set to 150cm/s. A 20 mm simulated vessel was constructed with 0.1mm spatial resolution and a laminar flow profile across the vessel. The velocity profile was sampled with a range of temporal resolutions (30ms to 100ms in increments of 10ms) and temporal offsets (0ms to the simulated temporal resolution in increments of 10ms) as well as a range of spatial resolutions (1mm×1mm to 2.2mm×2.2mm in increments of 0.1mm×0.1mm) and spatial offsets (0mm×0mm to the simulated spatial resolution in increments of 0.1mm×0.1mm). Note that this simulation was used to analyze the effects of partial-volume and temporal filtering through changes in spatial and temporal sampling and did not take into account the MRI signal properties such as flip angle, TE/TR, T_1/T_2, or noise.

Flow Phantom Experiments

Validation of the CVX sequence was performed by comparing flow phantom measurements to the conventional FCFE sequence using identical scan parameters: TE/TR = 3.08/5.08ms, 320×221 matrix, 1.5mm×1.5mm×5mm acquisition voxel, 30° imaging flip angle, 801Hz/pixel receiver bandwidth, 4 views-per-segment (60), a total scan time of 21 heart beats, a temporal resolution of 40.6ms, 25 cardiac phases reconstructed during a simulated 1000ms RR-interval, retrospective ECG gating, rate-2

GRAPPA (44) parallel imaging with 24 reference lines, and VENC = 150cm/s. PC-MRI data were acquired in a sealed tube (20/1.0mm inner diameter/wall thickness) containing blood-mimicking fluid (40% glycerol, 60% water), which was circulated through the phantom by a CardioFlow 1000MR computer controlled displacement pump (Shelley Medical Imaging Technologies, Toronto, Ontario, Canada). The flow profile was programmed for two sine waves with peak velocities of 75 and 150cm/s. Measurements were repeated three times for each sequence at each flow rate. Additionally, flow phantom measurements were obtained using the FCFE and compared to the higher spatial and higher temporal resolution CVX sequences described in Fig. 36 and Tables 8-9. The flow profile, designed to match the numerical simulations, consisted of a 400ms half sine wave with a peak velocity of 150cm/s. Three measurements for each sequence were acquired.

Preclinical Evaluation in Normal Volunteers

A preclinical evaluation was performed to compare the measurement accuracy for our proposed CVX sequences compared to the conventional FCFE sequence using a chemical shift insensitive protocol (Fig. 36 and Tables 8-9). Our university's Institutional Review Board approved the study and informed consent was obtained for each subject prior to MRI scanning. Subjects were positioned head first in the supine position on the scanner bed and imaged using an anterior 6-element body matrix coil and a posterior 6-element spine matrix coil for signal reception. PC-MRI data was acquired in the ascending aorta, (aAo), main pulmonary artery (PA), and right/left pulmonary arteries (RPA/LPA) of ten (N=10) normal volunteers (3 female, 7 male; age 26.7±3.6 years) with no previous history of cardiovascular disease.

The imaging plane for aAo flow was located in the ascending aorta distal to the aortic valve and coronary ostia. The imaging plane for flow in the PA was located downstream from the pulmonary valve and proximal to the first bifurcation. The imaging planes for the RPA and LPA were located ~1cm distal to the pulmonary bifurcation. All imaging planes were prescribed on bSSFP cine images during end-systole using end-expiratory breath holds.

Eddy Current Correction

Eddy current induced velocity offsets were measured by imaging a stationary viscous gel phantom (97.85% water, 2% hydroxyethyl cellulose, 0.1% copper sulfate, and 0.05% sodium azide) placed at isocenter with identical slice prescriptions and imaging parameters as the PC-MRI scans (29). Stationary phantom correction was conducted within one week of all PC-MRI experiments to avoid temporal drift of eddy current-induced phase shifts (90).

Image Processing

Data were processed offline using Matlab and a DICOM viewing tool (Osirix, www.osirix-viewer.com). For quantitative flow assessment at each vessel territory, the stationary eddy current correction phantom images were subtracted from the volunteer PC-MRI phase images on a pixel-by-pixel basis. A region-of-interest (ROI) was drawn in Osirix around the contours of each vessel boundary as indicated in the magnitude images. The resulting ROIs were then imported to the eddy current corrected PC-MRI phase images, which were then exported from Osirix to Matlab for quantitative velocity and flow analysis. Measurements of total flow were computed by scaling the mean ROI signal intensity (velocity related phase shift) by VENC/π (cm/s). The resulting mean ROI velocities were then multiplied by the area of the ROI (cm^2) to calculate the flow rate (mL/s) and finally integrated over the cardiac cycle to yield the total flow results (mL). Measurements of peak velocity were computed by scaling the ROI signal by VENC/π (cm/s) in the cardiac frame with the maximum signal intensity. Measurements of pulmonary to systemic blood flow ratios (Qp/Qs) were computed by dividing measurements of PA total flow by aAo total flow. Measurements of eddy current-induced velocity offsets were computed by scaling the mean ROI signal intensity in each cardiac frame by VENC/π (cm/s) and then averaging across all cardiac frames.

Data Analysis

All statistical analysis was performed in Matlab. Bland-Altman (48) analysis was used to compare the measurement bias (mean difference between the measurements) and limits of agreement (95% confidence intervals, lower and upper 95%-CI) between measurements made with FCFE and CVX in addition to comparisons of repeated with FCFE vs. FCFE and CVX vs. CVX. The mean and standard deviation of total flow, peak velocity, and eddy current-induced velocity offsets were calculated for each flow territory across the population of volunteers for FCFE and CVX. Additionally, the mean and standard deviation of pulmonary to systemic blood flow ratios (Qp/Qs) were compared for FCFE and CVX. A paired t-test with Holm-Sidak post hoc correction was used to measure the statistical significance of measurements obtained using FCFE and CVX at the 95% significance level (P<0.05). Lastly, an analysis of sequence efficiency, defined as the ratio of the readout duration and the TR (91,92) was computed for FCFE and CVX.

RESULTS

Numerical Simulations of Spatiotemporal Sampling

Figure 37 shows numerical simulations of the measured total flow and peak velocity for a range of spatial and temporal resolution combinations. The results indicate that the parameters used in the FCFE protocol can lead to a 14.2% error in total flow and a 6.7% error in peak velocity. CVX with high spatial resolution leads to a 10.2% error in total flow and a 6.2% error in peak velocity. CVX with high temporal resolution leads to a 10.5% error in total flow and a 5.9% error in peak velocity.

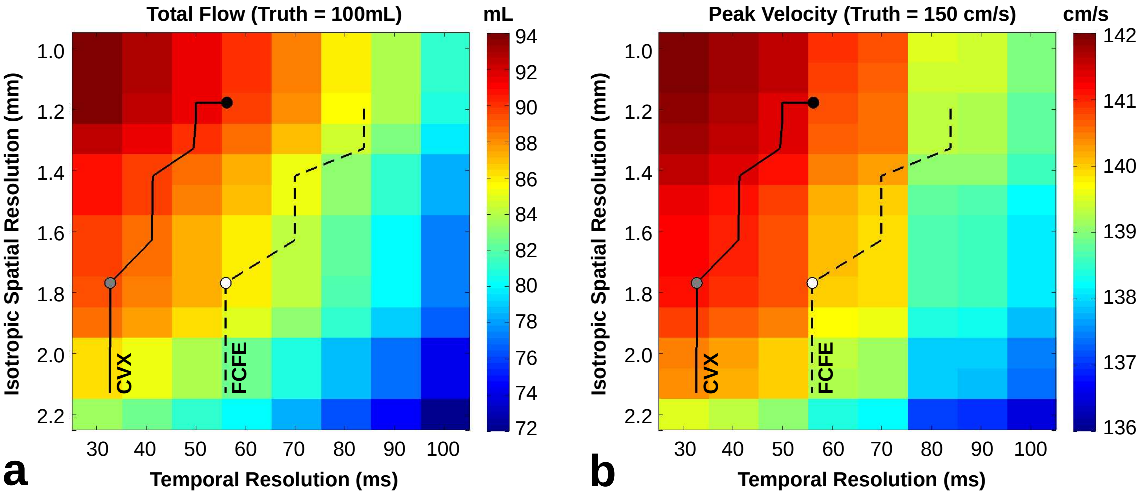

Figure 37. Numerical simulations of spatiotemporal sampling showing (a) the measured total flow and (b) peak velocity for different combinations of spatial and temporal resolution. Overlaid on top of the simulations are FCFE (dashed line) and CVX (solid line) contours for chemical shift insensitive protocols with 20-23 heart beat scan durations. The PC-MRI sequences described in Table 9 and Figure 36 are denoted by the white (FCFE), black (CVX with high spatial resolution), and gray (CVX with high temporal resolution) circles. The FCFE protocol leads to a 14.2% error in total flow and a 6.7% error in peak velocity. The CVX protocol optimized for high spatial resolution leads to a 10.2% error in total flow and a 6.2% error in peak velocity. The CVX protocol optimized for high temporal resolution leads to a 10.5% error in total flow and a 5.9% error in peak velocity. The simulated total flow and peak velocity was 100 mL and 150 cm/s, respectively.

Flow Phantom Experiments

The Bland-Altman plots and statistics (Fig. 38) show a low measurement bias and 95%-CI range (bias [lower 95%-CI, upper 95%-CI,]) 0.28cm/s [-7.14cm/s, 7.69cm/s] when comparing FCFE and CVX PC-MRI with matched sequence parameters. For reference, comparisons of repeated FCFE experiments had a measurement bias of -0.40cm/s [-4.71cm/s, 3.90cm/s] and CVX experiments had a measurement bias of -0.65cm/s [-4.58cm/s, 3.27cm/s]. Flow phantom measurements of total flow were 85.6±2.3 mL for FCFE, 91.5±1.6 mL for the CVX with high spatial resolution, and 90.9±1.4 mL for CVX with high temporal resolution. Flow phantom measurements of peak velocity were 132.3±2.2 cm/s for FCFE, 135.3±1.6 cm/s for CVX with high spatial resolution, and 137.1±1.7 cm/s for CVX with high temporal resolution.

Compared to the programmed values, FCFE leads to a 14.4% error in total flow and an 11.8% error in peak velocity. CVX with high spatial resolution leads to an 8.5% error in total flow and a 9.8% error in peak velocity. CVX with high temporal resolution leads to a 9.1% error in total flow and an 8.6% error in peak velocity.

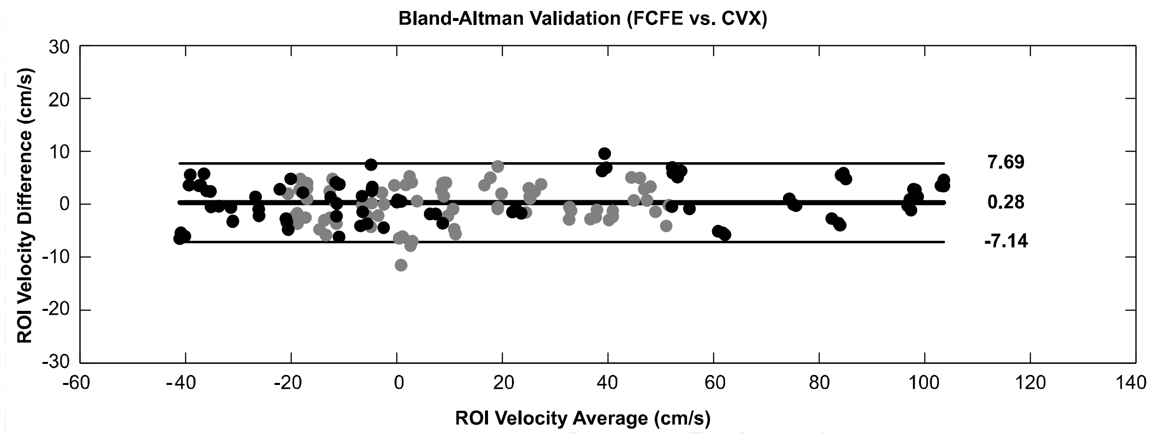

Figure 38. Bland-Altman analysis of the measured mean velocity within each cardiac phase from the flow phantom experiments measured using FCFE and CVX, each with three repeated measures. The solid lines represent the measurement bias while the dashed lines represent the limits of agreement (95%-CIs). The gray and black data points represent data from the 150 mL/s and 300 mL/s peak flow rate measurements, respectively. The measurement bias (0.28cm/s) and 95%-CI range (-7.14cm/s, 7.69cm/s) are low, indicating that the measured velocity is the same between the FCFE and CVX sequences for identical PC-MRI protocol parameters.

Preclinical Evaluation in Normal Volunteers

Measurements of total flow and peak velocity are listed in Table 10 and shown in Fig. 39. Figure 39 illustrates that the measurements of total flow and peak velocity were higher for both CVX protocols compared to FCFE, in every volunteer and every region. The measured total flow and peak velocity for FCFE vs. CVX with high spatial resolution and FCFE vs. CVX with high temporal resolution were significantly different ($P<0.05$). Across all volunteers and vessels, CVX with high spatial resolution resulted in an 8.1% and 3.8% increase in the measured total flow and peak velocity, respectively, compared to FCFE. Similarly, CVX with high temporal resolution increased these same measures by 5.1% and 10.5%. The measured Qp/Qs ratios for FCFE vs. CVX with high spatial resolution (1.03±0.02 vs. 1.04±0.01) and FCFE vs. CVX with high temporal resolution (1.03±0.02 vs. 1.04±0.01) were not significantly different ($P>0.05$). Eddy current-induced velocity offsets for FCFE, CVX with high spatial resolution, and CVX with high temporal resolution were 0.46±0.33 cm/s, 0.80±0.43 cm/s, and 1.01±0.55 cm/s, respectively. The calculated sequence efficiencies for FCFE, CVX with high spatial resolution, and CVX with high temporal resolution were 17.7%, 30.5%, and 31.4%, respectively. Figure 40 shows representative PC-MRI images and the measured peak velocity profiles from a single volunteer the FCFE and CVX sequences.

Table 3. In vivo PC-MRI measures of total flow and peak velocity.

	FCFE	CVX Spatial Resolution	CVX Temporal Resolution
Total Flow (mL)			
aAo	89.0±18.2	95.9±19.4[†]	93.5±17.9[†]
PA	92.6±18.5	100.1±20.1[†]	97.2±18.0[†,‡]
RPA	48.1±9.5	52.5±9.9[†]	50.9±9.5[†,‡]
LPA	44.3±8.7	47.7±10.2[†]	46.4±9.0[†]
Peak Velocity (cm/s)			
aAo	117.2±17.2	121.6±15.3[†]	127.3±15.8[†,‡]
PA	87.0±11.8	90.0±13.5[†]	95.4±15.4[†,‡]
RPA	93.8±15.9	97.1±16.8[†]	104.7±21.7[†,‡]
LPA	95.3±18.0	99.7±19.8[†]	107.2±19.9[†,‡]

Data are expressed as mean±standard deviation in mL (total flow) and cm/s (peak velocity).

[†] P<0.05 shows a statistical significant difference with FCFE.

[‡] P<0.05 shows a statistical significant difference with CVX Spatial Resolution.

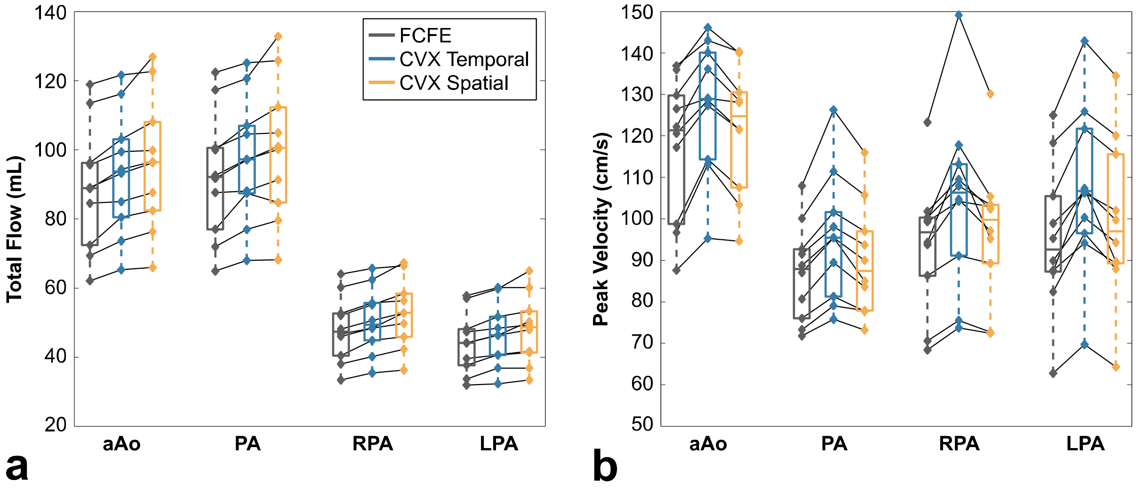

Figure 39. (a) Total flow and (b) peak velocity measurements obtained using FCFE (gray), CVX with high spatial resolution (blue), and CVX with high temporal resolution (yellow). Data from each volunteer (N=10) are connected to show that both CVX protocols lead to increased measures of total flow and peak velocity compared to FCFE for every volunteer and every region. All data are eddy current corrected. The box plots show the median and 25th and 75th percentiles and the error bars show the 95% confidence intervals.

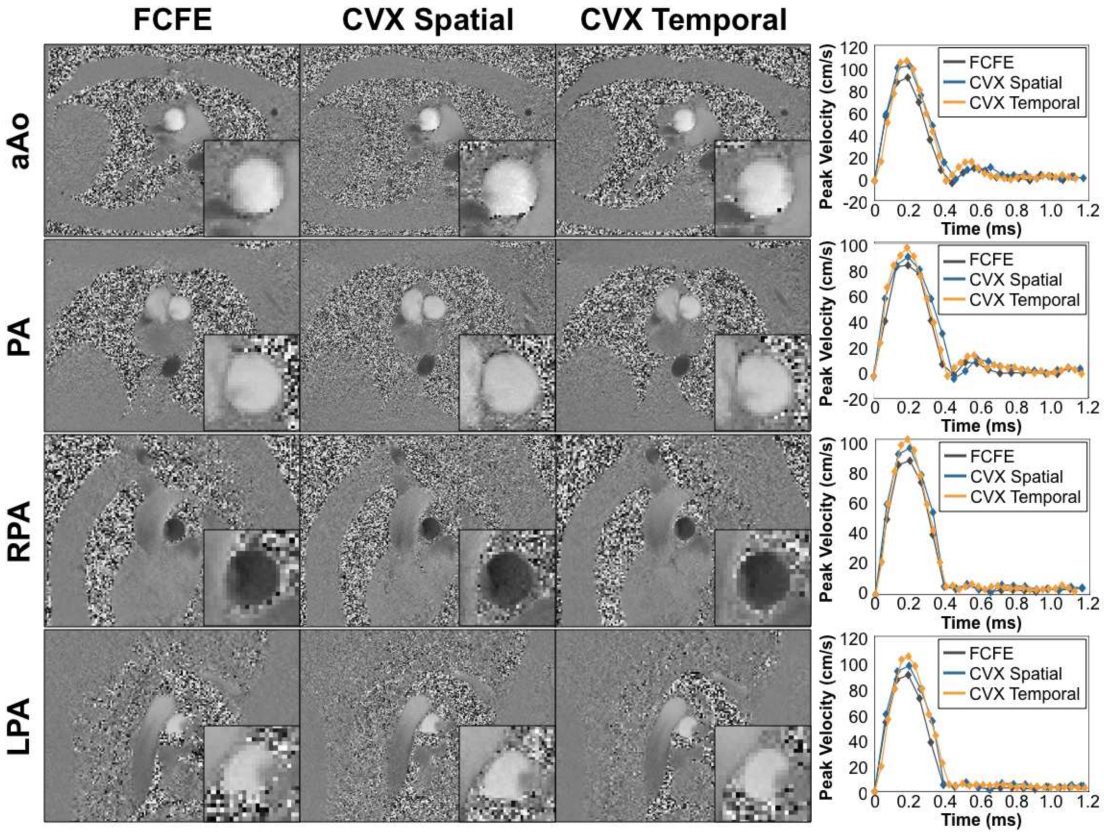

Figure 40. Representative PC-MRI images and measured peak velocity profiles within the ascending aorta (aAo), main pulmonary artery (PA), and right and left branch pulmonary arteries (RPA and LPA) from a single volunteer for the FCFE and CVX sequences.

DISCUSSION

CVX is used to construct a chemical shift insensitive, 2D through-plane velocity encoded PC-MRI sequence with minimum duration gradients for all axes given pulse sequence and hardware constraints. CVX PC-MRI provides more accurate measurements of blood flow and peak velocity due to increased sequence efficiency, which affords time efficient chemical shift insensitivity in addition to increased spatial or temporal resolution.

The low measurement bias and narrow 95%-CIs of the Bland-Altman results indicate that flow phantom velocity measurements acquired with CVX PC-MRI are in excellent agreement with conventional FCFE PC-MRI for identical scan parameters. Furthermore, good agreement is observed between flow phantom measurements and the numerical simulations of spatiotemporal sampling. Both the flow phantom experiments and numerical simulations indicate that CVX PC-MRI leads to an increase in the measured total flow and peak velocity that is more consistent with the expected values and hence more accurate, likely due to less low-pass spatiotemporal filtering.

The preclinical evaluation of CVX PC-MRI in normal volunteers resulted in higher measurements of total flow and peak velocity compared to FCFE, which we infer are more accurate from our simulation and flow phantom results. Additionally, in the absence of shunts or regurgitant flow (neither of which is expected within our normal volunteer population), we expect that the measured Qp/Qs ratios be close to 1.05 (accounting for flow loss into the coronary arteries at the level of aAo (64)). Qp/Qs ratios were close to the expected value of 1.05 and no statistical difference was observed between measures of Qp/Qs between FCFE and CVX. This is due to the fact that FCFE underestimates flow in the aAo and the PA by approximately the same amount. This indicates that blood flow measured with FCFE shows good relative flow agreement when chemical shift effects are mitigated, but lacks absolute flow agreement. CVX PC-MRI therefore represents a more accurate sequence for quantifying blood flow and velocity due to increased spatiotemporal sampling.

Measurements of eddy current-induced velocity offsets for CVX with high spatial and temporal resolution were greater than FCFE. This is likely due to the fact that the CVX sequences make better use of the available gradient hardware and uses higher gradient slew rates that may result in higher eddy current-induced velocity offsets. Additionally, dead time exists in the FCFE sequence (TE_{IN}>TE_{MIN}), which allows for eddy current fields to dissipate resulting in reduced eddy current-induced velocity offsets. FCFE was the only sequence that resulted in acceptable (<0.6 cm/s) eddy current-induced velocity offsets before correction (61), which indicates that to obtain the most accurate PC-MRI measurements using CVX, stationary phantom eddy current corrections should be performed.

In order to control for the effects of chemical shift-induced phase errors all PC-MRI sequences used a high receiver bandwidth and TE_{IN} (57). The reduced gradient durations in CVX PC-MRI allows the use of $TE_{IN,MIN}$=2.46ms at 3T. $TE_{IN,MIN}$ cannot be achieved with the conventional FCFE PC-MRI sequence, thus it is necessary to use the next available in-phase TE (TE_{IN}=4.92ms). This leads to a concomitant increase in TE and TR, which decreases signal-to-noise ratio (SNR) due to T_2* effects and reduces temporal resolution. While this derates the FCFE sequence, it also controls for a significant source of error.

For $TE_{IN,MIN}$ protocols, the CVX optimization for Interval 1 (Fig. 36b,c) takes <20s to arrive at a solution, whereas for TE_{MIN} protocols, for which the search interval $[T_L,T_U]$ is longer, the CVX optimization takes ≈60s. The CVX optimization for Interval 2 takes <18s to arrive at a solution.

In addition to providing more accurate measures of blood flow and peak velocity with either increased spatial or temporal resolution, CVX also offers nearly doubles the sequence efficiency compared to FCFE. This is primarily due to a more efficient use of the available gradient hardware and an asymmetric distribution of M_1, but also due to a reduction in the area of the applied slice select spoiler gradient.

CVX offers the highest sequence efficiency gains compared to FCFE when using low VENCs (≤50cm/s). Thus, CVX may prove especially useful for low VENC applications, such as measuring CSF flow or myocardial velocity mapping. The increased spatial resolution provided by CVX could be useful for high spatial resolution applications, such as measuring blood flow in the carotid and coronary arteries while the increased temporal resolution provided by CVX could be useful for measuring high-velocity turbulent jets associated with stenotic and regurgitant valvular disease. Furthermore, instead of increasing spatiotemporal resolution, CVX could be used to reduce scan time, which would be extremely useful for 4D flow applications. Preliminary estimates indicate 4D flow acquisition times could be reduced by ~33%.

Limitations

The PC-MRI sequences evaluated in this study were restricted to the use of TE_{IN} for reduction of chemical shift-induced phase errors. When chemical shift effects are not of a concern, the minimum available TE/TR can be further reduced for CVX resulting in higher sequence efficiency and the use of higher spatial or temporal resolution. Regardless of chemical shift-induced errors, CVX always provides the shortest TE/TR compared with FCFE, which can be used to increase spatiotemporal resolution or reduce breath hold time.

Currently, the CVX optimization is conducted offline using Matlab. This requires that the desired VENC, FOV, matrix size, receiver bandwidth, slice thickness, and RF pulse duration be known a priori. Furthermore, these sequence parameters cannot be altered during a scan, which currently limits the clinical utility of the sequence. In addition, based on Eqs. [10-11], the current optimization produces a time efficient solution that works for all slice orientations and does not exceed peripheral nerve simulation limits. However, further incremental improvements may be possible by considering slice-specific physical gradient hardware constraints. Both of the above mentioned limitations could be overcome by conducting the CVX optimization online. In addition, the use of C++ libraries rather than Matlab could reduce the time needed for optimization.

CONCLUSIONS

CVX PC-MRI increases sequence efficiency while reducing chemical shift-induced phase errors. This can be used to provide either higher spatial or higher temporal resolution than conventional chemical shift mitigated PC-MRI methods to provide more accurate measurements of blood flow and peak velocity.

CHAPTER 8

REGION-OF-INTEREST CONTOURING ERRORS

PC-MRI measurements require a region-of-interest (ROI) to be manually contoured to encompass the vessel lumen, but this process is subjective and prone to error. In this chapter, ROIs were systematically increased/decreased to evaluate the impact of overestimating and underestimating the ROI size on PC-MRI flow measurements (Specific Aim #5). We ***hypothesize*** that overestimating the ROI size will lead to higher accuracy compared to underestimating the ROI size and that these findings can be used as evidence based suggestions for ROI contouring to increase measurement accuracy in PC-MRI.

INTRODUCTION

Ongoing research efforts and established correction methods for many of the known errors in PC-MRI have helped mitigate the quantitative inaccuracies of the technique, but PC-MRI remains an underutilized clinical tool due to measurement unreliability. Nevertheless, PC-MRI holds tremendous promise given the need to non-invasively measure 2D through-plane blood flow in a wide range of clinical settings. Reduction of PC-MRI errors to clinically insignificant levels (<5% of total flow) is necessary if these measurements are to be made routinely accurate and absolutely quantitative. In this work, we aim to analyze the effects of variable ROI contouring on PC-MRI measurement errors in an effort to improve upon the quantitative accuracy of the technique.

PC-MRI images are comprised of pixels containing a measured phase that, in the absence of errors, is proportional to the velocity of moving tissue (e.g. flowing blood). To measure, for example, total forward flow or peak velocity, PC-MRI images require contouring a ROI to isolate the lumen of a blood vessel of interest. An accurately contoured ROI would perfectly contain the vessel lumen and exclude the vessel wall. The resulting ROI provides an accurate measurement of total forward flow, but this may not be easily achieved due to limited post-processing time and suboptimal spatial resolution. Limited post-processing time directly impacts the accuracy of the ROI boundary. Suboptimal spatial resolution leads to blurring at the vessel lumen/wall boundary (pixels in the vessel lumen partial volume with pixels in the vessel wall) and compounds the estimate of the blood velocity (71,72).

The expected gross measurement error arising from an incorrectly drawn ROI can be predicted from observation of the tissues nearest the vessel lumen/wall boundary. If an ROI is drawn too small, the measurement will exclude pixels near the vessel lumen and lead to underestimation of total forward flow (assuming the excluded flow is forward flow). If an ROI is drawn too large, the measurement will include erroneous pixels that will lead to an over- or underestimation of total forward flow, depending on the signal's phase within the erroneously included pixels. If an ROI drawn too large contains stationary tissue (e.g. vessel wall or perivascular fat that does not chemically shift into the vessel lumen) with a moderate or high signal intensity, then the erroneously included pixels are unlikely to contribute a total forward flow measurement error because the stationary tissue would have a phase (velocity) of zero in the absence of noise and other sources of error. If an ROI is drawn too large and contains moving tissue (e.g. myocardium or a pulsatile vessel wall), then the erroneously included pixels can lead to an over- (under-) estimation of total forward flow when the moving tissue's mean velocity is in the same (opposite) direction as the blood flow. If an ROI is drawn too large and contains low signal magnitude tissue (e.g. lung tissue), the erroneously included pixels would contribute an unpredictable total forward flow error.

The ***objective*** of this work was to systematically evaluate the impact of overestimating and underestimating the ROI size on PC-MRI total forward flow measurements in the ascending aorta (aAo), main pulmonary artery (PA), and right and left pulmonary arteries (RPA/LPA) of ten healthy volunteers (N=10). The results provide evidence-based suggestions for ROI contouring to increase measurement accuracy in PC-MRI.

METHODS

In Vivo Imaging Methods

All imaging was performed on a 3 Tesla MRI system (Trio, Siemens Medical Solutions, Erlangen, Germany) with 40 mT/m maximum gradient amplitude, 200 mT/m/s maximum slew rate, and 400 μs rise time. Our university's Institutional Review Board approved the study and informed consent was obtained for each subject prior to MRI scanning. Subjects were positioned head-first in the supine position on the scanner bed and imaged using a 6-element body matrix and 6-element spine matrix coils for signal reception. Blood flow was measured using PC-MRI in the aAo, PA, and RPA and LPA of ten (N=10) healthy volunteers (3 female, 7 male; age 25.9 ± 4.7 years) with no previous history of cardiovascular disease. The imaging plane for aAo flow was located in the ascending aorta immediately distal to the aortic valve and coronary ostia. The imaging plane for flow in the PA was located distal to the pulmonary valve and proximal to the first bifurcation. The imaging planes for the LPA and RPA were located ~1 cm distal to the pulmonary bifurcation. All PC-MRI imaging planes were prescribed from bSSFP cine images during end-systole with end-expiratory breath holds.

PC-MRI measurements were made using a cine spoiled gradient echo velocity-encoding sequence: TE/TR = 4.92/8.5 ms, 256 × 160 matrix, 1.3 × 1.3 × 6 mm^3 voxels, 30° flip angle, 814 Hz/pixel bandwidth, 4 views-per-segment, a total scan time of 23 heartbeats, a temporal resolution of 68 ms, retrospective ECG gating acquired during one end-expiratory breath hold, and GRAPPA (44) parallel imaging with an acceleration factor of 2 and 24 reference (central) k-space lines. 2D through-plane velocity encoding was performed using a VENC of 150cm/s. The chosen imaging protocol was designed to be insensitive to chemical shift effects (57). Eddy current correction (29) was conducted after each volunteer was imaged by duplicating each PC-MRI measurement in a stationary phantom. Non-zero velocity measurements within the phantom at the precise scan plane locations used for each subject arise due to eddy current induced background phase errors. Subtraction of the eddy current phantom measurements from the volunteer datasets results in PC-MRI measurements that are eddy current corrected. Automatic correction of Maxwell/concomitant gradient terms was employed (24) as implemented by the manufacturer. Therefore, our PC-MRI sequence and protocol minimizes the effects of chemical shift, eddy currents, and Maxwell terms.

Image Processing

Data were processed offline using a combination of MATLAB (The Mathworks, Natick, MA) and a DICOM viewing tool (Osirix, www.osirix-viewer.com) according to the following steps: 1) For quantitative flow assessment at each vessel territory, an arbitrarily shaped ROI was manually contoured to the vessel lumen/wall boundary within the PC-MRI magnitude images; 2) The eddy current stationary phantom images were then subtracted from the PC-MRI phase images for correction of eddy current-induced background phase errors (29); 3) The manually contoured ROI was then imported into the eddy current corrected phase images, which were subsequently analyzed with a custom Osirix plug-in; 4) Total forward flow measurements were computed by the plug-in, which scaled the mean ROI signal intensity (phase) by VENC/π (cm/s); 5) The resulting mean ROI velocities were then multiplied by the area of the ROI (cm^2) to calculate the flow rate (mL/s) and finally integrated over the cardiac cycle to yield the total forward flow result (mL).

The custom Osirix plug-in used the geometric center and the coordinates of each of the 100 automatically splined points from the manually contoured ROI to define a local radius. Each point along the ROI was then displaced radially to increase/decrease the local radii in increments of 1% over a range of ±25%. This process mimics the user's uncertainty about the precise vessel lumen-wall boundary. The percent-increment values were then converted to a pixel value in order to simplify the interpretation of the final results (i.e. it is more intuitive to interpret an increase/decrease in the size of an ROI in terms of pixels as opposed to a percentage of the ROIs radius). Figure 41 shows example PC-MRI phase images from a single volunteer in the aAo, PA, RPA, and LPA for the manual contoured (thick line) and ROIs with ±2 pixel increments (thin lines). The total forward flow was then computed for the manually contoured ROI and the additional 50 concentric ROIs.

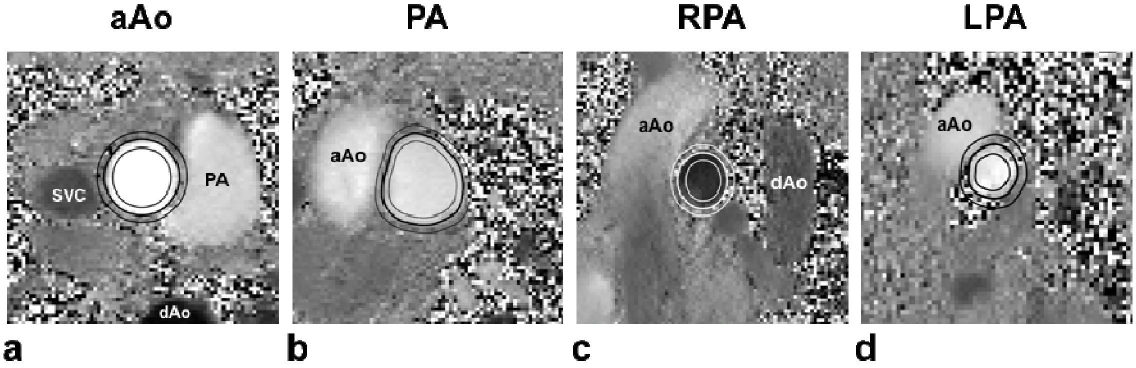

Figure 41. Example PC-MRI phase images and corresponding concentric ROIs in the ascending aorta (aAo), main pulmonary artery (PA), right pulmonary artery (RPA), and left pulmonary artery (LPA) of a single healthy volunteer. Manually contoured ROIs are shown with a thick line and examples of the computationally derived concentric ROIs with ±2 pixel increments are shown with thin lines. SVC: superior vena cava.

Data Analysis

The total forward flow error, ε, was calculated for each concentric ROI and for each vessel territory in every volunteer,

$$\epsilon = \frac{ROI_M - ROI_C}{ROI_M} \times 100, \qquad [1]$$

where ROI_M is the manually contoured ROI and ROI_C is one of the concentric ROIs. This results in 500 ε values (10 volunteers each with 50 adjusted ROIs) for each vessel territory. Due to the fact that the adjusted ROIs were radially increased/decreased by a percentage of the local radii and that the values of the local radii varied across both vessels and volunteers, each calculated value of ε did not correspond to the same pixel value. In other words, a 1% increase in the local radii for one volunteer may not correspond to the same pixel increase for another volunteer. After the ROI increments were converted to pixel increments, median values of ε were calculated by binning the values of ε from -2 to +2 pixels in bin widths of 0.2 pixels. The calculated values of ε were non-Gaussian distributed and of unequal variance, thus bootstrap statistical methods were used to compute the median and 95% confidence intervals of ε for each vessel by randomly resampling ε within each 0.2 pixel bin 2,000 times with replacement.

Lastly, the median ε and upper and lower 95% confidence intervals were then reported for each vessel. The total forward flow error rates were calculated for every volunteer within each vessel territory by fitting a line to the total forward flow error data for increased (0 pixels to +2 pixels) and decreased (0 pixels to -2 pixels) ROI sizes. The resulting total forward flow error rate was expressed in units of pixel^{-1}. A two-sample t-test with Holm-Sidak *post hoc* correction was used to measure the statistical significance of the differences in the measured total forward flow error rates between decreased and increased ROI sizes.

RESULTS

Figure 42 and Table 11 show the median total forward flow errors as a function of ROI pixel increment. A 1 pixel (1.3mm) increase in ROI size leads to a total forward flow error (median ± SD [lower 95%-CI, upper 95%-CI]) of 2.7 ± 1.9% [0.7, 3.4] for the aAo and 5.4 ± 3.7% [4.3, 7.9] for the PA, but a total forward flow error of 9.3 ± 4.8% [7.1, 12.8] for the RPA and 10.1 ± 4.2% [9.3, 11.0] LPA. A 1 pixel decrease in ROI size, however, leads to a total forward flow error of -10.1 ± 4.1% [-11.3, -8.3] for the aAo and -10.0 ± 5.0% [-12.9, -8.8] for the PA, but a total forward flow error of -19.5 ± 4.9% [-

21.5, -16.3] for the RPA and -19.1 ± 5.2% [-22.5, -17.3] for the LPA. A 2 pixel (2.6mm) increase in ROI size leads to a total forward flow error of 1.6 ± 2.5% [0.1, 3.9]% for the aAo and 8.5 ± 5.4% [5.0, 10.8]% for the PA, but a total forward flow error of 16.1 ± 8.5% [10.6, 18.8]% for the RPA and 19.8 ± 8.7% [19.0, 21.9]% LPA. A 2 pixel decrease in ROI size, however, leads to a total forward flow error of -22.4 ± 8.2% [-25.6, -15.4]% for the aAo and -24.6 ± 4.4% [-26.1, -21.7]% for the PA, but a total forward flow error of -44 ± 7.9% [-48.1, -40.8]% for the RPA and 43 ± 9.7% [-46.5, -38.4]% for the LPA. Note that the 95% confidence intervals narrowly surround the median total forward flow error for all vessels and all ROI pixel increments.

Table 12 compares the total forward flow error rates for each vessel territory as a function of increased/decreased ROI size in units of percent error per pixel (unit of pixel^{-1}). Total forward flow errors accumulate at a rate (median ± SD % error per pixel) of 0.9 ± 0.9 (aAo), 4.7 ± 2.8 (PA), 3.8 ± 4.7 (RPA), and 8.1 ± 5.2 (LPA) when the ROI size is increased. Conversely, total forward flow errors accumulate at a rate of 13.1 ± 4.2 (aAo), 13.9 ± 3.5 (PA), 23.4 ± 3.6 (RPA), and 20.3 ± 4.8 (LPA) when the ROI size is decreased. Total forward flow error rates were positive for every vessel territory in every volunteer. Additionally, the total forward error rates are higher for every vessel territory in every volunteer for decreased ROIs compared to increased ROIs. A comparison of the population median error rates for each vessel territory showed a statistically significant difference (Table 12).

Gatehouse et al. [19] described a 5% error in stroke volume to be a limit of acceptability in PC-MRI flow measurements. With these error criteria, ROIs drawn up to 2 pixels too large and/or 0.5 pixels too small in the aAo lead to ≤5% error in total forward flow measurements. In the PA, the Gatehouse threshold is maintained for ROIs drawn up to 0.9 pixels too large and/or 0.5 pixels too small. In the RPA, the Gatehouse threshold is maintained for ROIs drawn up to 0.4 pixels too large and/or 0.3 pixels too small. Finally, in the LPA, the Gatehouse threshold is maintained for ROIs drawn up to 0.3 pixels too large and/or 0.3 pixels too small.

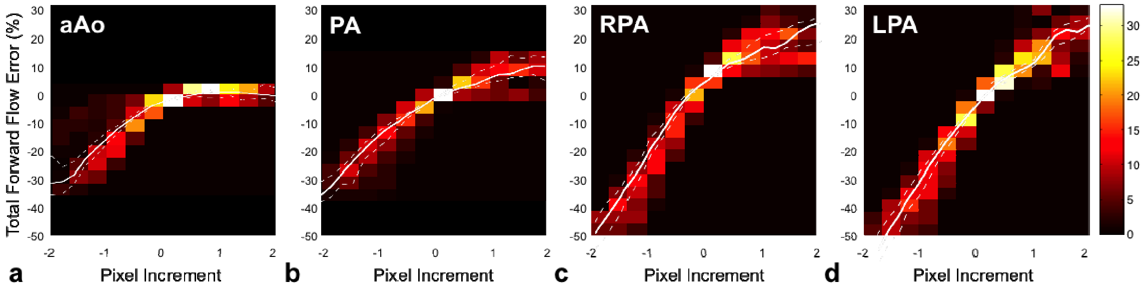

Figure 42. Median percent total forward flow error (solid white line) and the ±95% confidence intervals (dashed white lines) as a function of the ROI pixel increment for measurements in the (A) ascending aorta (aAo), (B) main pulmonary artery (PA), (C) right pulmonary artery (RPA), and (D) left pulmonary artery (LPA) in ten (N=10) healthy volunteers. The data are plotted over a two-dimensional histogram of the frequency of the total forward flow error binned into 0.25 pixel and 5% total forward flow error increments.

Table 11. Median percent total forward flow error for ±1 and ±2 pixel ROI increments.

Vessel	Decrease ROI		Increase ROI	
	-2 Pixels	**-1 Pixel**	**+1 Pixel**	**+2 Pixels**
aAo	-22.4 ± 8.2 [-25.6, -15.4]	-10.1 ± 4.1 [-11.3, -8.3]	2.7 ± 1.9 [0.7, 3.4]	1.6 ± 2.5 [0.1, 3.9]
PA	-24.6 ± 4.4 [-26.1, -21.7]	-10.0 ± 5.0 [-12.9, -8.8]	5.4 ± 3.7 [4.3, 7.9]	8.5 ± 5.4 [5.0, 10.8]
RPA	-44.0 ± 7.9 [-48.1, -40.8]	-19.5 ± 4.9 [-21.5, -16.3]	9.3 ± 4.8 [7.1, 12.8]	16.1 ± 8.5 [10.6, 18.8]
LPA	-43.0 ± 9.7 [-46.5, -38.4]	-19.1 ± 5.2 [-22.5, -17.3]	10.1 ± 4.2 [9.3, 11.0]	19.8 ± 8.7 [19.0, 21.9]

Median ± SD [lower 95%-CI, upper 95%-CI] percent flow error [95% confidence intervals] for each vessel territory (aAo – ascending aorta, PA – pulmonary artery, RPA – right PA, LPA – left PA) as a function of increased/decreased ROI radius.

Table 12. Rate at which total forward flow error is accumulated.

Vessel	Decrease ROI	Increase ROI
aAo	13.1 ± 4.2 [3.8, 16.9]	0.9 ± 0.9 [0.1, 3.2]
PA	13.9 ± 3.5 [10.4, 23.8]	4.7 ± 2.8 [0.1, 9.1]
RPA	23.4 ± 3.6 [20.0, 30.3]	3.8 ± 4.7 [0.5, 14.6]
LPA	20.3 ± 4.8 [15.1, 29.7]	8.1 ± 5.2 [1.6, 20.3]

Median ± SD [minimum, maximum] total forward flow error rates for each vessel territory (aAo – ascending aorta, PA – pulmonary artery, RPA – right PA, LPA – left PA) as a function of increased/decreased ROI size in units of pixel^{-1}.

A statistical significant difference ($P < 0.001$) between the median total forward flow error rate for increased/decreased ROI sizes was calculated for each vessel.

DISCUSSION

Across all vessels and volunteers, the magnitude of the total forward flow error is greater for ROIs that are smaller than the manually contoured ROI compared to ROIs that are larger than the manually contoured ROI. This is apparent qualitatively in Figure 42 wherein the slope of the median total forward flow error curves (white lines) are not symmetric about the zero-pixel shift. The slopes of the median total forward flow error curves for all vessels are lower for increasing ROI sizes, indicating that larger ROIs contribute a lower magnitude flow error than smaller ROIs. Additionally, the slopes of the individual volunteer total forward flow error curves are lower for increasing ROI sizes in every volunteer. Quantitatively, Table 12 shows a statistically significant difference between the slope of the error curves in Figure 42 for increased/decreased ROI sizes, which indicates that the lowest expected measurement error per pixel is achieved when the ROI is increased in size.

The aAo has a lower median total forward flow error as the ROI increases compared to other vessels, because the signal outside the vessel-lumen boundary comes mostly from stationary tissues with high signal magnitudes and therefore near-zero phase. The PA, RPA, and LPA have nearby flowing spins (e.g. other vessels) and/or low signal intensity tissues (e.g. lung) leading to poor phase estimation and significantly non-zero velocities. This accounts for the larger median total forward flow error as the ROI increases compared to the aAo. This can also be observed, qualitatively, in Figure 42 where the slope of the median total forward flow error curves for larger ROIs are steeper in the PA, RPA, and LPA, compared to the aAo.

The aAo has a much thicker vessel wall (1-2 pixels) compared to the PA, RPA, and LPA (~1 pixel). Thus, total forward flow measurements made in the aAo are less sensitive to errors as the ROI increases in size because the included phase contribution from the stationary vessel wall contributes a near-zero phase, which doesn’t contribute a significant measurement error. This becomes more of a problem for the PA, RPA, and LPA because the vessel wall is thinner and signal phase from the lungs and/or surrounding vessels may be included in the measurement, thus leading to a measurement error.

No user can be expected to contour an ROI as to include perfectly the vessel lumen and exclude the vessel wall, therefore ROI contouring is an obvious source of error in

PC-MRI flow measurements. In addition to providing evidence-based suggestions for ROI contouring in an effort to increase measurement accuracy in PC-MRI, this same analysis could be used to produce an objective measure of confidence in the reported flow measures. For example, after a user has contoured the necessary ROIs, the proposed analysis method, could then provide a confidence interval for the total forward flow assuming a user defined pixel error in the contoured ROI (e.g. ±0.5 pixel). To further illustrate this point, assume a measured total forward flow of 50mL. Alone, this flow measure does not provide any measure of confidence in the contoured ROI. However, if a calculated confidence interval was shown to be [47ml, 52mL] for a measured total forward flow of 50mL, then the user may conclude that errors in ROI placement has a relatively small effect on estimating the true forward flow. If, however, the calculated confidence interval was shown to be [41ml, 57mL] for a measured total forward flow of 50mL, then the user may conclude that errors in the ROI placement has a large influence on measurement variability and the ROI may need to be reconsidered more carefully, especially if the result is in poor agreement with other measures.

Limitations

Our total forward flow measurements were obtained using a PC-MRI protocol with suboptimal temporal resolution (68ms). For this study, temporal resolution was sacrificed for spatial resolution (1.3mm^2). Partial volume effects from a lower resolution acquisition likely contribute a larger error than low temporal resolution effects, especially considering we compared total forward flow measurements, rather than peak velocity.

Nevertheless, the suboptimal temporal resolution does not alter the measured total forward flow error as a function of ROI size.

Each point along the manually contoured ROI was adjusted radially by increasing or decreasing the ROI by the same pixel increment. This process mimics the user’s uncertainty about the precise vessel lumen-wall boundary, but does not perfectly mimic user ROI contouring errors. For example, most ROIs are not inappropriately contoured with uniform pixel increments in every radial direction, rather they may be off by a different pixel amount along every point of the ROI contour. Nevertheless, the analysis conducted herein is a systematic approach to determining the affect of ROI contouring on measurement errors in PC-MRI total forward flow measurements.

CONCLUSION

ROIs that are too large contribute a lower magnitude total forward error compared to ROIs that are too small, especially in the aAo. Accurately contouring a vessel boundary in a clinical setting is typically limited by post-processing time and suboptimal spatial resolution. Therefore, when uncertainty about the vessel-lumen boundary arises in a clinical setting, the magnitude of total forward flow errors may be reduced by erring towards a slightly (<1 pixel) larger ROI rather than contouring a smaller ROI. ROIs in the RPA and LPA (smaller vessels) are more prone to total forward flow errors than ROIs in the aAo and PA (larger vessels). Therefore, if the available time allotted for ROI contouring is critical, particular attention should be paid to carefully contour the RPA and LPA to ensure accurate flow results in these error prone territories.

CHAPTER 9

CONCLUSIONS

Phase-contrast MRI is subject to numerous sources of error, which decrease clinical confidence in the reported measures. This work outlines how stationary perivascular fat can impart a significant chemical shift-induced PC-MRI measurement error (up to 20%). The chemical shift induced phase errors can be reduced by using a high receiver bandwidth (BW) and an in-phase echo time (TE_{IN}). It was demonstrated that a high BW (814 Hz/px) and TE_{IN} (4.92 ms) significantly improves intrapatient net forward flow agreement compared with a low BW (401 Hz/px) and a mid-phase TE (3.08 ms) as indicated by significantly decreased measurement biases and limits of agreement for blood flow measurements made in the ascending aorta, main pulmonary artery, and the right/left branch pulmonary arteries in normal volunteers (N=10).

In an effort to increase the time efficiency of the chemical shift reduction strategy, a novel velocity encoding strategy, termed slice select refocused gradient (SSRG) encoded PC-MRI, was developed to enable the use of the minimum available TE_{IN} at 3T. It was demonstrated that SSRG with a high BW (814 Hz/px) and $TE_{IN,MIN}$ (2.46 ms) significantly improves intrapatient net forward flow agreement compared with FCFE with a low BW (401 Hz/px) and a mid-phase TE (3.08 ms) as indicated by significantly decreased measurement biases and limits of agreement for blood flow measurements made in the ascending aorta, main pulmonary artery, and the right/left branch pulmonary arteries in normal volunteers (N=10). In addition to reducing chemical shift-induced phase errors, a shorter TE/TR also allows an increase in spatiotemporal resolution and SNR, and/or a reduction in breath hold durations.

An analysis of the effects of ROI contouring showed that ROIs that are one pixel in radius too large contribute a lower magnitude total forward flow error compared to ROIs that are one pixel too small. Hence, the magnitude of the measurement error is smaller when slightly overestimating the ROI size compared to underestimating the ROI size. Nevertheless, especially careful attention must be paid when contouring ROIs for the smaller branch pulmonary arteries, as even a ±1 pixel increase in the size of the ROI leads to clinically significant total forward flow errors.

Lastly, convex gradient optimization (CVX) was used to construct time efficient gradients for chemical shift insensitive PC-MRI. CVX with a high BW and $TE_{IN,MIN}$ optimized for either spatial or temporal resolution provided higher measurements of flow and peak velocity compared to a conventional PC-MRI sequence at high BW and $TE_{IN,MIN}$.

Despite a reduction of chemical shift errors, increased spatiotemporal resolution, and ROI contouring error analysis, which are highlighted in this thesis work, several challenges still remain that may affect the clinical utility of PC-MRI measurements. PC-MRI has largely moved on to so-called “4D PC-MRI,” which provides beautiful images of three-dimensional flow fields over large regions of interest, but 4D PC-MRI results are also subject to the same errors that lead to inconsistent results in 2D through-plane PC-MRI. Despite other advantages 4D PC-MRI techniques typically do not achieve the high spatiotemporal resolution needed to assess smaller vessels due to the frequent use of moderate isotropic spatial and temporal resolutions, which are needed to achieve clinically feasible scan times. A 4D PC-MRI pulse sequence that is chemical shift insensitive and offers high spatiotemporal resolution with concomitant increases in SNR due to reductions in TE/TR would be clinically useful and could serve as a logical extension from the work described herein.

APPENDIX A

The following is a Matlab script detailing the solution for time efficient trapezoidal and triangular gradients for PC-MRI. The variable names match those listed in Figure 34 (Chapter 6).

```
VENC = 150; % velocity encoding strength, cm/s
gyro = 267.513; % gyromagnetic ratio, rad/(ms*mT)
DeltaM1 = pi*100*1000/(gyro*VENC); % First moment difference, mT/m*ms^2

% Slice Select Gradient
Gs = 15.6584; % slice select gradient amplitude, mT/m
Rs = 0.160; % slice select ramp time, ms
Fs = 0.6; % slice select gradient flat time, ms
SRs = Gs/Rs; % slice select gradient slew rate, mT/m/ms

% Readout Gradient
Gr = 11.5136; % readout gradient amplitude, mT/m
Rr = 0.120; % readout gradient ramp time, ms
Fr = 1.260; % readout gradient flat time, ms
ROsr = Gr/Rr; % readout gradient slew rate, mT/m/ms

% Phase Encoding Gradient
Gp = 20.4577; % phase encoding gradient amplitude, mT/m
Rp = 0.230; % phase encoding gradient ramp time, ms
Fp = 0.130; % phase encoding gradient flat top time, ms
PEArea = Gp*(Rp+Fp); % phase encoding area for max k-space line

% Gradient hardware Constraints
Gmax = 38;
SRmax = 170;
```

```
% Search for velocity encoding gradient amplitude, Gve, from Gmax to 0
for Gve = Gmax:-0.1:0,

   SR = 170/(sqrt(3)); % Maximum available gradient amplitude

   T2 = roundn(-(16*Fs*Gs + 16*Gs*Rs + 8*Rs*Gve)/(64*Gve) - ...
   (104*Gve^2 - (256*SR^2*Fs^2*Gs^2 + 512*SR^2*Fs*Gs^2*Rs + ...
   256*SR^2*Fs*Gs*Rs*Gve + 512/3*SR^2*Fs*Rs*Gve^2 + ...
   256*SR^2*Gs^2*Rs^2 + 256*SR^2*Gs*Rs^2*Gve - ...
   448/3*SR^2*Rs^2*Gve^2 + 2048*DeltaM1*SR^2*Gve + ...
   256*SR*Fs*Gs*Gve^2 - 512/3*SR*Fs*Gve^3 + 256*SR*Gs*Rs*Gve^2 - ...
   896/3*SR*Rs*Gve^3 + 1216*Gve^4)^(1/2))/(64*SR*Gve),-2);

   T4 = roundn((6^(1/2)*(6*SR^2*Fs^2*Gs^2 + ...
   12*SR^2*Fs*Gs^2*Rs + 6*SR^2*Fs*Gs*Rs*Gve + ...
   2*SR^2*Fs*Rs*Gve^2 + 6*SR^2*Gs^2*Rs^2 + ...
   6*SR^2*Gs*Rs^2*Gve - SR^2*Rs^2*Gve^2 - 24*SR^2*T2^2*Gve^2 + ...
   24*DeltaM1*SR^2*Gve + 6*SR*Fs*Gs*Gve^2 - 2*SR*Fs*Gve^3 + ...
   6*SR*Gs*Rs*Gve^2 - 2*SR*Rs*Gve^3 - 72*SR*T2*Gve^3 - ...
   39*Gve^4)^(1/2))/(12*SR*Gve) - (3*Gve)/(2*SR),-2);

   T3 = roundn(Gve/(2*SR) - ((Fs*Gs)/2 + (Gs*Rs)/2 + ...
   (Gve*(Rs - 2*T4))/2)/Gve,-2);

   T1 = roundn(T2 + (Gs*(Fs + Rs))/(2*Gve),-2);

   % Ensure the velocity encoding gradient durations are equal
   C = T1 + T2 + Rs + 4*roundn((Gve/SR),-2) - (3*roundn((Gve/SR),-2) + ...
   T3 + T4 + Rs);

   % Phase encoding gradient can be constructed based on Time_VE and
   PEArea.
   Time_VE = T1 + T2 + Rs + 4*roundn((Gve/SR),-2);
   Rp = roundn(0.5*Time_VE,-2);
   Gp = PEArea/Rp;
   PEsr = Gp/Rp;

   % Maximum available gradient amplitude, g, and slew rate, SR1, for
   the flow compensated readout gradient
   g = (Gmax^2 - Gve^2 - Gp^2)^(1/2);
   SR1 = (SRmax^2 - SR^2 - PEsr^2)^(1/2);

   % Construction of the flow compensated readout gradient
   Gr = g;

   F2 = roundn(((Gr*Fr)/2 + (2*Gr*Rr)/3)/Gr + ...
   (((Gr^2*Fr^2*SR1^2)/2 + (4*Gr^2*Fr*Rr*SR1^2)/3 + ...
   (17*Gr^2*Rr^2*SR1^2)/18 + (Gr^2*Fr^2*SR1^2)/2 + ...
   (4*Gr^3*Fr*SR1)/3 + 2*Gr^2*Fr*Rr*SR1^2 + ...
   2*Gr^3*Rr*SR1 + (4*Gr^2*Rr^2*SR1^2)/3 + ...
   (Gr^2*Rr*SR1^2)/5 + Gr^4)^(1/2)/2 - (3*Gr^2)/2)/(Gr*SR1),-2);

   F1 = roundn(f2 - (Gr*(Fr + Rr))/(2*Gr),-2);

   % Ensure tGvee readout and velocity encoding durations are equal
   D = T1 + T2 + Rs + 4*roundn((Gve/SR),-2) - ...
   (4*roundn((Gr/SR1),-2) + f1 + f2 + Rr);

   % Terminate for loop with a solved solution when the velocity encoding
   durations are equal and of the same duration of the flow compensated readout
   if abs(D) <= 0.01 && abs(C) <= 0.01,
      break
   end

end
```

APPENDIX B

The following is a Matlab script detailing the convex gradient optimization for all gradients within the CVX PC-MRI pulse sequence. The CVX Matlab libraries, not included here, can be downloaded from http://cvxr.com/cvx.

```
% Optimization of the Slice, Read, and Phase gradients optimized during the time
between RF transmission and data acquisition (i.e. the end of the slice select
gradient plateau and the start of the readout gradient plateau)

VENC = 150; % velocity encoding strength, cm/s
gyro = 267.513; % gyromagnetic ratio, rad/(ms*mT)
DeltaM1 = pi*100*1000/(gyro*VENC); % First moment difference, mT/m*ms²

% Slice Select Gradient
Gs = 15.6584; % slice select gradient amplitude, mT/m
Rs = 0.160; % slice select ramp time, ms
Fs = 0.6; % slice select gradient flat time, ms
SRs = Gs/Rs; % slice select gradient slew rate, mT/m/ms

% Readout Gradient
Gr = 11.5136; % readout gradient amplitude, mT/m
Rr = 0.120; % readout gradient ramp time, ms
Fr = 1.260; % readout gradient flat time, ms
ROsr = Gr/Rr; % readout gradient slew rate, mT/m/ms

% Phase Encoding Gradient
Gp = 20.4577; % phase encoding gradient amplitude, mT/m
Rp = 0.230; % phase encoding gradient ramp time, ms
Fp = 0.130; % phase encoding gradient flat top time, ms
PEArea = Gp*(Rp+Fp); % phase encoding area for max k-space line

Mss0 = gyro*((1)*Gs*(0.5*Fs)); % slice select zero momemt, mT*ms/m
Mss1 = gyro *((1/2)*Gs*((0.5*Fs)^2)); % slice select first momemt, mT*ms^2/m

Mpe0 = 4258*(Gp*(Fp+Rp)); % phase encoding zero momemt, mT*ms/m
Mpe1 = []; % phase encoding first moment, mT*ms^2/m

% Both M0 and M1 for the readout gradient need to be nulled at the echo time.
Solved within the CVX code because they depend on the durations of the
gradients, which we do not know a priori
Mro0 = []; % Readout M0
Mro1 = []; % Readout M1

% Lower and upper search bounds
N_est = [100 150];

% Initial gradient amplitudes for slice1, phase, read, and slice2, mT/m
g0 = [Gs 0 0 Gs];

% Final gradient amplitudes for slice1, phase, read, and slice2, mT/m
gf = [0 0 Gr 0];

% Gradient sampling time, ms
T = 10e-3;

GMAX = 38; % Maximum gradient amplitude, mT/m
SMAX = 170; % Maximum gradient slew rate (individual axis), mT/m/ms
t0 = 0.5*Fs; % Starting time of gradients, ms
cvx_solver SDPT3;

% turn off output from CVX
cvx_quiet(true);

% init bisection interval
```

```
n_top = N_est(2); % smallest feasible N
n_bot = N_est(1); % largest unfeasible N

% bisection
% solve a sequence of feasibility problems
done = 0; n = n_top;
while( done==0 )
% ------------------------------------------------------------------------
dbgstr = sprintf('mtgrad3d_cvx: n=%d, [n_bot=%d,n_top=%d]',n,n_bot,n_top);
Nf = n;

% form difference matrix to calculate slew rate
D = diag(-ones(n,1),0) + diag(ones(n-1,1),1);
D = D(1:end-1,:);

% form time vector to calculate moments
tvec = t0 + [0:n-1]*T; % in sec
% tMat for all moments
tMat = zeros( Nm, n );
for mm=1:Nm,
    tMat( mm, : ) = tvec.^(mm-1);
end

cvx_begin
  variable g(n, 4);
  % no objective function
  % ...
  subject to
  % start ampl
  g(1,:) == g0;
  % end ampl
  g(n,:) == gf;

  % Slice Select Moments
  gyro *T*tMat(1,:)*g(:,1) == -Mss0; % Slice Select1 M0
  gyro *T*tMat(1,:)*g(:,4) == -Mss0; % Slice Select2 M0
  gyro *T*tMat(2,:)*g(:,1) - gyro*T*tMat(2,:)*g(:,4) == dM1; % Slice Select •M1

  % Phase Encoding Moments
  gyro*T*tMat(1,:)*g(:,2) == -Mpe0; % Phase Encode M0
  gyro *T*tMat(2,:)*g(:,2) == -Mpe1; % Phase Encode M1

  % Determine the Readout Moments based on current gradient duration
  t1 = tMat(2,end);
  t2 = t1 + 0.5*ROf;

  Mro0 = gyro*((1)*g(n,3)*(t2 - t1));       % Readout M0
  Mro1 = gyro*((1/2)*g(n,3)*(t2^2 - t1^2)); % Readout M1

  gyro*T*tMat(1,:)*g(:,3) == -Mro0; % Readout M0
  gyro *T*tMat(2,:)*g(:,3) == -Mro1; % Readout M1

  % Gradient amplitude constraints for limiting slice orientation
  square(g(:,1)) + square(g(:,2)) + square(g(:,3)) <= GMAX*GMAX;
  square(g(:,4)) + square(g(:,2)) + square(g(:,3)) <= GMAX*GMAX;
  square(g(:,1)) <= GMAX*GMAX;
  square(g(:,2)) <= GMAX*GMAX;
  square(g(:,3)) <= GMAX*GMAX;
  square(g(:,4)) <= GMAX*GMAX;
  % Slew constraints (sum of square roots on all axis)
  square(D*g(:,1)/T) + square(D*g(:,2)/T) + square(D*g(:,3)/T) <= SMAX*SMAX;
  square(D*g(:,4)/T) + square(D*g(:,2)/T) + square(D*g(:,3)/T) <= SMAX*SMAX;
  square(g(:,1)) <= SMAX*SMAX;
  square(g(:,2)) <= SMAX*SMAX;
  square(g(:,3)) <= SMAX*SMAX;
  square(g(:,4)) <= SMAX*SMAX;

cvx_end

% check variables, update bisection interval
%   cvx_optval is meaningless, since there's no objective function
%   cvx_status is either Solved or Infeasible
```

```
if( strfind(cvx_status,'Solved') ) % feasible
    dbgstr = sprintf('%s, Solved', dbgstr);
    feas = 1;

    n_top = n;
    n = round( 0.5*(n_top+n_bot) );
    % update feasible g
    grad = g; %.';
else
    dbgstr = sprintf('%s, Infeasible', dbgstr);

    n_bot = n;
    n = round( 0.5*(n_top+n_bot) );
end
% check termination condition
if( n_top<=n_bot+1 )
    if( exist('grad') )
        done = 1;
    else
        % if we're here, n_top was infeasible to start with
        n_top = n_top*2;
        n = n_top;
    end
end
% hard termination condition
if( n > N_max )
    disp( sprintf('mtgrad3d_cvx: n=%d > N_max=%d, terminating
bisection.',n,N_max) );
    done = 1;
end

% output status of current iteration
if( DBGMSG )
    disp( dbgstr );
end
% -------------------------------------------------------------------------
end % while loop

% let CVX talk again
cvx_quiet(false);

return;
```

```
% Optimization of the Slice, Read, and Phase gradients optimized the time
between the end of data acquisition (i.e. end of the readout plateau) and the
end of the TR

% Slice Select Gradient
Gs = 15.6584; % slice select gradient amplitude, mT/m
Rs = 0.160; % slice select ramp time, ms
Fs = 0.6; % slice select gradient flat time, ms
SRs = Gs/Rs; % slice select gradient slew rate, mT/m/ms
dz = 0.005; % slice thickness, m

% Readout Gradient
Gr = 11.5136; % readout gradient amplitude, mT/m
Rr = 0.120; % readout gradient ramp time, ms
Fr = 1.260; % readout gradient flat time, ms
ROsr = Gr/Rr; % readout gradient slew rate, mT/m/ms

% Phase Encoding Gradient
Gp = 20.4577; % phase encoding gradient amplitude, mT/m
Rp = 0.230; % phase encoding gradient ramp time, ms
Fp = 0.130; % phase encoding gradient flat top time, ms
PEArea = Gp*(Rp+Fp); % phase encoding area for max k-space line

Mpe0 = 4258*(Gp*(Fp+Rp)); % phase encoding zero momemt, mT*ms/m
Mpe1 = []; % phase encoding first moment, mT*ms^2/m

% We don’t care about the readout moment as we are just building the ramp down
of the readout gradient
Mro0 = []; % Readout M0
Mro1 = []; % Readout M1

Spoil_Phase = 4*pi; % Amount of desired spoiler dephasing, rad
Mss0 = Spoil_Phase/((gyro*dz)/(10*1000));
Mss1 = [];

% Lower and upper search bounds
N_est = [0 100];

% Initial gradient amplitudes for spoil, phase, and read, mT/m
g0 = [0 0 Gr];

% Final gradient amplitudes for spoil, phase, and read, mT/m
gf = [0 0 0];

% Gradient sampling time, ms
T = 10e-3;

GMAX = 38; % Maximum gradient amplitude, mT/m
SMAX = 170; % Maximum gradient slew rate (individual axis), mT/m/ms
t0 = 0; % Starting time of gradients, ms
```

```
cvx_solver SDPT3;

% turn off output from CVX
cvx_quiet(true);

% init bisection interval
n_top = N_est(2); % smallest feasible N
n_bot = N_est(1); % largest unfeasible N

% bisection
% solve a sequence of feasibility problems
done = 0; n = n_top;
while( done==0 )
% -----------------------------------------------------------------------
dbgstr = sprintf('mtgrad3d_cvx: n=%d, [n_bot=%d,n_top=%d]',n,n_bot,n_top);
Nf = n;

% form difference matrix to calculate slew rate
D = diag(-ones(n,1),0) + diag(ones(n-1,1),1);
D = D(1:end-1,:);

% form time vector to calculate moments
tvec = t0 + [0:n-1]*T; % in sec
% tMat for all moments
tMat = zeros( Nm, n );
for mm=1:Nm,
    tMat( mm, : ) = tvec.^(mm-1);
end

cvx_begin
  variable g(n, 2);
  % no objective function
  % ...
  subject to
  % start ampl
  g(1,:) == g0;
  % end ampl
  g(n,:) == gf;

  % Spoiler Moments
  GAM*T*tMat(1,:)*g(:,1) == Mss0;
  GAM*T*tMat(2,:)*g(:,1) == Mss1;

  % Phase Encoding Moments
  GAM*T*tMat(1,:)*g(:,2) == Mpe0;
  GAM*T*tMat(2,:)*g(:,2) == Mro0;

  % Readout Moments
  GAM*T*tMat(1,:)*g(:,3) == Mpe1;
  GAM*T*tMat(2,:)*g(:,3) == Mro1;

  % Gradient amplitude constraints for limiting slice orientation
  square(g(:,1)) + square(g(:,2)) + square(g(:,3)) <= GMAX*GMAX;
  square(g(:,1)) <= GMAX*GMAX;
  square(g(:,2)) <= GMAX*GMAX;
  square(g(:,3)) <= GMAX*GMAX;

  % Slew constraints (sum of square roots on all axis)
  square(D*g(:,1)/T) + square(D*g(:,2)/T) + square(D*g(:,3)/T) <= SMAX*SMAX;
  square(g(:,1)) <= SMAX*SMAX;
  square(g(:,2)) <= SMAX*SMAX;
  square(g(:,3)) <= SMAX*SMAX;

cvx_end

% check variables, update bisection interval
%   cvx_optval is meaningless, since there's no objective function
%   cvx_status is either Solved or Infeasible
if( strfind(cvx_status,'Solved') ) % feasible
    dbgstr = sprintf('%s, Solved', dbgstr);
    feas = 1;
```

```
    n_top = n;
    n = round( 0.5*(n_top+n_bot) );
    % update feasible g
    grad = g; %.';
else
    dbgstr = sprintf('%s, Infeasible', dbgstr);

    n_bot = n;
    n = round( 0.5*(n_top+n_bot) );
end
% check termination condition
if( n_top<=n_bot+1 )
    if( exist('grad') )
        done = 1;
    else
        % if we're here, n_top was infeasible to start with
        n_top = n_top*2;
        n = n_top;
    end
end
% hard termination condition
if( n > N_max )
    disp( sprintf('mtgrad3d_cvx: n=%d > N_max=%d, terminating
bisection.',n,N_max) );
    done = 1;
end

% output status of current iteration
if( DBGMSG )
    disp( dbgstr );
end
% ------------------------------------------------------------------------
end % while loop

% let CVX talk again
cvx_quiet(false);

return;
```

REFERENCES

1. Hoffman JI, Kaplan S. The incidence of congenital heart disease. J Am Coll Cardiol 2002;39(12):1890-1900.

2. Warnes CA, Williams RG, Bashore TM, Child JS, Connolly HM, Dearani JA, Del Nido P, Fasules JW, Graham TP, Jr., Hijazi ZM, Hunt SA, King ME, Landzberg MJ, Miner PD, Radford MJ, Walsh EP, Webb GD. ACC/AHA 2008 Guidelines for the Management of Adults with Congenital Heart Disease: Executive Summary: a report of the American College of Cardiology/American Heart Association Task Force on Practice Guidelines (writing committee to develop guidelines for the management of adults with congenital heart disease). Circulation 2008;118(23):2395-2451.

3. Russo CA, Elixhauser A. Hospitalizations for Birth Defects in 2004. HCUP Statistical Brief #24 2007;U.S. Agency for Healthcare Research and Quality(Rockville, MD).

4. Lotz J, Meier C, Leppert A, Galanski M. Cardiovascular flow measurement with phase-contrast MR imaging: basic facts and implementation. Radiographics 2002;22(3):651-671.

5. Pelc NJ. Flow quantification and analysis methods. Magn Reson Imaging Clin N Am 1995;3(3):413-424.

6. Prakash A, Powell AJ, Geva T. Multimodality noninvasive imaging for assessment of congenital heart disease. Circulation Cardiovascular imaging 2010;3(1):112-125.

7. Pennell DJ, Sechtem UP, Higgins CB, Manning WJ, Pohost GM, Rademakers FE, van Rossum AC, Shaw LJ, Yucel EK. Clinical indications for cardiovascular magnetic resonance (CMR): Consensus Panel report. J Cardiovasc Magn Reson 2004;6(4):727-765.

8. Rebergen SA, Chin JG, Ottenkamp J, van der Wall EE, de Roos A. Pulmonary regurgitation in the late postoperative follow-up of tetralogy of Fallot. Volumetric quantitation by nuclear magnetic resonance velocity mapping. Circulation 1993;88(5 Pt 1):2257-2266.

9. Prakash A, Powell AJ, Geva T. Multimodality noninvasive imaging for assessment of congenital heart disease. Circ Cardiovasc Imaging;3(1):112-125.

10. Bonow RO, Carabello BA, Kanu C, de Leon AC, Jr., Faxon DP, Freed MD, Gaasch WH, Lytle BW, Nishimura RA, O'Gara PT, O'Rourke RA, Otto CM, Shah PM, Shanewise JS, Smith SC, Jr., Jacobs AK, Adams CD, Anderson JL, Antman EM, Fuster V, Halperin JL, Hiratzka LF, Hunt SA, Nishimura R, Page RL, Riegel B. ACC/AHA 2006 guidelines for the management of patients with valvular heart

disease: a report of the American College of Cardiology/American Heart Association Task Force on Practice Guidelines (writing committee to revise the 1998 Guidelines for the Management of Patients With Valvular Heart Disease): developed in collaboration with the Society of Cardiovascular Anesthesiologists: endorsed by the Society for Cardiovascular Angiography and Interventions and the Society of Thoracic Surgeons. Circulation 2006;114(5):e84-231.

11. Geva T. Repaired tetralogy of Fallot: the roles of cardiovascular magnetic resonance in evaluating pathophysiology and for pulmonary valve replacement decision support. J Cardiovasc Magn Reson 2011;13:9.

12. Oosterhof T, van Straten A, Vliegen HW, Meijboom FJ, van Dijk AP, Spijkerboer AM, Bouma BJ, Zwinderman AH, Hazekamp MG, de Roos A, Mulder BJ. Preoperative thresholds for pulmonary valve replacement in patients with corrected tetralogy of Fallot using cardiovascular magnetic resonance. Circulation 2007;116(5):545-551.

13. Trivedi KR, Benson LN. Interventional strategies in the management of peripheral pulmonary artery stenosis. Journal of interventional cardiology 2003;16(2):171-188.

14. Bryant DJ, Payne JA, Firmin DN, Longmore DB. Measurement of flow with NMR imaging using a gradient pulse and phase difference technique. J Comput Assist Tomogr 1984;8(4):588-593.

15. Nayler GL, Firmin DN, Longmore DB. Blood flow imaging by cine magnetic resonance. J Comput Assist Tomogr 1986;10(5):715-722.

16. Axel L, Morton D. MR flow imaging by velocity-compensated/uncompensated difference images. J Comput Assist Tomogr 1987;11(1):31-34.

17. van Dijk P. Direct cardiac NMR imaging of heart wall and blood flow velocity. J Comput Assist Tomogr 1984;8(3):429-436.

18. Gatehouse PD, Keegan J, Crowe LA, Masood S, Mohiaddin RH, Kreitner KF, Firmin DN. Applications of phase-contrast flow and velocity imaging in cardiovascular MRI. Eur Radiol 2005;15(10):2172-2184.

19. Srichai MB, Lim RP, Wong S, Lee VS. Cardiovascular applications of phase-contrast MRI. AJR Am J Roentgenol 2009;192(3):662-675.

20. Keller PJ, Wehrli FW. Gradient moment nulling through the Nth moment: application of binomial expansion coefficients to gradient amplitudes. J Magn Reson 1988;78:145-149.

21. Axel L. Blood flow effects in magnetic resonance imaging. AJR Am J Roentgenol 1984;143(6):1157-1166.

22. Bernstein MA, Shimakawa A, Pelc NJ. Minimizing TE in moment-nulled or flow-encoded two- and three-dimensional gradient-echo imaging. J Magn Reson Imaging 1992;2(5):583-588.

23. Markl M, Bammer R, Alley MT, Elkins CJ, Draney MT, Barnett A, Moseley ME, Glover GH, Pelc NJ. Generalized reconstruction of phase contrast MRI: analysis and correction of the effect of gradient field distortions. Magn Reson Med 2003;50(4):791-801.

24. Bernstein MA, Zhou XJ, Polzin JA, King KF, Ganin A, Pelc NJ, Glover GH. Concomitant gradient terms in phase contrast MR: analysis and correction. Magn Reson Med 1998;39(2):300-308.

25. Gatehouse PD, Rolf MP, Graves MJ, Hofman MB, Totman J, Werner B, Quest RA, Liu Y, von Spiczak J, Dieringer M, Firmin DN, van Rossum A, Lombardi M, Schwitter J, Schulz-Menger J, Kilner PJ. Flow measurement by cardiovascular magnetic resonance: a multi-centre multi-vendor study of background phase offset errors that can compromise the accuracy of derived regurgitant or shunt flow measurements. J Cardiovasc Magn Reson 2010;12:5.

26. Lankhaar JW, Hofman MB, Marcus JT, Zwanenburg JJ, Faes TJ, Vonk-Noordegraaf A. Correction of phase offset errors in main pulmonary artery flow quantification. J Magn Reson Imaging 2005;22(1):73-79.

27. Walker PG, Cranney GB, Scheidegger MB, Waseleski G, Pohost GM, Yoganathan AP. Semiautomated method for noise reduction and background phase error correction in MR phase velocity data. J Magn Reson Imaging 1993;3(3):521-530.

28. Bakker CJ, Hoogeveen RM, Viergever MA. Construction of a protocol for measuring blood flow by two-dimensional phase-contrast MRA. J Magn Reson Imaging 1999;9(1):119-127.

29. Chernobelsky A, Shubayev O, Comeau CR, Wolff SD. Baseline correction of phase contrast images improves quantification of blood flow in the great vessels. J Cardiovasc Magn Reson 2007;9(4):681-685.

30. Miller TA, Landes AB, Moran AM. Improved accuracy in flow mapping of congenital heart disease using stationary phantom technique. J Cardiovasc Magn Reson 2009;11:52.

31. Firmin DN, Nayler GL, Klipstein RH, Underwood SR, Rees RS, Longmore DB. In vivo validation of MR velocity imaging. J Comput Assist Tomogr 1987;11(5):751-756.

32. Attili AK, Parish V, Valverde I, Greil G, Baker E, Beerbaum P. Cardiovascular MRI in childhood. Arch Dis Child.

33. Kondo C, Caputo GR, Semelka R, Foster E, Shimakawa A, Higgins CB. Right and left ventricular stroke volume measurements with velocity-encoded cine MR imaging: in vitro and in vivo validation. AJR Am J Roentgenol 1991;157(1):9-16.

34. Bernstein MA, Ikezaki Y. Comparison of phase-difference and complex-difference processing in phase-contrast MR angiography. J Magn Reson Imaging 1991;1(6):725-729.

35. Ferrigno M, Hickey DD, Liner MH, Lundgren CE. Cardiac performance in humans during breath holding. J Appl Physiol 1986;60(6):1871-1877.

36. Paulev P, Wetterqvist H. Cardiac output during breath-holding in man. Scand J Clin Lab Invest 1968;22(2):115-123.

37. Polzin JA, Alley MT, Korosec FR, Grist TM, Wang Y, Mistretta CA. A complex-difference phase-contrast technique for measurement of volume flow rates. J Magn Reson Imaging 1995;5(2):129-137.

38. Spritzer CE, Pelc NJ, Lee JN, Evans AJ, Sostman HD, Riederer SJ. Rapid MR imaging of blood flow with a phase-sensitive, limited-flip-angle, gradient recalled pulse sequence: preliminary experience. Radiology 1990;176(1):255-262.

39. Soila KP, Viamonte M, Jr., Starewicz PM. Chemical shift misregistration effect in magnetic resonance imaging. Radiology 1984;153(3):819-820.

40. Gao JH, Holland SK, Gore JC. Nuclear magnetic resonance signal from flowing nuclei in rapid imaging using gradient echoes. Med Phys 1988;15(6):809-814.

41. Edden RA, Smith SA, Barker PB. Longitudinal and multi-echo transverse relaxation times of normal breast tissue at 3 Tesla. J Magn Reson Imaging;32(4):982-987.

42. Stanisz GJ, Odrobina EE, Pun J, Escaravage M, Graham SJ, Bronskill MJ, Henkelman RM. T1, T2 relaxation and magnetization transfer in tissue at 3T. Magn Reson Med 2005;54(3):507-512.

43. Govindaraju V, Young K, Maudsley AA. Proton NMR chemical shifts and coupling constants for brain metabolites. NMR Biomed 2000;13(3):129-153.

44. Griswold MA, Jakob PM, Heidemann RM, Nittka M, Jellus V, Wang J, Kiefer B, Haase A. Generalized autocalibrating partially parallel acquisitions (GRAPPA). Magn Reson Med 2002;47(6):1202-1210.

45. Tanaka S, Yoshiyama M, Imanishi Y, Nakahira K, Hanaki T, Naito Y, Imai M, Tanaka M. MR measurement of visceral fat: assessment of metabolic syndrome. Magn Reson Med Sci 2006;5(4):207-210.

46. Tanaka S, Yoshiyama M, Imanishi Y, Teragaki M, Kasayuki N, Shimizu N, Nakahira K, Hanaki T, Naito Y, Tanaka M, Inoue Y. Measuring visceral fat with water-selective suppression methods (SPIR, SPAIR) in patients with metabolic syndrome. Magn Reson Med Sci 2007;6(3):171-175.

47. Holland BJ, Printz BF, Lai WW. Baseline correction of phase-contrast images in congenital cardiovascular magnetic resonance. J Cardiovasc Magn Reson;12:11.

48. Bland JM, Altman DG. Statistical methods for assessing agreement between two methods of clinical measurement. Lancet 1986;1(8476):307-310.

49. Johnson KM, Wieben O, Samsonov AA. Phase-contrast velocimetry with simultaneous fat/water separation. Magn Reson Med 2010;63(6):1564-1574.

50. Brodsky EK, Holmes JH, Yu H, Reeder SB. Generalized k-space decomposition with chemical shift correction for non-Cartesian water-fat imaging. Magn Reson Med 2008;59(5):1151-1164.

51. Meyer CH, Pauly JM, Macovski A, Nishimura DG. Simultaneous spatial and spectral selective excitation. Magn Reson Med 1990;15(2):287-304.

52. Moriguchi H, Lewin JS, Duerk JL. Dixon techniques in spiral trajectories with off-resonance correction: A new approach for fat signal suppression without spatial-spectral RF pulses. Magn Reson Med 2003;50:915–924.

53. Pelc NJ, Sommer FG, Li KC, Brosnan TJ, Herfkens RJ, Enzmann DR. Quantitative magnetic resonance flow imaging. Magn Reson Q 1994;10(3):125-147.

54. Anderson A, Kirsch J. Analysis of noise in phase contrast MR imaging. Med Phys 1996;23(6):857-869.

55. Westenberg JJ, Roes SD, Ajmone Marsan N, Binnendijk NM, Doornbos J, Bax JJ, Reiber JH, de Roos A, van der Geest RJ. Mitral valve and tricuspid valve blood flow: accurate quantification with 3D velocity-encoded MR imaging with retrospective valve tracking. Radiology 2008;249(3):792-800.

56. Lufkin R, Anselmo M, Crues J, Smoker W, Hanafee W. Magnetic field strength dependence of chemical shift artifacts. Comput Med Imaging Graph 1988;12(2):89-96.

57. Middione MJ, Ennis DB. The effects of chemically shifted perivascular fat in quantitative phase contrast MRI. Magn Reson Med 2013;69:391-401.

58. Markl M, Alley MT, Pelc NJ. Balanced phase-contrast steady-state free precession (PC-SSFP): a novel technique for velocity encoding by gradient inversion. Magn Reson Med 2003;49(5):945-952.

59. Thompson RB, McVeigh ER. Real-time volumetric flow measurements with complex-difference MRI. Magn Reson Med 2003;50(6):1248-1255.

60. Atkinson DJ, Edelman RR. Cineangiography of the heart in a single breath hold with a segmented turboFLASH sequence. Radiology 1991;178(2):357-360.

61. Gatehouse PD, Rolf MP, Graves MJ, Hofman MB, Totman J, Werner B, Quest RA, Liu Y, von Spiczak J, Dieringer M, Firmin DN, van Rossum A, Lombardi M, Schwitter J, Schulz-Menger J, Kilner PJ. Flow measurement by cardiovascular magnetic resonance: a multi-centre multi-vendor study of background phase offset

errors that can compromise the accuracy of derived regurgitant or shunt flow measurements. J Cardiovasc Magn Reson;12:5.

62. Rolf MP, Hofman MB, Gatehouse PD, Markenroth-Bloch K, Heymans MW, Ebbers T, Graves MJ, Totman JJ, Werner B, van Rossum AC, Kilner PJ, Heethaar RM. Sequence optimization to reduce velocity offsets in cardiovascular magnetic resonance volume flow quantification--a multi-vendor study. J Cardiovasc Magn Reson;13:18.

63. Stalder AF, Frydrychowicz A, Russe MF, Korvink JG, Hennig J, Li K, Markl M. Assessment of flow instabilities in the healthy aorta using flow-sensitive MRI. J Magn Reson Imaging 2011;33(4):839-846.

64. Ganong WF. Review of Medical Physiology. 22nd Edition. New York: Lange Medical Books/ McGraw-Hill 2005.

65. Lin HY, Bender JA, Ding Y, Chung YC, Hinton AM, Pennell ML, Whitehead KK, Raman SV, Simonetti OP. Shared velocity encoding: A method to improve the temporal resolution of phase-contrast velocity measurements. Magn Reson Med 2012;68:703–710.

66. Wedeen VJ, Weisskoff RM, Poncelet BP. MRI signal void due to in-plane motion is all-or-none. Magn Reson Med 1994;32(1):116-120.

67. Geva T. Indications and timing of pulmonary valve replacement after tetralogy of Fallot repair. Semin Thorac Cardiovasc Surg Pediatr Card Surg Annu 2006:11-22.

68. Middione MJ, Ennis DB. Velocity Encoding With the Slice Select Refocusing Gradient for Faster Imaging and Reduced Chemical Shift-Induced Phase Errors. Magn Reson Med 2013. doi: 10.1002/mrm.24861.

69. Chatzimavroudis GP, Zhang H, Halliburton SS, Moore JR, Simonetti OP, Schvartzman PR, Stillman AE, White RD. Clinical blood flow quantification with segmented k-space magnetic resonance phase velocity mapping. J Magn Reson Imaging 2003;17(1):65-71.

70. Laffon E, Lecesne R, De Ledinghen V, Valli N, Couzigou P, Laurent F, Drouillard J, Ducassou D, Barat JL. Segmented 5 versus nonsegmented flow quantitation: comparison of portal vein flow measurements. Invest Radiol 1999;34(3):176-180.

71. Tang C, Blatter DD, Parker DL. Accuracy of phase-contrast flow measurements in the presence of partial-volume effects. J Magn Reson Imaging 1993;3(2):377-385.

72. Tang C, Blatter DD, Parker DL. Correction of partial-volume effects in phase-contrast flow measurements. J Magn Reson Imaging 1995;5(2):175-180.

73. Eichenberger AC, Schwitter J, McKinnon GC, Debatin JF, von Schulthess GK. Phase-contrast echo-planar MR imaging: real-time quantification of flow and velocity patterns in the thoracic vessels induced by Valsalva's maneuver. J Magn Reson Imaging 1995;5(6):648-655.

74. Pike GB, Meyer CH, Brosnan TJ, Pelc NJ. Magnetic resonance velocity imaging using a fast spiral phase contrast sequence. Magn Reson Med 1994;32(4):476-483.

75. Thompson RB, McVeigh ER. Flow-gated phase-contrast MRI using radial acquisitions. Magn Reson Med 2004;52(3):598-604.

76. Pruessmann KP, Weiger M, Scheidegger MB, Boesiger P. SENSE: sensitivity encoding for fast MRI. Magn Reson Med 1999;42(5):952-962.

77. Foo TK, Bernstein MA, Aisen AM, Hernandez RJ, Collick BD, Bernstein T. Improved ejection fraction and flow velocity estimates with use of view sharing and uniform repetition time excitation with fast cardiac techniques. Radiology 1995;195(2):471-478.

78. Markl M, Hennig J. Phase contrast MRI with improved temporal resolution by view sharing: k-space related velocity mapping properties. Magn Reson Imaging 2001;19(5):669-676.

79. McGibney G, Smith MR, Nichols ST, Crawley A. Quantitative evaluation of several partial Fourier reconstruction algorithms used in MRI. Magn Reson Med 1993;30(1):51-59.

80. Lustig M, Donoho D, Pauly JM. Sparse MRI: The application of compressed sensing for rapid MR imaging. Magn Reson Med 2007;58(6):1182-1195.

81. Baltes C, Kozerke S, Hansen MS, Pruessmann KP, Tsao J, Boesiger P. Accelerating cine phase-contrast flow measurements using k-t BLAST and k-t SENSE. Magn Reson Med 2005;54(6):1430-1438.

82. Bolster BD, Jr., Atalar E. Minimizing dead-periods in flow-encoded or -compensated pulse sequences while imaging in oblique planes. J Magn Reson Imaging 1999;10(2):183-192.

83. Atalar E, McVeigh ER. Minimization of Dead-Periods in MRI Pulse Sequences for Imaging Oblique Planes. Magn Reson Med 1994;32(6):773-777.

84. Derbyshire JA, Herzka DA, McVeigh ER, Lederman RJ. Efficient Implementation of Hardware-Optimized Gradient Sequences for Real-Time Imaging. Magn Reson Med 2010;64:1814-1820.

85. Hargreaves BA, Nishimura DG, Conolly SM. Time-optimal multidimensional gradient waveform design for rapid imaging. Magn Reson Med 2004;51(1):81-92.

86. Zou Y, Middione MJ, Srinivasan S, Ennis DB. Analysis of Gradient Spoiling in Phase Contrast. ISMRM Conf Proc Salt Lake City, Utah 2013.

87. Grant M, Boyd S. Graph implementations for nonsmooth convex programs, Recent Advances in Learning and Control (a tribute to M. Vidyasagar), V. Blondel, S. Boyd, and H. Kimura, editors, pages 95-110, Lecture Notes in Control and Information Sciences, Springer, 2008. http://stanford.edu/~boyd/graph_dcp.html.

88. Grant M, Boyd S. CVX: Matlab software for disciplined convex programming, version 2.0 beta. http://cvxr.com/cvx. 2012.

89. Boesch C, Gruetter R, Martin E. Temporal and spatial analysis of fields generated by eddy currents in superconducting magnets: optimization of corrections and quantitative characterization of magnet/gradient systems. Magn Reson Med 1991;20(2):268-284.

90. Gatehouse PD, Rolf MP, Bloch KM, Graves MJ, Kilner PJ, Firmin DN, Hofman MB. A multi-center inter-manufacturer study of the temporal stability of phase-contrast velocity mapping background offset errors. J Cardiovasc Magn Reson;14:72.

91. Parker DL, Gullberg GT. Signal-to-noise efficiency in magnetic resonance imaging. Med Phys 1990;17(2):250-257.

92. Reeder SB, McVeigh ER. The effect of high performance gradients on fast gradient echo imaging. Magn Reson Med 1994;32(5):612-621.